11-14-2018

Phonon Dispersion and Band Gap Engineering of Strained and Isotopically Enriched Atomically Thin Transition Metal Dichalcogenide Semiconductors

Wei Wu
University of Connecticut - Storrs, wei.2.wu@uconn.edu

Phonon Dispersion and Band Gap Engineering of Strained and Isotopically Enriched Atomically Thin Transition Metal Dichalcogenide Semiconductors

Wei Wu, PhD

University of Connecticut, 2018

Transition metal dichalcogenide (TMD) materials consist of strong intra-layer covalently bonded and weak inter-layer van der Waals bonded layers, which enable the preparation of atomically thin devices by either mechanical exfoliation or chemical vapor deposition (CVD). As a certain group of TMDs MX_2 (M=Mo, W; X=S, Se, Te) are scaled to the thickness of one three-atom-thick layer, the electronic dispersion undergoes a transition from an indirect to a direct band gap due to quantum confinement effects. The mechanical flexibility can be also enhanced by reducing layer number in TMDs. In view of these extraordinary properties, TMDs have been proposed as good candidate active materials for optoelectronic and photonic devices. However, the mechanisms of tuning electronic band gap energy and phonon dispersion are still unclear. In additional, the quantum emission behavior in atomically thin TMDs remains to be better understood.

This thesis examines the mechanisms of strain and isotope effect on optoelectronic and photonic transport in atomically thin WSe_2. A two-order of magnitude enhancement in the photoluminescence (PL) emission intensity in uniaxially strained single crystalline CVD grown WSe_2 bilayers is demonstrated using a new encapsulation four-point bending technique. A strain transfer model is developed considering 3-dimensional Poisson effect. Adding confidence to the high levels of elastic strain achieved, mode dependent Grüneisen parameters were obtained by

interpreting the Raman spectra. Additionally, a larger optical band gap in isotopically pure bilayer WSe_2 compared to the naturally abundant sample is reported in this thesis due to the isotope effect on the indirect excitons. The X-ray diffraction characterization reveals a slightly shorter interlayer van der Waals bond length in isotopic WSe_2 bilayer with heavier atomic mass.

Furthermore, a new route of creating locally defined single photon emitters on nominally bilayer WSe_2 is investigated. The bilayer WSe_2 is continuous over 1 cm^2 and transferred onto silicon oxide tip arrays to create engineered defects due to local strain. The seconder order photon correlation measurement confirms quantum emission arising from engineered defect sites. The results are promising for integration of quantum emission sites into scaled device architectures.

Phonon Dispersion and Band Gap Engineering of Strained and Isotopically Enriched Atomically Thin Transition Metal Dichalcogenide Semiconductors

Wei Wu

B.S., Tianjin University, 2008

M.S., Tianjin University, 2010

A Dissertation

Submitted in Partial Fulfillment of the

Requirements for the Degree of

Doctor of Philosophy

at the

University of Connecticut

2018

APPROVAL PAGE

Doctor of Philosophy Dissertation

Phonon Dispersion and Band Gap Engineering of Strained and Isotopically Enriched Atomically Thin Transition Metal Dichalcogenide Semiconductors

Presented by

Wei Wu, B.S., M.S.

Major Advisor

_____

Michael T. Pettes

Associate Advisor

_____

Ugur Pasaogullari

Associate Advisor

_____

Mark Aindow

Associate Advisor

_____

Avinash M. Dongare

Associate Advisor

_____

Karen C. Bustillo

University of Connecticut

2018

ACKNOWLEDGMENTS

First and foremost, I want to thank my advisor, Prof. Michael Thompson Pettes, who has led me into this exciting research field. It has been a great honor for being his first Ph.D. student to explore many interesting research fields. His talent for being a scientist and patience for being a mentor guide me to my achievements. I am also grateful to fellow lab members, particularly Jason Y. Wu, Nicomario C. Wright, Jeremy Brine and Danielle M. Leppert-Simenauer, who has been working with me on research.

I would like to thank two funding agencies, including National Science Foundation and FEI company for the support of finances to complete this thesis. In particular, FEI-UCONN Center of Excellence in Microscopy Fellowship afforded me the freedom to broaden my research projects.

I would also like to thank Dr. Karen C. Bustillo in the Nation Center for Electron Microscopy (NCEM) at Lawrence Berkeley Laboratory for being my project mentor and thesis committee. I am also thankful to other thesis committee members: Prof. Avinash M. Dongare, Prof. Mark Aindow, Prof. Ugur Pasaogullari for guiding me in research and preparing this thesis. In additionally, I would like to acknowledge Dr. Peter Ercius at NCEM for performing cross-sectional scanning transmission electron microscopy on WSe_2 bilayer in section 2.3.3, Dr. Robert A. Burke at U. S. Army Research Laboratory for providing graphene sample in section 3.3.3, Dr. Avinash M. Dongare for performing DFT calculation in section 3.5, Dr. Joan M. Redwing at The Pennsylvania State University for providing wafer-scale nominal bilayer WSe_2 sample in section 4.1, Dr. Joshua **R.** Hendrickson and Dr. C. Kavir Dass at the U. S. Air Force Research Laboratory for performing time resolved photoluminescence and the second order photon correlation

characterization in section 4.3.3. and polarized photoluminescence of section 4.3.4. Without their help, I would not have been able to complete this thesis.

Finally, I would like to thank my family for all their love and supports. For my parents who raised me up with love and unconditional supports. And for my wife, Wenqing Yu, who encourages me all of my days. I would not have been able to make such achievements without them.

Table of Contents

List of Tables ix

List of Figures x

Chapter 1: Introduction 1

1.1 Background on Atomically Thin van der Waals Materials 1

1.1.1 Strain Engineering in Atomically Thin Transition Metal Dichalcogenides .. 3

1.1.2 Quantum Emission in Atomically Thin Transition Metal Dichalcogenides 10

1.1.3 Isotopic Engineering in Atomically Thin Transition Metal Dichalcogenides 14

1.1.4 Raman Spectroscopy in Atomically Thin Transition Metal Dichalcogenides 17

1.2 Motivation and Scope of This Thesis 19

Chapter 2: Synthesis of Atomically Thin Transition Metal Dichalcogenides 23

2.1 Chemical Vapor Deposition System 23

2.2 Monolayer MoS_2 Single Crystals 24

2.2.1 Synthesis of Monolayer MoS_2 Single Crystals 24

2.2.2 Atomic Force Microscopy Analysis and Optoelectronic Characterization of Monolayer MoS_2 Single Crystals 25

2.3 Naturally Abundant Bilayer WSe_2 Single Crystals 29

2.3.1 Synthesis of Naturally Abundant Bilayer WSe_2 Single Crystals 29

2.3.2 Atomic Force Microscopy Analysis of Naturally Abundant Bilayer WSe_2 Single Crystals 30

2.3.3 Cross-sectional Scanning Transmission Electron Microscopy of Naturally Abundant Bilayer WSe_2 Single Crystals 31
2.3.4 Optoelectronic Characterization of As-grown Naturally Abundant Bilayer WSe_2 Single Crystals 35
2.4 Isotopically Pure Bilayer WSe_2 Single Crystals 36
2.4.1 Synthesis of Isotopically Pure Bilayer WSe_2 Single Crystals 36
2.4.2 X-ray Diffraction Characterization of Naturally Abundant and Isotopically Pure WSe_2 37
2.4.3 Atomic Force Microscopy and Optoelectronic Characterization of Isotopically Pure Bilayer WSe_2 Single Crystals 39
2.5 Conclusion 41
Chapter 3: Strain Dependent Optoelectronic Behavior in Atomically Thin Transition Metal Dichalcogenides 42
3.1 Sample Transfer and Encapsulation Method 42
3.2 Four-Point Bending Apparatus 45
3.3 Strain Analysis 46
3.3.1 Three-dimensional Poisson Effect Analysis 46
3.3.2 Strain Reversibility Study 51
3.3.3 Strain Transfer Verification 52
3.4 Strain Dependent Phonon Dispersion 57
3.5 Strain Dependent Photoluminescence and Optical Band Gap Evolution 59
3.6 Strain Transfer Analysis of Unencapsulated WSe_2 Bilayer Single Crystals 69
3.7 Conclusion 71

Chapter 4: Single Photon Source in Atomically Thin Transition Metal Dichalcogenides 72
4.1 Epitaxial Nominally Bilayer WSe_2 Growth and Characterization 72
4.2 Transfer Epitaxial Nominally Bilayer WSe_2 onto Sharp Tip Arrays 75
4.3 Single Photon Emission in Epitaxial Nominally Bilayer WSe_2 78
4.3.1 Continuous-wave Photoluminescence Spectroscopy of Epitaxial Nominally Bilayer WSe_2 on Sharp Tip 78
4.3.2 Power and Temperature Dependent Photoluminescence of Epitaxial Nominally Bilayer WSe_2 on Sharp Tip 80
4.3.3 Time Resolved Photoluminescence of Epitaxial Nominally Bilayer WSe_2 on Sharp Tip 83
4.3.4 Polarized Photoluminescence of Epitaxial Nominally Bilayer WSe_2 on Sharp Tip 87
4.4 Continuous-wave Photoluminescence from Intrinsic Defects 88
4.5 Conclusion 90
Chapter 5: Isotope Effect on the Indirect Excitonic Transition in an Atomically-thin Transition Metal Dichalcogenides 91
5.1 Phonon Dispersion of Naturally Abundant and Isotopically Pure WSe_2 Bilayers 91
5.2 Optical Band Gap of Naturally Abundant and Isotopically Pure WSe_2 Bilayers . 96
5.3 Conclusion 99
Chapter 6: Conclusion 100
References 102

List of Tables

Table 1. 1 Comparison of experimental and computational Grüneisen parameters of atomically thin van der Waals materials. (ε denotes the uniaxial strain; for black phosphorus, υ is the Poisson ratio of the SU-8 polymer substrate). 7

Table 1. 2 Comparison of single photon emission sources in vdW atomically thin materials. ("FSSE" denotes the fine structure splitting energy) 12

Table 1. 3 Character table for D_{3h} point group atomically thin TMDs. D_{3h} point group has 1 identity (E), 2 three-fold rotational axis (C_3), 3 axis (C_2) perpendicular to C_3, 1 horizontal plane of symmetry (σ_h), 2 center of symmetry (S_3), 3 vertical plane of symmetry (σ_v). "1" denotes the sign of vector is unchanged by symmetry operation, whereas "-1" represents a sign change due to asymmetry operation. 18

List of Figures

Figure 1. 1 Crystal structure of monolayer van der Waals materials. (a) graphene, (b) WSe_2. 2

Figure 1. 2 The layer number dependent thermal expansion coefficient amplification of transition metal dichalcogenides. Experimental data is from ref. 37. 4

Figure 1. 3 Comparison of the experimental E_{2g} mode Grüneisen parameters in TMD materials. The Grüneisen parameter of unencapsulated bilayer WSe_2 calculated based on the data from ref. 50 (red squares) is indicative of serious problems regarding the reported strain transferred to the 2D crystal. The Grüneisen parameters of monolayer MoS_2 and bilayer WSe_2 are adopted from refs. [47] and [39], respectively. 9

Figure 2. 1 Schematic of the CVD system with capability of both vacuum and atmospheric pressure. The carrier gas is selected by a 3-way valve. The system pressure can be switched between vacuum and atmospheric pressure by switching the downstream system from pump to bubbler. A dual-bubbler is used to prevent the sealant (silicone oil) from flowing back into the stainless steel gas line. 23

Figure 2. 2 Schematic illustration of the CVD growth of MoS_2. 25

Figure 2. 3 Optical characterization of MoS_2 monolayers on SiO_2 (258 nm)-on-Si substrate. (a) Optical microscopy image of MoS_2 monolayers. (b-c) Multi-energy Raman spectra of MoS_2 monolayer using the Si Raman peak for calibration. (d-e) Photoluminescence..... 26

Figure 2. 4 Characterization of diffusion limited growth of an MoS_2 monolayer. (a) Optical image of MoS_2 monolayer single crystal, (b) Atomic force microscopy analysis of MoS_2 monolayer with uniform thickness ~0.7 nm. Spatially resolved Raman intensity at (c) 384 cm^{-1} (E_{2g} mode), (d) 405 cm^{-1} (A_{1g} mode). (e) Spatially resolved photoluminescence shows uniform distributed optical band gap as 1.83 eV. The scale bar is 1 μm in all panels. 27

Figure 2. 5 Characterization of mass limited growth of an MoS_2 monolayer. (a) Optical image of MoS_2 monolayer and (b) atomic force microscopy analysis of MoS_2 monolayer with thickness ~0.7 nm at the flat region. Spatially resolved Raman intensity at (c) 384.5 cm^{-1} (E_{2g} mode), (d) 404.5 cm^{-1} (A_{1g} mode). (e) Spatially resolved photoluminescence mapping at 1.835 eV (blue color) and 1.875 eV (cyan color). (f) Point Raman spectra at 3 locations using 514 nm laser excitation. (g) Point photoluminescence spectra at 3 locations using 514 nm. The corner shows lower optical band gap of 1.875 eV, whereas the center region has higher optical band gap of 1.885 eV. The scale bar is 1 μm in all panels..... 28

Figure 2. 6 Schematic illustration of the CVD growth of WSe_2. 30

Figure 2. 7 Atomic force microscopy (AFM) analysis of naturally abundant WSe_2 bilayer single crystal. (A) AFM mapping of the entire domain demonstrates uniform thickness across the crystallite. (B) Cross-sectional height profiles demonstrate the thickness of WSe_2 bilayer single crystal is approximately 1.3 nm and is consistent with the *c*-axis unit cell parameter for AB-stacked WSe_2 (1.2983 nm, Powder Diffraction File #38-1388)[120]. 31

Figure 2. 8 Cross-sectional scanning transmission microscopy (STEM) sample prepared by Focused Ion Beam (FIB). Platinum protective layer coated by electron beam induced metal deposition after (a) 30 second, (b) 2 minutes, (c) 4 minutes, (d) 10 minutes deposition time.

(e) Platinum protective layer coated by Ga^+ ion beam induced metal deposition. (f) Ga^+ beam image after etching and polishing. (g) STEM bright field image of transferred laminate on copper grid. (h) STEM bright field image of the laminate showing Ga^+ Pt/e-beam Pt/WSe_2/SiO_2/Si. 33

Figure 2. 9 STEM of a WSe_2 bilayer single crystal. (a) Scanning electron micrograph showing a WSe_2 bilayer single crystal (bright triangle) and a thin electron-beam deposited platinum coating (bright square) used in the cross-sectioning process. (b) Cross-sectional high-angular annular dark-filed (HAADF) STEM analysis shows the bilayer structure of the CVD-grown WSe_2. (c) Line profile of the HAADF intensity along the length of the red line drawn in (b). The interlayer distance is measured as ~0.7 nm and is in agreement with the {0002} interplanar spacing of WSe_2 (d_{0002}=0.6493 nm, Powder Diffraction File #38-1388)[120]. The STEM image and profile shown in panels (b-c) were obtained by Dr. Peter Ercius at the Lawrence Berkeley National Laboratory Molecular Foundry's National Center for Electron Microscopy using the TEAM 0.5 instrument. 34

Figure 2. 10 Spatially dependent Raman intensity of WSe_2 bilayer single crystal. (a) Optical image of bilayer WSe_2 on SiO_2-on-Si substrate. Spatially resolved Raman intensity at (b) 250 cm^{-1} (E_{2g} mode), (c) 258.7 cm^{-1} (A_{1g} mode), and (d) 308.3 cm^{-1} (A^2_{1g} mode). Vibrational modes are depicted schematically in panels (b–d). 35

Figure 2. 11 (a) Linear- and (b) log-scale XRD spectra of naturally abundant $^{NA}W^{NA}Se_2$ (black line) and isotopically pure $^{186}W^{80}Se_2$ (red line). The diffractograms are aligned to the Si (004) peak to correct for specimen displacement. 38

Figure 2. 12 Spatially dependent characterization of an isotopically pure bilayer $^{186}W^{80}Se_2$ crystal. (a) Optical image and (b) atomic force microscopy (AFM) characterization of $^{186}W^{80}Se_2$ on a 285 nm SiO_2-on-Si substrate. (c) AFM height profile corresponding to line shown in (b). Spatially resolved Raman intensity at (d) 248.5 cm^{-1} (E_{2g} mode), (e) 256.7 cm^{-1} (A_{1g} mode), and (f) 305.9 cm^{-1} (A^2_{1g} mode), where the vibrational modes are depicted schematically. (g) Spatially resolved photoluminescence (PL) intensity at the peak emission wavelength of 1.58 eV..... 40

Figure 3. 1 Schematic illustration of WSe_2 encapsulation process. The thickness of each PMMA encapsulation layer is ~500 nm, and the thickness of flexible PET substrate is 1 mm..... 43

Figure 3. 2 Photoluminescence-based layer number determination of encapsulated WSe_2. (a) AFM analysis of WSe_2 crystal with bilayer, trilayer, and bulk features. (b) Cross-sectional height profiles demonstrate the thickness of bilayer (~1.3 nm) and trilayer (~1.8 nm) WSe_2. (c) Optical image of the PMMA/WSe_2/PMMA/PET composite. (d) Photoluminescence spectra of bilayer WSe_2 (red curve) and trilayer WSe_2 (black curve) taken from the corresponding regions depicted in (c). 44

Figure 3. 3 Custom four-point bending apparatus. (a) Photograph of the four-point bending apparatus assembled onto Horiba Multiline Raman Spectrometer-LabRAM HR Evolution. (b) Photograph of the experimental apparatus applying uniaxial strain to a poly(methyl methacrylate) (PMMA)-encapsulated bilayer WSe_2 sample affixed to a flexible poly(ethylene terephthalate) (PET) substrate. Tick marks machined into the right of the device (below scale bar) indicate mm. (c) Optical microscope image of a bilayer WSe_2

crystallite encapsulated by two thin PMMA layers on a flexible PET substrate. The crystal is outlined in red as a guide to the eye. 45

Figure 3. 4 Schematic of the Poisson effect on a uniaxially strained WSe_2 bilayer encapsulated in PMMA on top of a PET substrate: $\varepsilon_{//}$ is the uniaxial strain applied through the four-point bending apparatus, $\varepsilon_{\perp\perp,\text{in-plane}}$ is the in-plane compressive strain caused by the Poisson effect of the PMMA/PET composite, and $\varepsilon_{\perp\perp,\text{out-of-plane}}$ is the out-of-plane compressive strain from the Poisson effect on the PMMA encapsulation layer..... 48

Figure 3. 5 Reproducibility of strain-controlled photoluminescence (PL) emission spectra. (a) Cyclic stability of the maximum PL intensities of bilayer WSe_2 at uniaxial strain, $\varepsilon_{//}$, demonstrating elastic and reversible strain up to 1.56%. (b) Corresponding PL spectra of cyclically strained bilayer WSe_2..... 51

Figure 3. 6 Patterned graphene used in strain verification experiment. (a) Scanning electron microscopy image of a continuous monolayer graphene film patterned into triangular domains with edge lengths of ~12 μm. (b) Raman spectra of graphene before and after patterning. Although the defect-enabled D peak appears for graphene patterned by Ga^+ focused ion beam milling, the 2D-to-G peak intensity ratio remains ~2 as expected for monolayer graphene. 53

Figure 3. 7 Measured Raman spectra and Grüneisen parameter of the 2D mode of CVD-grown encapsulated graphene patterned into triangles. (a) Raman spectra as a function of applied uniaxial strain. (b) Strain dependence of the 2D peak Raman shift, obtained by deconvolution of the experimental spectra using Lorentzian distributions. Also shown is the

strain dependence of the 2D mode of unencapsulated graphene reproduced from ref. 46. Uncertainties in $\partial\omega/\partial\varepsilon_{//}$ are given as the upper and lower 95% confidence bounds of a linear regression model for both data sets. The linear train dependence of the Raman shift indicates no observable strain relaxation. (c) The Grüneisen parameter for the 2D mode is obtained from the strain-dependent Raman spectra as 3.66 with a standard deviation of 0.23. This is in agreement with the 2D mode value of 3.583±0.267 calculated from ref. 46, where uncertainty is defined using the upper and lower 95% confidence bounds. 55

Figure 3. 8 Measured Raman spectra and Grüneisen parameter of the 2D mode of CVD-grown encapsulated unpatterned graphene. (a) Raman spectra as a function of applied uniaxial strain. (b) Strain dependence of the 2D peak Raman shift, obtained by deconvolution of the experimental spectra using Lorentzian distributions. Also shown is the strain dependence of the 2D mode of unencapsulated graphene reproduced from ref. 46. Uncertainties in $\partial\omega/\partial\varepsilon_{//}$ are given as the upper and lower 95% confidence bounds of a linear regression model for both data sets. The linear train dependence of the Raman shift indicates no observable strain relaxation. (c) The Grüneisen parameter for the 2D mode is obtained from the strain-dependent Raman spectra as 3.894 with a standard deviation of 0.214. This is in agreement with the 2D mode value of 3.583±0.267 calculated from ref. 46, where uncertainty is defined using the upper and lower 95% confidence bounds. 56

Figure 3. 9 Raman spectra of bilayer WSe_2 as it is strained up to 3.59%. (a) Raman spectra as a function of uniaxial strain ($\varepsilon_{//}$). As strain increases, the in-plane E_{2g} optical phonon mode evolves into separate E^{+}_{2g} and E^{-}_{2g} modes. (b) Strain dependence of the peak Raman shifts for the E^{+}_{2g}, E^{-}_{2g}, A_{1g}, and A^{2}_{1g} modes, obtained by deconvolution of the experimental Raman

spectra using Lorentzian distributions. The linear strain dependence of the Raman shift indicates strain relaxation by slippage or plastic deformation is not observed. (c) Mode-specific Grüneisen parameters of bilayer WSe_2 are constant over the range of $0.01 \leq \varepsilon_{//} \leq 0.036$. 59

Figure 3. 10 Photoluminescence spectra of bilayer WSe_2 with increasing uniaxial strain. PL intensity versus emission energy is shown for $\varepsilon_{//}$ = (a) 0, (b) 0.54, (c) 1.03, (d) 1.56, (e) 1.93, (f) 2.47, (g) 3.18, and (h) 3.59% under continuous wave excitation at an energy of 2.33 eV (λ = 532 nm). The indirect (dash-dotted lines) and direct (solid lines) optical transition peaks were deconvolved using Gaussian distributions, and the background is shown as a gray dashed line. 60

Figure 3. 11 Amplification of the photoluminescence (PL) emission intensity of WSe_2 bilayer when strained up to 3.59%. (a) PL emission spectra resulting from excitation at 2.33 eV as a function of applied uniaxial strain. Inset shows the PL spectra of the unstrained material, $\varepsilon_{//}$=0, where the indirect (dash-dotted line) and direct (solid line) electronic transitions have been deconvolved using Gaussian distributions. (b) Experimental PL amplification versus strain, defined as $I(\varepsilon_{//}) / I(\varepsilon_{//}=0)$. Subscripts max, direct, and indirect denote amplification obtained using the max intensity of the experimental PL, the max intensity of the deconvolved direct sub-peak, and the max intensity of the deconvolved indirect sub-peak, respectively. All computational results were conducted by Dr. Jin Wang and Prof. Avinash Dongare, University of Connecticut Materials Science and Engineering, and obtained by density functional theory (DFT) including the effect of spin orbit coupling, van der Waals

interactions, and Poisson effect from PMMA/PET are shown for the direct (solid light blue line) and indirect (dashed light blue line) electronic transitions. 62

Figure 3. 12 Indirect-to-direct electronic band transition conversion through strain. (a) Evolution of the electronic band structure in response to uniaxial strain calculated using density functional theory including both spin orbit coupling, interlayer van der Waals interactions, and the Poisson effect (DFT-vdW-Poisson) for $\varepsilon_{//}$ = 0% (red) to 4% (purple) in increments of 0.5%. Direct and indirect electronic transitions are depicted. (b) Strain-dependence of the interband transition energies normalized to that of the unstrained indirect PL transition. Experimental values have been obtained by deconvolution of the PL emission spectra using Gaussian distributions and are shown in comparison with a DFT-vdW-Poisson model (blue lines, DFT calculations by Dr. Jin Wang and Prof. Avinash Dongare, University of Connecticut Materials Science and Engineering) and a calculation neglecting van der Waals interactions (DFT-HSE, obtained from ref. 50). The indirect-to-direct conversion occurs at $\varepsilon_{//} > 3.5\%$ in both the experiment and DFT-vdW-Poisson calculation and at ~0.5% when vdW interactions are neglected (DFT-HSE[50]), indicating that increased interlayer coupling strength may lead to weaker strain-coupled effects in layered materials. 68

Figure 3. 13 Comparison of experimentally observed optical direct and indirect band gap energy in this thesis (red circles, orange squares) and in a report by Desai *et al.*[50] (blue and green triangles). The direct and indirect band gap energies for the previous work[50] are obtained by deconvolution of the photoluminescence spectra reported in that publication. 70

Figure 4. 1 Wafer-scale, nominally bilayer epitaxial WSe_2 synthesized on *c*-plane sapphire. (a) Scanning electron micrographs showing large-area coalesced and uniform coverage of small-grain size WSe_2 synthesized by gas source chemical vapor deposition. (b) Atomic force microscopy analysis showing textured growth of predominantly bilayer to trilayer WSe_2. (c) X-ray photoelectron spectroscopy analysis demonstrates a 1:2 atomic ratio tungsten:selenium, and no detectable coordination with oxygen. (d) Raman spectroscopy exhibits no carbonaceous peaks and indicates 2–3 layer WSe_2 (inset). 73

Figure 4. 2 The photoluminescence mapping at 4K of as-grown WSe_2 on sapphire *c*-plane (0001) substrate. (a) Photoluminescence mapping of emission peak center at 758 nm at 4K temperature. (b) All PL spectra of mapping shows no defect emission from WSe_2 at each pixel. (c) The point-PL emission spectra show two high intensity PL peak originating from sapphire. (d) Point-PL spectra shows the emission of nominally bilayer WSe_2 on sapphire.74

Figure 4. 3 Demonstration of ability to transfer of large-area WSe_2 onto ultra-sharp tip arrays. (a) Optical microscopy and (b) scanning electron microscopy images of MOCVD-grown nominally bilayer WSe_2 coated with ~500 nm of poly(methyl methacrylate) (PMMA) transferred onto a tip array. (c) Scanning electron microscopy image of the WSe_2 on the tip array after removal of PMMA with acetone and hydrogen annealing. 76

Figure 4. 4 Ultra-large strain and strain gradients are possible for atomically thin crystals transferred onto ultra-sharp tips. (a) Calculated maximum strain that will arise on the top (tensile) and bottom (compressive) surfaces of an *n*-layer WSe_2 film as a function of tip radius according to equation 6.1. (b) Calculated strain gradient occurring across the sample. (c-d) Scanning electron micrographs of a representative sharp tip. 77

Figure 4. 5 Continuous-wave photoluminescence spectra shows the engineered emission sites. (a) Optical micrograph and (b) spatial continuous-wave excitation PL of nominally bilayer epitaxial WSe_2 transferred onto an ultra-sharp SiO_2 tip on a SiN_x-on-Si substrate, where the integrated area of the localized exciton peak over the free exciton is shown versus x-y coordinate. 79

Figure 4. 6 Temperature dependence of localized emission. Photoluminescence spectra of localized emission from WSe_2 on an ultra-sharp SiO_2 tip as a function of temperature obtained using femtosecond excitation at 540 nm. Inset shows that the peak emission wavelength is relatively constant over the measured temperature range with a mean of 772.95 nm and a standard deviation of 0.83 nm. This experiment was conducted by Dr. C. Kavir Dass and Dr. Joshua R. Hendrickson at the U. S. Air Force Research Laboratory in Dayton, Ohio. 81

Figure 4. 7 Power dependent PL spectra of localized emission. (inset) Peak emission wavelength is relatively constant over the measured excitation power range with a mean of 772.88 nm and a standard deviation of 0.27 nm. This experiment was conducted by Dr. C. Kavir Dass and Dr. Joshua R. Hendrickson at the U. S. Air Force Research Laboratory in Dayton, Ohio. 82

Figure 4. 8 Time resolved photoluminescence (TRPL) spectra of localized emission from WSe_2 on an ultra-sharp SiO_2 tip as a function of average excitation power obtained using femtosecond excitation at 540 nm. Equation 6.2 is used to deconvolve free (fast decay, dotted line) and bound (slow decay, dashed line) exciton contributions to the measured event count. The bottom graph shows the fitting residue at each laser power. This

experiment was conducted by Dr. C. Kavir Dass and Dr. Joshua Hendrickson at the U. S. Air Force Research Laboratory in Dayton, Ohio. 84

Figure 4. 9 Second order photon correlation of nominally bilayer WSe_2 on the apex of sharp tip. Measured second order photon correlation $g^{(2)}(\Delta t)$ obtained using continuous wave excitation at 532 nm and collected at $\lambda_{emission}$ = 772.9 nm using short- and long-pass tunable filters for a collection period of 45 minutes as a function of time delay Δt. This experiment was conducted by Dr. C. Kavir Dass and Dr. Joshua Hendrickson at the U. S. Air Force Research Laboratory in Dayton, Ohio. 86

Figure 4. 10 Polarization dependence of the localized peak emission intensity (squares) demonstrates no preferential orientation of the emitted photons, which can be fit as 8.68±0.18 counts$\cdot s^{-1}\cdot \mu W^{-1}$ (line). 87

Figure 4. 11 Continuous-wave spatial photoluminescence of WSe_2. (a) PL intensity of three intrinsic defect emission peaks. Spatial PL mapping of emission peaks at (b) 740 nm, (c) 750 nm, and (d) 765 nm. The peaks shown in (a) are obtained from the brightest pixel in corresponding panels (b-d) and are weaker than the quantum emitter detected on the sharp tip apex (see Figure 4.5b). 89

Figure 5. 1 Isotopic mass dependent Raman spectra of bilayer WSe_2. Normalized Raman spectra of (a) naturally abundant $^{NA}W^{NA}Se_2$, and (b) isotopically pure $^{186}W^{80}Se_2$ over the temperature range from 4.41 to 300 K. (c) The phonon frequency difference ($\Delta\omega$) of E_{2g} (red), A_{1g} (blue) and A^2_{1g} (green) modes between $^{NA}W^{NA}Se_2$ and $^{186}W^{80}Se_2$, where error is

defined by the standard deviation of 6 measurements each with a different spectral window initial point in order to minimize the instrumental uncertainty. Temperature-dependent phonon lifetime and full width at half maximum of the (d) E_{2g} mode and (e) A^2_{1g} mode from 4.41 to 300 K. 94

Figure 5. 2 Temperature dependence of Raman active mode peak positions isotopically engineered bilayer WSe_2. Raman shift for the (a) E_{2g}, (b) A_{1g}, and (c) A^2_{1g} modes of naturally abundant $^{NA}W^{NA}Se_2$ (solid symbols) and isotopically pure $^{186}W^{80}Se_2$ (open symbols). 95

Figure 5. 3 Isotopic mass dependent photoluminescence and optical band gap. Normalized photoluminescence spectra over a temperature range from 4.41 to 300 K for (a) naturally abundant bilayer $^{NA}W^{NA}Se_2$, and (b) isotopically pure bilayer $^{186}W^{80}Se_2$. (c) Difference in optical band gap between $^{NA}W^{NA}Se_2$ and $^{186}W^{80}Se_2$. (d) Temperature dependence of the band gap of $^{NA}W^{NA}Se_2$ and $^{186}W^{80}Se_2$, where modeling results using the empirical Varshni relation are given by solid and dashed lines, respectively..... 98

Chapter 1: Introduction

1.1 Background on Atomically Thin van der Waals Materials

The van der Waals (vdW) crystals are the materials consisting of strong intra-layer covalently bonded and weak inter-layer van der Waals bonded atoms. Due to their layered structure and relatively weak inter-layer van der Waals bonds compared to intra-layer covalent bonds, the bulk graphite and bulk molybdenum disulfide (MoS_2) are commonly used as dry lubricants. Despite their lubricant applications, the weak van der Waals bonds also enable people to prepare atomically thin materials with one or few atom thickness by either mechanical exfoliation[1], chemical vapor depositon (CVD)[2,3], or other techniques[4]. Compared to bulk vdW materials, recently proposed technologies based on these materials offer size, weight, and power advantages not currently achievable using traditional materials, and are especially promising for nanophotonic applications[5,6] including quantum emission sources[7-16].

Graphene was the first obtained free-standing two-dimensional (2D) material consisting of one atomic carbon layer by mechanical exfoliation[1,17]. The isolated 2D graphene is stable at room temperature in air and remains macroscopically continuous with high carrier mobility[1,18]. Graphene also shows high thermal conductivity for both suspended[19,20] and supported cases[21] and exhibits two-dimensional phonon transportation[21] which has drawn numerous attention in electronic and thermal physics research fields. Owning these extraordinary properties, the applications of graphene have broadened to atomically thin flexible electronics[22], visible light sources[23], optical modulators[24], and high performance batteries[25].

However, due to lack of an electronic band gap in graphene and ultra-thin graphite, certain applications are greatly limited where semiconductors with non-trivial electronic band gap are required. Transition metal dichalcogenides (TMDs) are a relatively new class of atomically thin materials receiving interest for overcoming limitations inherent to graphene-based electronics, of which there are more than 40 unique TMDs encompassing a diverse range of unique properties[26-29]. Instead of having one only carbon atom in each vdW layer, the TMDs MX_2 (M=Mo, W; X=S, Se, Te) composes three atoms in each layer: chalcogen atoms in the top and bottom, metal atoms in the middle, as Figure 1.1 shows.

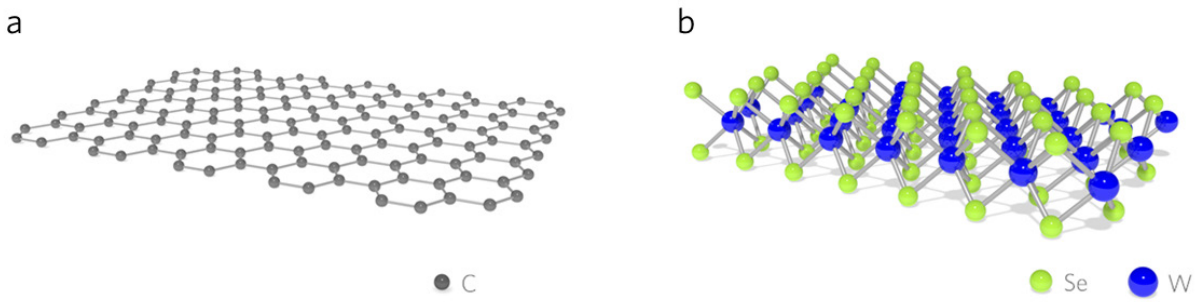

Figure 1. 1 Crystal structure of monolayer van der Waals materials. (a) graphene, (b) WSe_2.

Electronic band gap engineering in atomically thin TMDs is a new route to achieve tunable and flexible electronic and optoelectronic applications. As certain MX_2 TMDs are scaled to the thickness of one three-atom-thick layer, the electronic dispersion undergoes a transition from an indirect to a direct band gap due to quantum confinement effects[30-33]. In addition, certain phases also exhibit electronic band gap tunability via changing layer number[30], electrical gating[34], and heterostructure[35,36]. Therefore, the precise manipulation of electron and phonon band structure in atomically-thin TMDs materials becomes the key to widespread adoption in applications. Since

the difficulty of dynamically changing layer numbers without breaking the materials, other approaches (strain, isotopes, *etc.*) become on-demand and more applicable for manipulating phonons and the optical band gap. In additional to the unique phonon and optoelectronic properties, atomically thin TMDs have larger flexibility than their bulk phases[37] which further broaden their application in strain or flexible device related fields.

In the following sections of this chapter, first the current status of manipulating electron and phonon band structures through strain engineering will be discussed. Secondly, single photon quantum emission arising from these materials will be introduced as a future application of strained atomically thin TMDs. Thirdly, the idea of manipulating phonon and optical band gap through isotopic engineering will be raised and discussed. In addition, the fundamental principles of Raman spectroscopy will be illustrated in order to better understand later chapters. Last, the scope of present work will be briefly described.

1.1.1 Strain Engineering in Atomically Thin Transition Metal Dichalcogenides

Apart from the unique electrical and optoelectrical properties, atomically thin TMDs also show outstanding mechanical properties. In contrast to Si which usually breaks at ~1.5% strain, monolayer MoS_2 exhibits breaking at ~11% strain which is similar as graphene with breaking strain at 13%[38]. In addition, Figure 1.2 shows that higher thermal expansion coefficient (TEC) was observed in atomically thin TMDs than their bulk counterparts. The maximum TEC was measured as 47 times higher in monolayer MoS_2 than that of bulk MoS_2[37]. Since the bulk modulus is inversely proportional to the TEC, this results in atomically thin TMDs exhibiting the same order of magnitude of TEC as that of some polymers[39]. This significant stretchability in atomically thin materials not only shows the promising application in bendable and wearable technologies, but

also open the possibility of tuning the electrical and optoelectrical properties by strain engineering. Theoretically, it has been predicted that elastic strain[40,41] can be used as an extrinsic method to reversibly engineer a direct band gap in multilayer crystals with indirect band gaps.

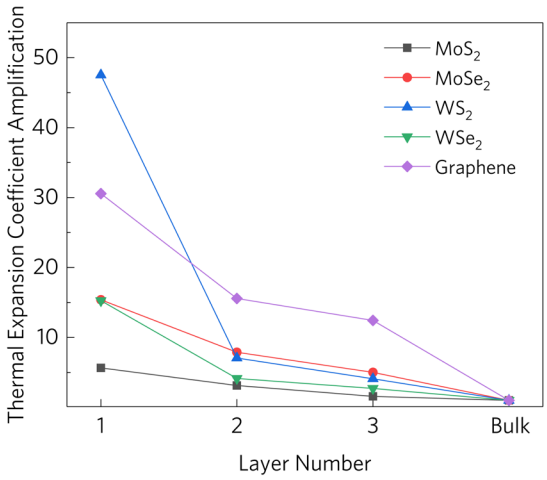

Figure 1. 2 The layer number dependent thermal expansion coefficient amplification of transition metal dichalcogenides. Experimental data is from ref. 37.

One method to strain atomically-thin TMDs is to place them on a piezoelectric substrate, in which the optical band gap energy increases ~60 meV with 0.2% compressive biaxial strain in trilayer MoS_2[42]. Another approach is to strain suspended atomically thin TMDs placed over a cavity by creating a pressure difference between the inside and outside of the cavity[43]. With this method[43], monolayer MoS_2 showed an optical band gap change of 99 meV/% biaxial strain and Grüneisen parameters (γ) were measured to be 0.68 for the E_{2g} mode and 0.21 for the A_{1g} mode with up to ~2% strain. Besides above two methods, use of an AFM probe[44] and a wrinkled substrate[45] were also used to apply tensile strain[44]. However, it is difficult to accurately evaluate the strain dependent optoelectrical properties in these methods due to the large strain gradient

created in regions of only a few hundred nm which is comparable to the beam spot size of commonly used laser probes such as 514 nm, 532 nm and 633 nm.

A higher throughput method to strain atomically thin materials is four-point bending which was first introduced for straining graphene[46]. Exfoliated graphene was placed onto an SU-8 coated PET substrate, where the SU-8 was used as adhesion layer and the PET was used as a flexible substrate[46]. The Grüneisen parameter was experimentally measured as $\gamma_{E_{2g}}$=1.99[46] with strain up to ~1.3%. By a similar method, monolayer MoS_2 shows ~45 meV/% strain changes in the optical band gap, and bilayer MoS_2 shows ~120 meV/% strain change with up to 2.2% tensile strain[47]. The Grüneisen parameter of the E_{2g} mode was also measured as ~1.06 in the same study[47] which is half that of the graphene's Grüneisen parameter of E_{2g} mode[46] and comparable to that of hexagonal boron nitride[48,49]. Moreover, bilayer WSe_2 strained by the four-point bending method exhibits ~35 times higher photoluminescence enhancement at 2% tensile strain due to the electronic band structure evolution with strain[50]. The above experiments were all done by directly placing atomically thin TMDs onto a flexible substrate with either sputtered titanium clamps[47] or without clamps[46,50].

Another important topic that needs to be addressed is the efficiency of strain transferred from the substrate to the atomically thin materials in four-point bending method, as all studies assumed 100% of the substrate strain was transferred to the material. In order to evaluate the strain transfer efficiency, the Grüneisen parameter can be measured by Raman spectroscopy and used as an indicator in comparison with known values or those calculated theoretically. In contrast with hard substrates such as Si wafers with a Poisson ratio ~0.22[51], the flexible polymer substrates have higher Poisson ratios, such as PET (0.37-0.44)[39], PMMA (0.35-0.4)[39], PC (0.33)[47] and SU-8

(0.33)[46]. Thus, when uniaxial tensile strain is applied to a flexible polymer substrate, non-negligible compressive strain also occurs in the direction perpendicular to the tensile strain due to the Poisson effect. If the atomically thin sample is unencapsulated, only the in-plane compressive strain is considered in the analysis[46,47]. Moreover, the sample can be also encapsulated between polymer layers to avoid exposure to air[52] or to more efficiently transfer strain from substrate to sample[39,52]. For the encapsulated sample, the compressive strain is both in-plane and out-of-plane. So, it is necessary to know the Poisson ratio of the substrate in both directions if the top and bottom encapsulation layers are different materials or if the Poisson ratio is anisotropic. The experimental Grüneisen parameters of some atomically thin van der Waals materials is showing in Table 1.1.

Table 1. 1 Comparison of experimental and computational Grüneisen parameters of atomically thin van der Waals materials. (ε denotes the uniaxial strain; for black phosphorus, υ is the Poisson ratio of the SU-8 polymer substrate).

Materials	Grüneisen parameter (γ)				
	$\gamma_{E_{2\gamma}}$ (γ_G)	γ_{2D}	$\gamma_{A_{1g}}$	$\gamma_{A_{1g}^2}$	$\gamma_{B_{2g}}$
Graphene	1.99[46] 1.97±0.15[53] 1.8±0.18[54] 2.4±0.2[55] 1.8±0.2[56] 1.8 (DFT)[46]	3.58[46] 2.83±0.12[53] 2.6±0.13[54] 3.8±0.3[55] 2.4±0.2[56] 2.98[57] 3.66[39]	-	-	-
MoS_2 (monolayer)	1.1±0.2[47] 0.6[58] 0.65[59]	-	0.21[59]	-	-
MoS_2 (bilayer)	1.0±0.2[60]	-	-	-	-
WS_2 (monolayer)	0.5[61] 0.54[62]	-	0.18[61]	-	-
WSe_2 (bilayer)	1.149±0.027[39] 0.38[62]	-	0.307±0.061[39]	0.357±0.103[39]	-
Black phosphorus ~15 layers (ε // to zigzag)	-	-	*0.14 (υ=0)[52] *0.22 (υ=0.33)[52] *-0.05 (υ=0, DFT)[52] *-0.46 (υ=0.33, DFT)[52]	*0.92 (υ=0)[52] *1.38 (υ=0.33)[52] *0.87 (υ=0, DFT)[52] *1.31 (υ=0.33, DFT)[52]	*2.47 (υ=0)[52] *3.69 (υ=0.33)[52] *2.10 (υ=0, DFT)[52] *3.09 (υ=0.33, DFT)[52]
Black phosphorus ~15 layers (ε // to armchair)	-	-	*1.05 (υ=0)[52] *1.57 (υ=0.33)[52] *0.63 (υ=0, DFT)[52] *0.89 (υ=0.33, DFT)[52]	*0.01 (υ=0)[52] *0.01 (υ=0.33)[52] *-0.11 (υ=0, DFT)[52] *-0.64 (υ=0.33, DFT)[52]	*0.42 (υ=0)[52] *0.63 (υ=0.33)[52] *0.16 (υ=0, DFT)[52] *-0.73 (υ=0.33, DFT)[52]

*Note: ref. 52 stated that the theoretical simulation results match the experimental results without considering the Poisson effect from the substrate (υ=0). Whereas, the experimental result considering the Poisson effect (υ=0.33) leads to larger γ. However, ref. 46 showed the necessity of considering the substrate Poisson effect. Thus, both results are listed here.

The importance of evaluating strain transfer efficiency can be shown by comparing the Grüneisen parameter of atomically thin vdW materials from different studies. By extrapolating the strain dependent E_{2g} mode, the Grüneisen parameter can be calculated as Figure 1.3 shows. In one previous study[50], $\gamma_{E_{2g}}$ decreases from 1.58 to 1.32 instead of maintaining a constant value. This indicates slippage or other problems with the study as γ is not strain dependent[63]. Comparing with a previous study on monolayer MoS_2[47] and bilayer WSe_2[39], the large and decreasing Grüneisen parameter in ref. 50 may indicate an overestimated strain value and also slippage between sample/substrate or between WSe_2 layers. Thus, it is necessary to evaluate the strain transfer efficiency in order to accurately study strain dependent properties when using four-point bending method.

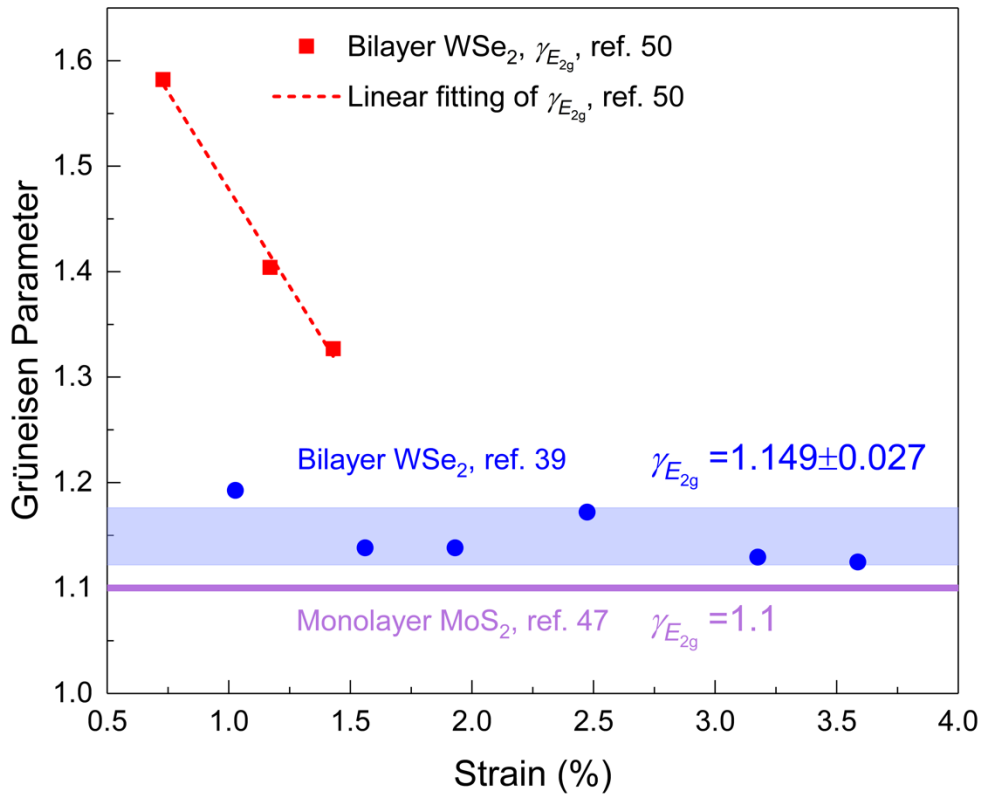

Figure 1. 3 Comparison of the experimental E_{2g} mode Grüneisen parameters in TMD materials. The Grüneisen parameter of unencapsulated bilayer WSe_2 calculated based on the data from ref. 50 (red squares) is indicative of serious problems regarding the reported strain transferred to the 2D crystal. The Grüneisen parameters of monolayer MoS_2 and bilayer WSe_2 are adopted from refs. [47] and [39], respectively.

1.1.2 Quantum Emission in Atomically Thin Transition Metal Dichalcogenides

Quantum single photon emission is another very recently found phenomenon of atomically thin TMDs. The single photon state is an excitation of the electromagnetic field, in which detectors measure exactly one phone for each incident state. So the photon number statistic has a mean value of one photon with variance of zero[64]. Single photon generation is a requirement for quantum key distribution and all-optical quantum computing, crucial for the advancement of quantum information technologies[65-70]. The information is encoded in the quantum state of each photon which travels at the speed of light and weakly interacts with the environment over long distances[64]. Using this phenomenon, researchers have recently demonstrated an 'un-hackable' transmission of data over a satellite-based network[71].

The single photon purity is one important property for the ideal single photon source which can be measured by Hanbury Brown and Twiss experiment[72]. The incident light passes a beam splitter and two single-photon detectors measuring output, where the correlation of time delay is measured between these detectors[72,73]. This correlation can be evaluated by the second order correlation function as[73]:

$$g^{(2)}(0)=\frac{\langle n_1(t)n_2(t)\rangle}{\langle n_1(t)\rangle\langle n_2(t)\rangle} \tag{1.1}$$

where $n_i(t)$ is the number of counts detected on detector i at the time t. For an ideal single photon source, the probability of multiple photon number is zero and $g^{(2)}(0)=0$.

Solid-state single photon sources have been commonly found to arise from defects in 1-dimensional[15,74] (carbon nanotube) or 3-dimensional[75-79] (quantum dots, diamond and cubic silicon carbide) materials. Several recent studies have observed single photons originating from defect

structures in mechanically exfoliated WSe_2[6-12,14,80], WS_2[6,8], hexagonal-BN (*h*-BN)[81], and GaSe[16,82], and in chemical vapor deposition synthesized WSe_2[83] and *h*-BN[13]. Optical emission energy in these systems resides within the electronic band gap and excitation had been provided by both direct[6-13,16] and remote optical pumping[82], and electrical charge injection[6]. Previous studies have postulated that non-uniform strain fields govern quantum emission in these materials[7,8,84] which may benefit secure communication technologies as the use of single photon sources requires both spatial control of the emission site and no more than one emitter per site[85-87]. For secure military communications, the use of single photon sources requires both spatial control of the emission site and no more than one emitter per site. However, the mechanism responsible for recent demonstration of strain-engineered single photon sources in TMDs using tent-pole style pillars[7,8] remains unclear, as does the generality of conclusions based on these studies. Additionally, scalability also currently limits progress: lab-scale mechanical exfoliation and powder vapor transport growth of small crystallites constitute the only cases where this effect has been observed in semiconducting atomically thin materials[6-12,14,16,80,82,83] . Thus, an approach for creating highly spatially localized and well-separated emission sites in a continuous film TMDs is needed.

Table 1. 2 Comparison of single photon emission sources in vdW atomically thin materials. ("FSSE" denotes the fine structure splitting energy)

Materials	Defect emission energy (eV)	Emission wavelength (nm)	Lifetime (ns)	$g^{(2)}(0)$	FSSE (μeV)	Temperature (K)
WSe_2	~1.63[6]	~760[6]	9.4±2.8[6]	0.29±0.08[6]	-	10[6]
(monolayer)	1.55[7]	800[7]	2.8±0.02[7]	0.07±0.04[7]	700-900[7]	3.5[7]
	1.59-1.66[8]	748-780[8]	3.08-8.81[8]	0.087-0.18[8]	200–730[8]	10[8]
	1.707±0.001[9]	726[9]	1.8-6.5[9]	0.32[9]	-	10[9]
	1.681[9]	738[9]	7-9.6[9]	0.28[9]	-	10[9]
	~1.69[10]	735.8[10]	1.51[10]	0.20±0.02[10]	-	4.2[10]
	~1.71[10]	723.5[10]	2.5[10]	0.18±0.02[10]	-	4.2[10]
	1.636[11]	758[11]	0.6[11]	0.3[11]	-	4.2[11]
	1.65-1.7[12]	729-751[12]	0.5-1.8[12]	0.36[12]	730±29[12]	4.2[12]
	1.58[14]	782.7[14]	4.14[14]	0.17[14]	726[14]	4[14]
	1.60-1.725[80]	719-775[80]	1.9-2.8[80]	0.19-0.23[80]	-	10[80]
	1.719[83]	721[83]	1.79±0.002[83]	0.21±0.06[83]	590-750[83]	4[83]
WSe_2 (bilayer)	~1.48-1.60[7]	775-835	4.8±0.1[7]	0.03±0.02[7]	-	3.5[7]
WS_2	~1.93[6]	642[6]	1.4±0.15[6]	0.31±0.05[6]	-	10[6]
(monolayer)	~1.97-2.00[8]	618-630[8]	-	-	300-810[8]	10[8]

Materials	Defect emission energy (eV)	Emission wavelength (nm)	Lifetime (ns)	$g^{(2)}(0)$	FSSE (μeV)	Temperature (K)
h-BN (monolayer)	1.99[13]	623[13]	-	~0.3[13]	-	77-300[13]
h-BN (multilayer)	1.99[13] 1.88[81]	623[13] 658.6[81]	3.09[13] -	0.33±0.12[13] 0.3-0.39[81]	- -	77-300[13] 10-300[81]
GaSe (multilayer)	1.881±0.002[16] 1.98-1.99[82]	659[16] 623-626[82]	- 1[82]	0.33[16] 0.13-0.37[82]	- -	10[16] 10[82]
Solitary doped SWCNT	95% < 1.186[85] E_{11}*: ~1.107[85] E_{11}*$^{-}$: ~0.992[85]	95%>1045[85] E_{11}*: ~1120[85] E_{11}*$^{-}$: ~1250[85]	0.431 (4 K)[85] 0.457 (50 K)[85] 0.475 (100 K)[85] 0.420 (150 K)[85] 0.251 (200 K)[85] 0.215 (230 K)[85] 0.194 (260 K)[85] 0.108 (270 K)[85] 0.120 (298 K)[85]	0.04-0.39 (4 K)[85] 0.25 (50 K)[85] 0.07 (100 K)[85] - 0.47 (200 K)[85] 0.09 (230 K)[85] 0.17 (260 K)[85] - -	-	4-298[85]
sp^3 defect in SWCNT	0.775-1.127[15]	1100-1600[15]	~0.07-0.62[15]	85% < 0.1[15]	-	300[15]

1.1.3 Isotopic Engineering in Atomically Thin Transition Metal Dichalcogenides

In additional to the strain effect, the isotopic effect is a static state knob to tune phonon and electron transport of van der Waals materials[88] without mechanically changing lattice structure. Isotopes are the element with same proton and electron numbers but having a different number of neutrons, resulting lighter or heavier atomic mass. The word of "isotope" was firstly introduced by Soddy based on his study on radioactive elements having the same intra-atomic charge but different atomic mass[89]. Soddy called it "isotope" because of "*isos*=equal" and "*topos*=place" in Greek, which indicates the isotopes of an element occupy the sample position in periodic table. At the same year, Thomson found the heavier neon atoms in discharge tube[90]. In 1920, Aston confirmed the existence of ^{20}Ne and ^{22}Ne by utilizing a mass spectrometer[91]. The isotope discovery led to the awarding of a Nobel prize in chemistry to Soddy in 1921 and Aston in 1922.

The atomic mass variances of isotopes directly change the atomic vibrational energy which can be described as a phonon, and usually can be characterized by phonon frequency and lifetime. The isotopic mass effect on phonons can be expressed as two factors: (1) average mass which is the mean of atomic mass for the isotopes of a given element, and (2) mass fluctuation which can be described as $g=\sum_{i,j}[c_{i,j}(1-M_{i,j}/M_{i,\mathrm{avg}})^2]$, where where $c_{i,j}$ and $M_{i,j}$ are the concentration and atomic mass of i-th atomic site and the j-th impurity, respectively, and $M_{i,\mathrm{avg}}$ is the average atomic mass of the i-th atomic site[92,93]. The frequency of optical lattice vibrations is expected to decrease with heavier atomic mass according to a simple two-atom basis one-dimensional harmonic oscillator model[94] as $\omega=[2C/(M_1^{-1}+M_2^{-1})]^{1/2}$ for zone center and $\omega=(2C/M_j)^{1/2}$, j = 1,2, for zone boundary phonons where C is the force constant and M_j is the mass of the j-th atom in the two atom basis chain. Regarding the mass fluctuation effect, the phonon frequency shift can be expressed as[95]

$$\Delta\omega=\frac{g\omega^2}{24}\int_0^{\infty}\frac{\omega'}{\omega_0-\omega'}N_{d1}(\omega')d\omega' \quad (1.2)$$

where g is the 2nd-order mass variance parameter, ω_0 is the original phonon frequency, $N_{d1}(\omega')$ is the phonon density of state at frequency ω'. The phonon lifetime can be expressed as $\tau=1/\Gamma$, where Γ is the phonon linewidth, usually obtained from the full width at half maximum (FWHM) of Raman spectra. First, we look at the average mass effect on phonon lifetime (or FWHM). When one phonon decays into two phonons, the FWHM of its Raman spectra is given as[95] $\Gamma=|V_3|^2N_{d2}(\omega_{0j})(1+n_{B1}+n_{B2})$, where V_3 is an anharmonic matrix element, $N_{d2}(\omega_{0j})$ is the density of states of the sum for two phonons into which the phonon of frequency ω_{0j} decays, n_{B1} and n_{B2} are the Bose-Einstein factors for the two phonons[95]. When T is close to 0 K, the anharmonic matrix element is proportional to $M^{-3/2}$, and the density of states is inversely proportional to $M^{1/2}$. So that we should expect that Γ is proportional to M^{-1} when T is close to 0 K. This relation between Raman FWHM and average mass was illustrated using isotopic Ge in which the intrinsic FHWM decreases with isotopic mass[96]. Next, we discuss about the mass fluctuation effect on phonon lifetime (or FWHM). The FWHM of a cubic monatomic crystal can be expressed as $\Gamma=g\omega^2N_{d1}(\omega_0)\pi/12$, where $N_{d1}(\omega_0)$ is the density of states of one phonon at frequency ω_0, and g is the mass fluctuation parameter[93], The Raman FWHM of a crystal with two different atoms in a primitive cell is $\Gamma=[g_cN_{d1c}(\omega_0)|e_c|^2+g_aN_{d1a}(\omega_0)|e_a|^2]\pi\omega_0^2/6$, where g the mass fluctuation parameter, e is the the orthonormal eigenvector corresponding to the Raman active optical phonon, subscript "a" and "c" represent anion and cation[97]. In above two cases, the FWHM is related to both average mass and mass fluctuation. Although the FWHM is expected to increase with larger mass fluctuation, this changes could be either very small as for Si or very large as for diamond[98].

Moreover, isotopes also effect on the optical band gap when the electron transition involves electron-phonon interactions. Electronic transitions from filled to empty states must conserve electron momentum. In a semiconductor with an indirect electronic band gap, the conduction band minimum (CBM) and valence band maximum (VBM) are not at the same electron momentum in reciprocal space. Since the momentum of photons is negligible, the electron transition between CBM and VBM must involve phonon assistance to obey the momentum conservation rule. Therefore, the band gap of an indirect semiconductor can be affected by the isotopes. It has been experimentally observed that the indirect band gap of Ge changes with the atomic mass, by ~2.2 meV between ^{70}Ge and ^{76}Ge[99]. Very recently, the indirect band gap renormalization energy changes of van der Waals *h*-BN was reported as ~4.4 meV between *h*-^{10}B^{NA}N and *h*-^{NA}B^{NA}N[88], where NA indicates a natural abundance isotopic composition.

In the macroscale, the isotopic effect also influences the thermal properties. It has been reported that the phonon scattering by isotopic impurities is an important mechanism for manipulating the thermal conductivity κ, such as for high-κ materials that are actively investigated for thermal management applications[100]. Experiments on 3-dimensional cubic crystals including diamond, silicon, and germanium[101-103] have shown that isotopic impurities considerably suppress the thermal conductivity at intermediate temperatures near the peak in κ. 2D structures such as single-layer graphene[21] and *h*-BN[104,105], as well as quasi-2D bulk graphite[106] and bulk *h*-BN[107], are known to possess high in-plane κ due to large crystallite sizes, light atomic masses, and strong interatomic bonding in the basal plane.

Although the isotopic effect has been reported in various bulk materials, it is still unexplored in the atomically thin TMDs due to the experimental difficulties, including the synthesis and characterization of atomically thin isotopic materials. Also, the isotopic effect cannot

be simply extended from bulk to atomically thin TMDs since they exhibit layer-number- (or thickness-) dependent phonon and optoelectronic properties. Thus, it is urgent to fill the gap in knowledge on the isotopic effect on phonon and optoelectronic properties in atomically thin TMDs.

1.1.4 Raman Spectroscopy in Atomically Thin Transition Metal Dichalcogenides

Raman spectroscopy is named after physicist Sir Chandrasekhara Venkata Raman who published the first paper of this technique at 1928[108] and received the Nobel Prize for physics at 1930. When photons scatter from a material system, most of the photons have the same energy as the incident light and the excited electrons go back to their original state, also known as Rayleigh scattering[109,110]. For inelastic scattering however, the scattered photons can be lower or higher energy than the incident photons, which defines the two types of Raman scattering: Stokes or anti-Stokes inelastic scattering. The energy loss/gain depends on the vibrational frequency of the molecule or crystal, which generally increases with bond strength. It has been reported that the phonon modes of atomically thin materials can be shifted by mechanical strain, which enables detection of strain using Raman spectroscopy[46,111].

However, not all vibrational modes are Raman active based on the selection rule - the polarizability of a molecule or crystal should change during vibration. Atomically thin MX_2 TMDs belong to the D_{3h} point group[112,113]. Table 1.3 shows the character table for D_{3h} point group. According to the irreducible representation, A_1' (x^2+y^2, z^2), E' (x^2-y^2, xy) and E'' (xz, yz) with quadratic terms are Raman active modes, whereas, A_2' (R_z), E' (x, y), and A_2'' (z) with linear terms are IR active modes. In IR characterization, the light will be absorbed when the frequency of IR is the same as the vibrational frequency of bonds[114]. By examination of the transmitted light, the frequency of IR active modes can be measured[114]. The E' Raman active mode (denotes the E_{2g}

mode in atomically thin TMDs) and A_1' Raman active mode (denotes the A_{1g} mode in TMDs) are the in-plane and out-of-plane vibrations, respectively. Another $A_1'^2$ (denotes the A_{1g}^2 mode in TMDs) only appears for layer numbers larger than 1[112]. The A_{1g}^2 mode corresponds to the interlayer vibrations involving both transition metal and chalcogen atoms.

Table 1. 3 Character table for D_{3h} point group atomically thin TMDs. D_{3h} point group has 1 identity (E), 2 three-fold rotational axis (C_3), 3 axis (C_2) perpendicular to C_3, 1 horizontal plane of symmetry (σ_h), 2 center of symmetry (S_3), 3 vertical plane of symmetry (σ_v). "1" denotes the sign of vector is unchanged by symmetry operation, whereas "-1" represents a sign change due to asymmetry operation.

D_{3h}	E	$2C_3$	$3C'_2$	σ_h	$2S_3$	$3\sigma_v$	Infrared (linear, rotation)	Raman (quadratic)
A_1'	1	1	1	1	1	1	-	x^2+y^2, z^2
A_2'	1	1	-1	1	1	-1	R_z	
E'	2	-1	0	2	-1	0	(x, y)	x^2-y^2, xy
A_1''	1	1	1	-1	-1	-1	-	
A_2''	1	1	-1	-1	-1	-1	z	
E''	2	-1	0	-2	1	0	(R_x, R_y)	(xz, yz)

Low-frequency Raman spectroscopy (~below 50 cm^{-1}) can further characterize the weak interlayer interaction in van der Waals materials. In TMDs, two low frequency Raman modes have been observed when the layer number is larger than one. Bilayer MoS_2 has the interlayer shear mode at ~23 cm^{-1}, and the interlayer breathing mode at ~36 cm^{-1} [115]. Bilayer WSe_2 exhibits the interlayer shear mode at ~18 cm^{-1}, and the interlayer breathing mode at ~28 cm^{-1} [115]. The weak interlayer van der Waals interaction can be affected by either strain, twisting or isotope engineering. The interlayer shear mode and breathing mode in MoS_2 bilayer has been observed to be sensitive to the twist angle between layers, in which the frequency variation can be up to 8 cm^{-1} [116]. For the isotopic effect, both low frequency shear and breathing modes "red-shift" with isotope mass in *h*-BN[88].

1.2 Motivation and Scope of This Thesis

In view of the above-mentioned extraordinary properties of atomically thin van der Waals materials, it is urgent and beneficial to understand the mechanisms and explore new phenomenon of optoelectronic and photonic transport in these materials. To achieve this goal, the challenges include: (i) identifying the mechanisms of strain effects on optoelectronic properties has been limited by difficulty in quantifying atomic-level strain experienced by an atomically thin material, (ii) the mechanism responsible for recent spatial control of quantum emitters based on high density, dielectrically non-uniform pillars[7,8] remains unclear, as does the generality of conclusions based on these studies, (iii) the isotopic effect on the electronic band gap was only examined on bulk vdW materials, such as *h*-BN with a large band gap of ~5.2 eV. It remains to be further explored in other atomically thin vdW materials with smaller band gaps and different symmetry (e.g. the MX_2 TMDs) which are more suitable for nanoelectronics, optoelectronic, and quantum emission applications.

Based on the above motivation, the aims of this thesis are to (i) understand the strain coupled-phonon and optoelectronic transport in atomically thin vdW semiconductors; (ii) establish a route to create locally defined atomically thin single photon quantum emitter with scalability to wafer-scale; (iii) explore the isotopic effects on phonon dispersion and optical band gap energy of atomically thin semiconducting TMDs. Accordingly, these studies, which focus on bilayer WSe_2, are presented in the next four chapters:

Chapter 2 reports a high repeatability chemical vapor deposition (CVD) method for monolayer MoS_2 and bilayer WSe_2 using our own custom designed and built CVD system. The monolayer MoS_2 was synthesized in both mass-limited and diffusion-limited growth conditions. The mass-limited growth showed uniform properties examined by AFM and spatial Raman and photoluminescence mapping. Whereas the diffusion-limited growth monolayer MoS_2 had tiny nucleation dots on the surface and a rounded profile resulting in non-spatially uniform Raman and PL spectra. Bilayer WSe_2 was also synthesized by a CVD method. In contrast with previous reports, the top and bottom layers of our WSe_2 had the same dimension and lattice orientation. The crystals showed spatially uniform Raman spectra and thickness. The bilayer structure was further examined by cross-section scanning transmission electron microscopy (STEM).

Chapter 3 examines the strain effect on optoelectronic and phonon dispersion in a WSe_2 bilayer grown by CVD. The crystal structure was characterized by confocal Raman spectroscopy, atomic force microscopy (AFM), and cross-sectional STEM. The WSe_2 bilayer was transferred and encapsulated by two thin poly(methyl methacrylate) (PMMA) layers laid on a flexible poly(ethylene terephthalate) (PET) substrate for a better strain transfer rate and larger applied uniaxial tensile strain. The Grüneisen parameter was obtained by interpreting the strain dependent Raman spectra using a 3-dimensional Poisson effect analysis model which was derived an

implemented in this thesis. Through comparison of the Grüneisen parameter of graphene also obtained in this thesis and that from a previous report[50], the strain transferred to the 2D materials was verified. The strain dependent optoelectronic response was studied using photoluminescence (PL) spectroscopy. The electronic band gap evolution was examined by deconvolution of the PL emission peak to indirect and direct electronic transition sub-peaks. A two-order of magnitude PL intensity enhancement was observed at a maximum of 3.59% uniaxial tensile strain.

Chapter 4 presents a method to create highly spatially localized and well-separated emission sites in a continuous epitaxial film of nominally bilayer WSe_2. To separate the effects of mechanical strain from substrate or dielectric-environment induced changes in the electronic structure, the continuous epitaxial bilayer WSe_2 was transferred onto isotropically etched silicon dioxide tip arrays. The second order photon correlation was measured as ~0.3, which confirms the single photon emission phenomenon occurring at the tips. Other types of defects created during sample transfer process were also examined by cryo-temperature spatial PL spectra.

Chapter 5 investigates the isotope effect on phonon dispersion and optical band gap energy in naturally abundant $^{NA}W^{NA}Se_2$ and isotopically purified $^{186}W^{80}Se_2$ bilayers. Both samples are grown using CVD under the same growth conditions to eliminate measurement uncertainty from other factors besides isotopes. The spatially resolved Raman and PL spectra showed the uniformity of the bilayer samples. A slightly shorter interlayer van der Waals spacing was obtained by X-ray diffraction for $^{186}W^{80}Se_2$ than for naturally abundant $^{NA}W^{NA}Se_2$. We demonstrated a higher and nearly temperature independent optical band gap energy in bilayer $^{186}W^{80}Se_2$ than in bilayer $^{NA}W^{NA}Se_2$ (by 3.92±0.71 meV from 4.41 K to 300 K) likely due to the renormalization of electronic states. The phonon frequencies decrease in the isotopically pure crystal due to the atomic

mass dependence of harmonic oscillations, with correspondingly longer optical phonon lifetimes than in the naturally abundant sample over a temperature range of 4-300 K.

Chapter 2: Synthesis of Atomically Thin Transition Metal Dichalcogenides

2.1 Chemical Vapor Deposition System

Chemical vapor deposition (CVD) system usually contains 4 major components: carrier gas supply, reaction chamber, temperature control element and pump system. For atomically thin transition metal dichalcogenide materials, such as MoS_2 and WSe_2, the growth prefers to be performed at atmospheric pressure for lower precursor sublimation rate in order to better control of growth parameters[2,35,117]. The oxygen residual inside the system also needs to be minimized pre-growth for better quality crystal growth. Thus, the modified CVD system with fast switching between vacuum mode and atmospheric pressure mode was designed and built. The scheme of the modified CVD system is illustrated in Figure 2.1.

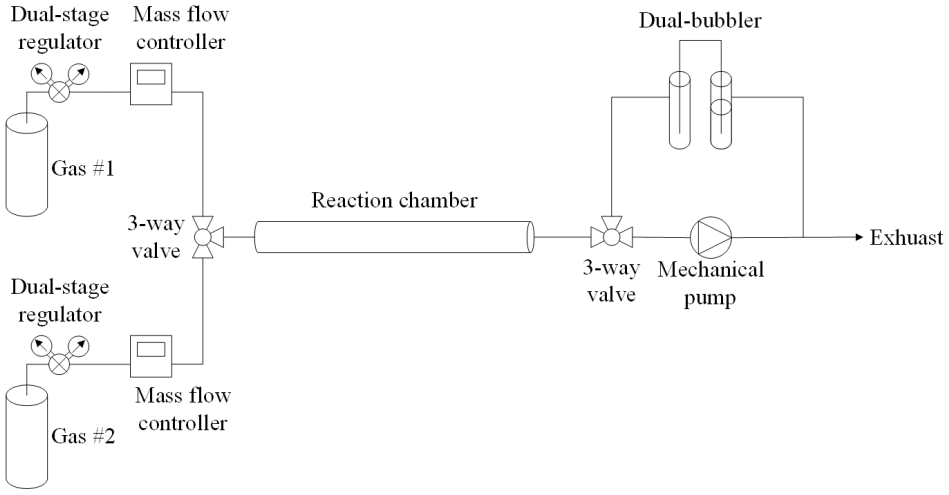

Figure 2. 1 Schematic of the CVD system with capability of both vacuum and atmospheric pressure. The carrier gas is selected by a 3-way valve. The system pressure can be switched between vacuum and atmospheric pressure by switching the downstream system from pump to bubbler. A dual-bubbler is used to prevent the sealant (silicone oil) from flowing back into the stainless steel gas line.

The modified CVD system contains multiple gas sources for different materials, such as N_2 for MoS_2 growth and forming gas $H_2(5\%)/N_2$ for WSe_2, which can be switched by the upstream 3-way valve. The carrier gas flow was controlled by a digital mass flow controller. The reaction chamber was made of quartz for high temperature growth (maximum growth temperature 1100°C). Prior to growth, the CVD reactor was pumped for hours to a rough vacuum pressure lower than 10^{-4} mbar in order to minimize residual oxygen. Then the downstream 3-way valve was switched off, and carrier gas was selected and injected into system. Once the pressure reaches atmospheric pressure, the 3-way valve was switched to the dual-bubbler system which can prevent sealing oil flowing back into the gas line. Since the inner volume of the CVD system between the two 3-way valves was relatively small, it was fast to pump down this part and to fill to atmospheric pressure. The exhaust can contain S or Se residuals and cause health issues to human, thus it is necessary to connect the exhaust to a fume hood.

2.2 Monolayer MoS_2 Single Crystals

2.2.1 Synthesis of Monolayer MoS_2 Single Crystals

MoS_2 monolayers are synthesized by CVD method using powder precursors. 200 mg of MoO_3 powder (Sigma Aldrich, 99.9% purity) in a crucible was placed in the center of a one-zone furnace fitted with a 1-inch diameter quartz tube. Sulfur powder in another crucible was placed upstream outside furnace where the temperature remains ~130°C during growth. A piece of ~285 nm thick SiO_2 on 500 μm Si wafer was placed polished-side-down on the crucible containing the MoO_3 powder. After several hours pumping down, the CVD reactor was filled by N_2 as a carrier gas until atmospheric pressure. The N_2 gas was set to 10 cm^3min^{-1} during growth, and the growth was performed using a sealed bubbler filled with silicone oil (Sigma Aldrich) to maintain

atmospheric pressure. The reaction chamber was heated to 700°C with ramp rate at 10 °C/min, then stay at 700°C for 10 minutes. After the growth, the system was cooled to 450°C in 20 minutes, followed by natural cooling to room temperature with the furnace lid open. The synthesis schematic illustration is shown in Figure 2.2. The critical growth parameter was identified as the sulfur introduction time. Early sulfur introducing time results in less or no growth. This is due to the fact that most of the MoO_3 was "poisoned" (totally reduced) by sulfur before it sublimates if sulfur introduced too early in the growth. Nevertheless, later sulfur introducing time results in mass limited growth which was caused by a lower sulfur vapor pressure in the reaction chamber.

Figure 2. 2 Schematic illustration of the CVD growth of MoS_2.

2.2.2 Atomic Force Microscopy Analysis and Optoelectronic Characterization of Monolayer MoS_2 Single Crystals

It has been reported that the atomically thin van der Waals materials, such as graphene, can be seen under visible light by choosing SiO_2 thickness[118]. Figure 2.3a gives the optical microscopy image of the CVD grown monolayer MoS_2 where the monolayer showing purple color on SiO_2 (285 nm)-on-Si. The deposition at the center of wafer usually has thick growth due to high

precursor vapor density. Towards the edge of wafer, the deposition shows continuous few-layer to monolayer MoS_2, and isolated triangle shape MoS_2 monolayers at the edge due to lower Mo precursor vapor density.

Figure 2.3b gives the multi-energy Raman spectra of MoS_2 monolayer on SiO_2-on-Si substrate. Both spectra using 488 nm wavelength blue laser (2.54 eV) and 514 nm wavelength green laser (2.41 eV) show the E_{2g} and A_{1g} vibrational modes. The Raman spectra using 785 nm wavelength laser shows no Raman active peak. This is due to the observed electron band gap energy of MoS_2 monolayer is at 1.83 eV, which is larger than the photon energy at 1.58 eV of the 785 nm wavelength laser.

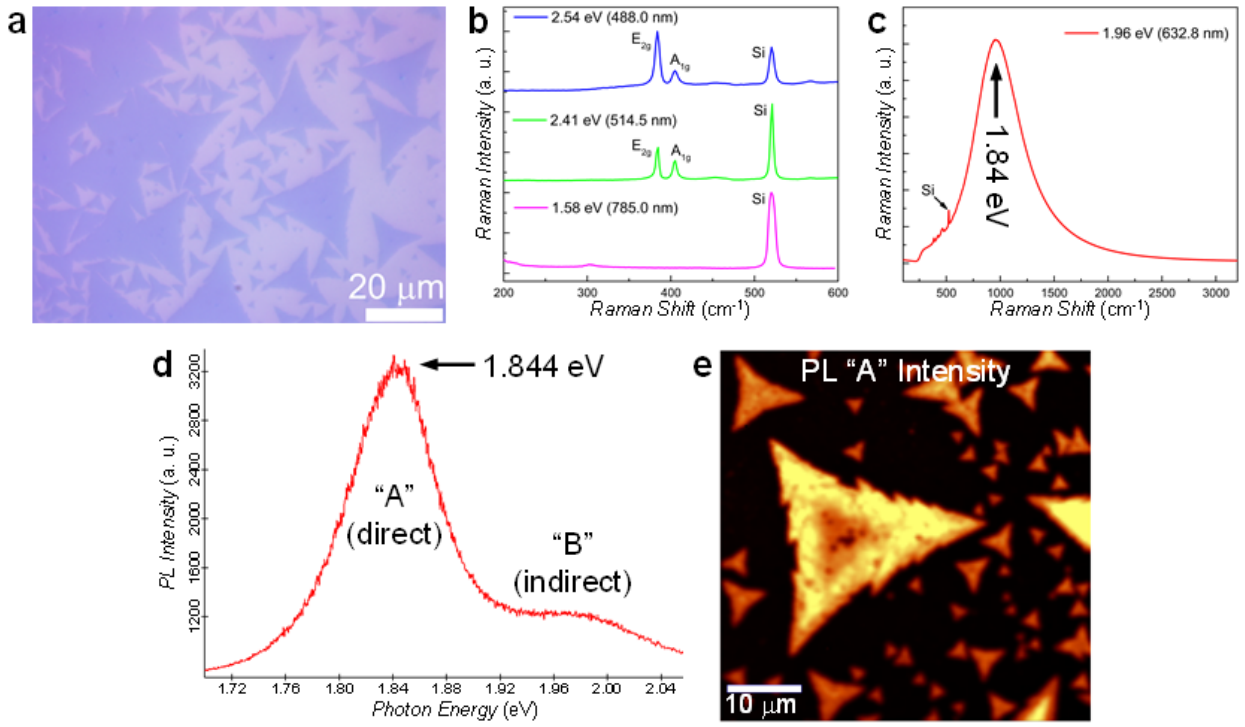

Figure 2. 3 Optical characterization of MoS_2 monolayers on SiO_2 (258 nm)-on-Si substrate. (a) Optical microscopy image of MoS_2 monolayers. (b-c) Multi-energy Raman spectra of MoS_2 monolayer using the Si Raman peak for calibration. (d-e) Photoluminescence.

Although the synthesis was supposed to be at the equilibrium condition, the mismatch of Mo- and S- vapor pressure ratio can result in mass limited growth where the number of Mo and S atoms does not have the correct ratio as 1:2. Figure 2.4 and 2.5 show the diffusion and mass limited growth of MoS_2, respectively, where the diffusion limited growth results in triangular crystals while mass limited growth results in rounded-triangular shapes. The precursor amount, MoO_3 temperature, carrier gas flow rate, and other growth conditions are all the same in the mass limited growth as for the diffusion limited growth condition, however, the sulfur temperature was slightly lower for the diffusion limited growth, ~120°C as measured by thermocouple tapped outside the quartz tube versus ~130°C for the mass limited growth. For mass limited growth, majority region of the crystal was monolayer with thickness ~0.7 nm as the atomic force microscopy analysis shows in Figure 2.5 b. However, there are nucleation dots on top of the monolayer. The photoluminescence mapping shows non-uniform optical band gap over the crystal region. The flat region at the edge of the crystal exhibits a lower band gap of 1.875 eV, whereas the center region containing dense nucleation dots has a higher band gap energy of 1.885 eV.

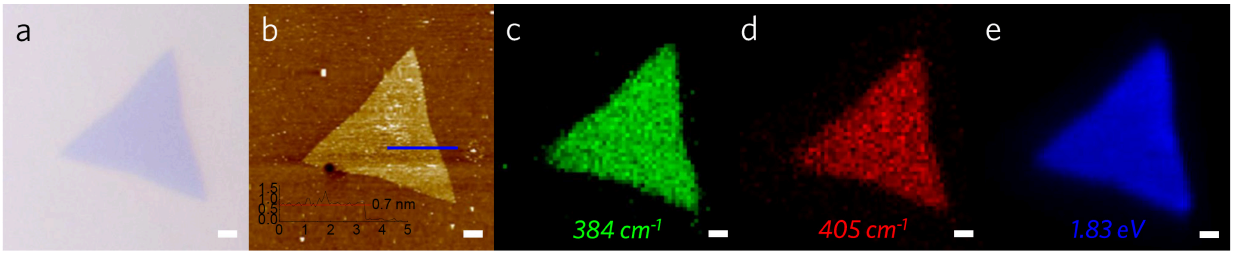

Figure 2. 4 Characterization of diffusion limited growth of an MoS_2 monolayer. (a) Optical image of MoS_2 monolayer single crystal, (b) Atomic force microscopy analysis of MoS_2 monolayer with uniform thickness ~0.7 nm. Spatially resolved Raman intensity at (c) 384 cm^{-1} (E_{2g} mode), (d) 405 cm^{-1} (A_{1g} mode). (e) Spatially resolved photoluminescence shows uniform distributed optical band gap as 1.83 eV. The scale bar is 1 μm in all panels.

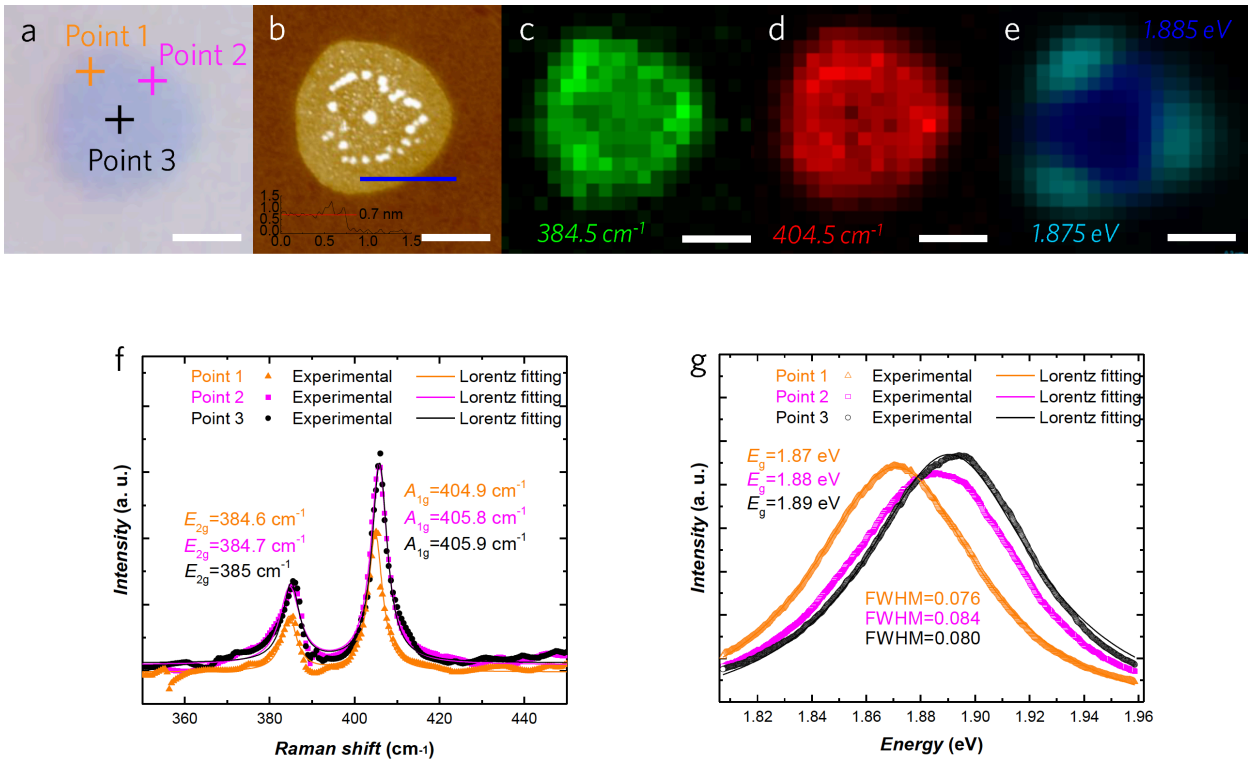

Figure 2. 5 Characterization of mass limited growth of an MoS_2 monolayer. (a) Optical image of MoS_2 monolayer and (b) atomic force microscopy analysis of MoS_2 monolayer with thickness ~0.7 nm at the flat region. Spatially resolved Raman intensity at (c) 384.5 cm^{-1} (E_{2g} mode), (d) 404.5 cm^{-1} (A_{1g} mode). (e) Spatially resolved photoluminescence mapping at 1.835 eV (blue color) and 1.875 eV (cyan color). (f) Point Raman spectra at 3 locations using 514 nm laser excitation. (g) Point photoluminescence spectra at 3 locations using 514 nm. The corner shows lower optical band gap of 1.875 eV, whereas the center region has higher optical band gap of 1.885 eV. The scale bar is 1 μm in all panels.

2.3 Naturally Abundant Bilayer WSe_2 Single Crystals

2.3.1 Synthesis of Naturally Abundant Bilayer WSe_2 Single Crystals

At only six atoms in thickness, WSe_2 bilayers are grown reproducibly by a chemical vapor deposition (CVD) method which can also be described as powder vaporization similar as previous reports[117,119]. A crucible containing 200 mg of WO_3 powder (Sigma Aldrich, 99.9% purity) was placed in the center of a one-zone furnace fitted with a 1-inch diameter quartz tube. Another crucible containing 200 mg of Se powder (Alfa Aesar, 99.999% purity) was placed upstream at the edge of heating zone, which operates at a lower temperature during growth. Crystal growth occurs on a silicon substrate with a ~285 nm-thick SiO_2 film placed polished-side-down on the crucible containing the WO_3 powder. Prior to growth, the CVD reactor was pumped to a rough vacuum pressure lower than 10^{-4} mbar, followed by injection of gaseous H_2 (4.992%)/N_2 (balance) (Airgas, 99.999% purity) at 100 cm^3min^{-1} to purge the system. Once atmospheric pressure was reached, the H_2/N_2 flow was reduced to 50 cm^3min^{-1}, and the growth was performed using a sealed bubbler filled with silicone oil (Sigma Aldrich) at the exhaust to maintain 1000 mbar pressure and prevent air from diffusing back into the reaction chamber. The system was heated to 1000°C in 1 hour, then keep at 1000°C for 15 minutes. During the growth, the Se temperature was measured as ~290°C by a thermocouple taped to the outside of the quartz tube. The system was cooled to 750°C in 20 minutes; followed by rapid cooling achieved by opening the furnace lid. We have identified that a critical parameter in successful growth of WSe_2 bilayer single crystals with uniform thickness is the time at which Se vapor was introduced into the chamber, which can be finely tuned by adjusting the position of the Se crucible. We achieve high yield growth by introducing Se when the furnace center's thermocouple reads ~820°C. We observe that introducing Se too early in the growth results in small grain sizes and non-uniform thickness likely due to

poisoning of the metal oxide source powder, which reduces the tungsten precursor concentration. Introducing Se too late results in thicker samples as thick tungsten oxyselenide nucleation on the substrate was reduced to WSe_2.

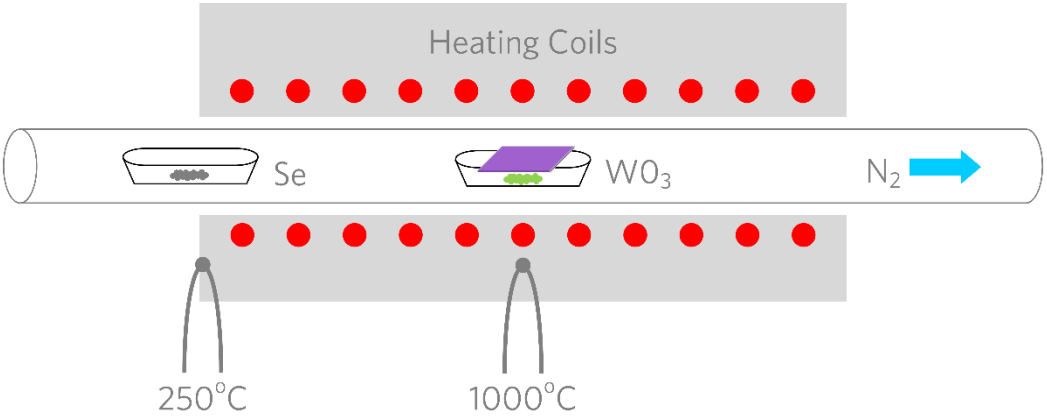

Figure 2. 6 Schematic illustration of the CVD growth of WSe_2.

2.3.2 Atomic Force Microscopy Analysis of Naturally Abundant Bilayer WSe_2 Single Crystals

Figure 2.7 shows a WSe_2 bilayer crystallite with a uniform thickness of ~1.3 nm, in accordance with the out-of-plane unit cell parameter of AB-stacked bulk WSe_2, which was 12.9825 Å (Powder Diffraction File no. 38-1388)[120]. The growth results in grain sizes on the order of 5–18 μm. In contrast to previous multilayer CVD growth reports for TMDs[121], our WSe_2 bilayer are synthesized so that the top and bottom layers possess the same dimensions (up to ~15 μm).

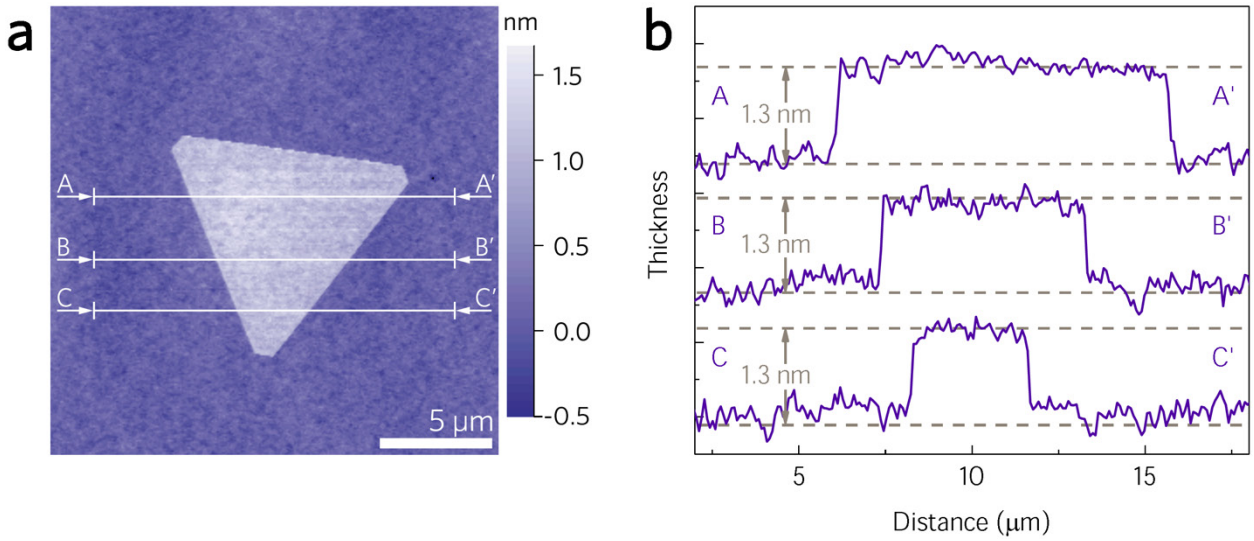

Figure 2. 7 Atomic force microscopy (AFM) analysis of naturally abundant WSe_2 bilayer single crystal. (A) AFM mapping of the entire domain demonstrates uniform thickness across the crystallite. (B) Cross-sectional height profiles demonstrate the thickness of WSe_2 bilayer single crystal is approximately 1.3 nm and is consistent with the *c*-axis unit cell parameter for AB-stacked WSe_2 (1.2983 nm, Powder Diffraction File #38-1388)[120].

2.3.3 Cross-sectional Scanning Transmission Electron Microscopy of Naturally Abundant Bilayer WSe_2 Single Crystals

The cross-sectional Transmission Electron Microscopy (STEM) sample was prepared using a Ga^+ Focused Ion Beam (FIB, FEI Helios Nanolab 460F1). The WSe_2 on SiO_2-on-Si crystal was first aligned so that the lamella can be prepared along a certain crystallographic direction, namely $\langle 10\bar{1}0 \rangle$ or $\langle 2\bar{1}\bar{1}0 \rangle$. To prevent sample damage caused by gallium ion bombardment, the WSe_2 was first coated with carbonaceous platinum by electron beam induced metal deposition (EBIMD) at 5 kV and 13 nA. As shown in Figure 2.8, the triangular shape of the WSe_2 bilayer

was still observable after 10 minutes EBIMD of platinum. A thicker Pt coating, ~2 μm in thickness, was subsequently deposited using the Ga^+ ion beam at 30 kV and 80 pA and acts as the sacrificial protective layer for ion milling. The lamella was then cut by the Ga^+ beam at 30 kV and 2.5 nA. The lamella was lifted off and loaded onto the side of a FIB lift-out TEM grid as a 'flag' to avoid copper re-deposition from the grid during the thinning and polishing processes. During the polishing step, the Ga^+ ion beam milling power was gradually reduced to 8 kV and 21 pA to avoid sample damage. STEM images were acquired using the Lawrence Berkeley National Laboratory Molecular Foundry's Transmission Electron Aberration-corrected Microscope (TEAM) 0.5 at 80 kV. STEM analysis clearly reveals the bilayer structure with an interlayer distance ~0.7 nm (Figure 2.9 b and c).

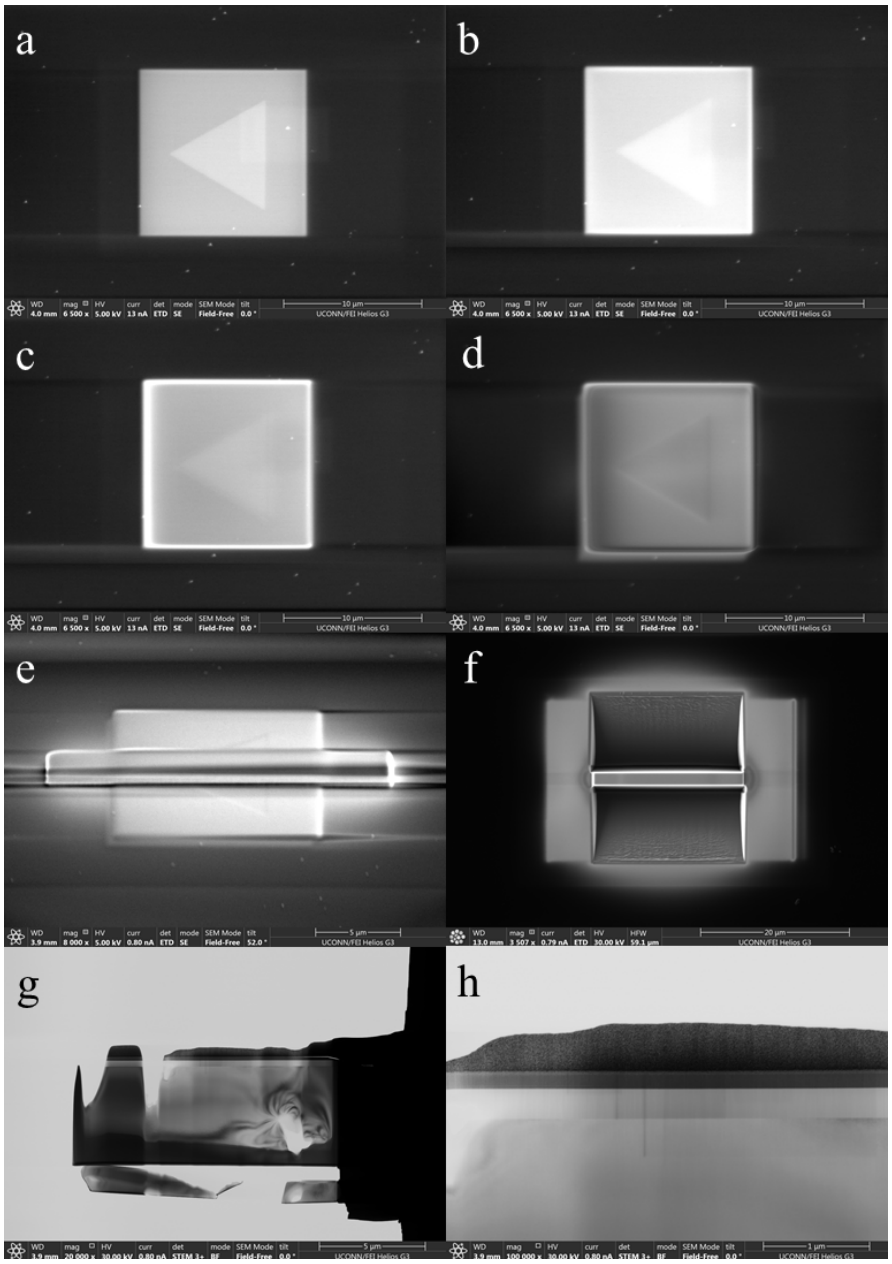

Figure 2. 8 Cross-sectional scanning transmission microscopy (STEM) sample prepared by Focused Ion Beam (FIB). Platinum protective layer coated by electron beam induced metal deposition after (a) 30 second, (b) 2 minutes, (c) 4 minutes, (d) 10 minutes deposition time. (e) Platinum protective layer coated by Ga^+ ion beam induced metal deposition. (f) Ga^+ beam image after etching and polishing. (g) STEM bright field image of transferred laminate on copper grid. (h) STEM bright field image of the laminate showing Ga^+ Pt/e-beam Pt/WSe_2/SiO_2/Si.

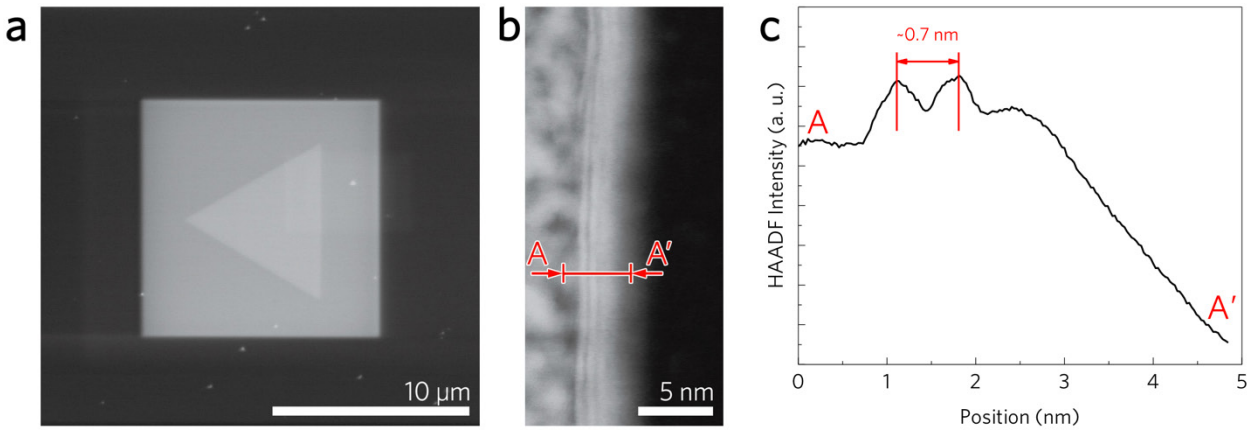

Figure 2. 9 STEM of a WSe_2 bilayer single crystal. (a) Scanning electron micrograph showing a WSe_2 bilayer single crystal (bright triangle) and a thin electron-beam deposited platinum coating (bright square) used in the cross-sectioning process. (b) Cross-sectional high-angular annular dark-filed (HAADF) STEM analysis shows the bilayer structure of the CVD-grown WSe_2. (c) Line profile of the HAADF intensity along the length of the red line drawn in (b). The interlayer distance is measured as ~0.7 nm and is in agreement with the {0002} interplanar spacing of WSe_2 (d_{0002}=0.6493 nm, Powder Diffraction File #38-1388)[120]. The STEM image and profile shown in panels (b-c) were obtained by Dr. Peter Ercius at the Lawrence Berkeley National Laboratory Molecular Foundry's National Center for Electron Microscopy using the TEAM 0.5 instrument.

2.3.4 Optoelectronic Characterization of As-grown Naturally Abundant Bilayer WSe_2 Single Crystals

The Raman spectra of a WSe_2 bilayer were obtained using a 2.33 eV (λ = 532 nm) continuous wave excitation at low power (86 μW) to avoid sample damage and spectral shifts due to local heating effects[47]. The spatially dependent Raman spectra of as-grown bilayer WSe_2 on SiO_2-on-Si substrate was uniform in intensity throughout the entire crystallite for the E_{2g}, A_{1g} and A^2_{1g} Raman active modes as Figure 2.10 shows.

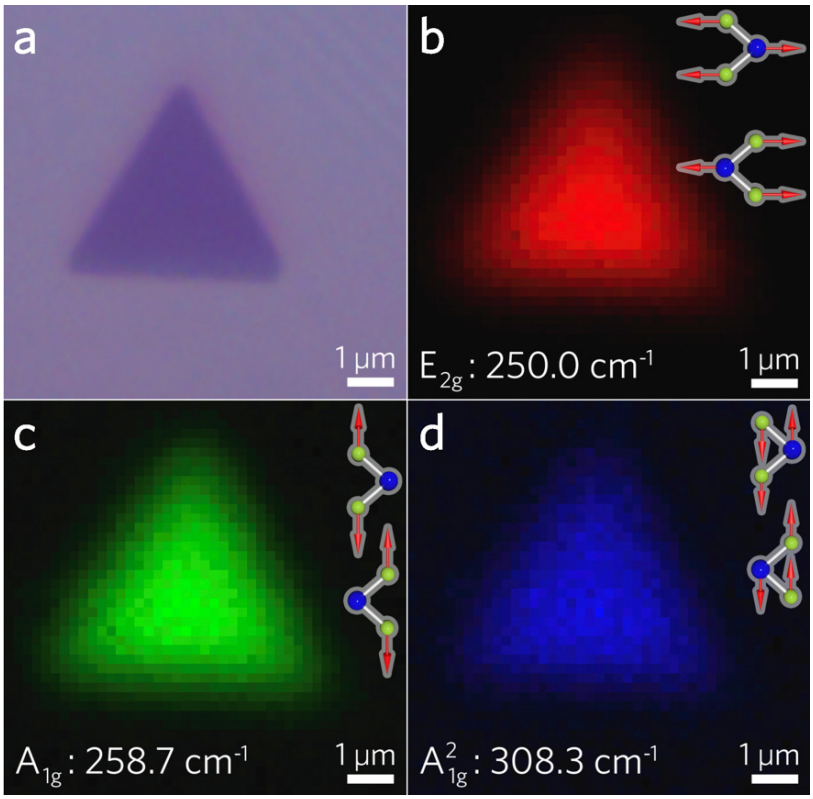

Figure 2. 10 Spatially dependent Raman intensity of WSe_2 bilayer single crystal. (a) Optical image of bilayer WSe_2 on SiO_2-on-Si substrate. Spatially resolved Raman intensity at (b) 250 cm^{-1} (E_{2g} mode), (c) 258.7 cm^{-1} (A_{1g} mode), and (d) 308.3 cm^{-1} (A^2_{1g} mode). Vibrational modes are depicted schematically in panels (b–d).

2.4 Isotopically Pure Bilayer WSe_2 Single Crystals

2.4.1 Synthesis of Isotopically Pure Bilayer WSe_2 Single Crystals

Isotopically pure $^{186}W^{80}Se_2$ bilayers are grown by a CVD method[39] similar as naturally abundant samples. 200 mg of $^{186}WO_3$ (ISOFLEX USA, >99.90% purity) in a crucible was placed in the center of furnace equipped with a 1-inch diameter quartz tube. 200 mg of ^{80}Se powder (ISOFLEX USA, >99.90% purity) was loaded into a separate crucible placed upstream at the edge of the furnace heating zone. Tungsten diselenide crystals are grown on a single-side-polished SiO_2(285 nm thickness)-on-Si substrate placed polished-side-down on top of the crucible containing the $^{186}WO_3$ powder. The CVD reactor was first pumped to lower than 10^{-4} mbar by a mechanical pump, followed by injection of gaseous H_2 (4.992%)/N_2 (balance) (Airgas, 99.999% purity) at 100 cm^3min^{-1}. Once the pressure in the growth chamber was raised to atmospheric pressure, the exhaust of CVD system was switched to a sealed bubbler filled with silicone oil (Sigma-Aldrich) in order to maintain atmospheric pressure and prevent air from diffusing back into the system. The flow rate of H_2/N_2 was then reduced to 50 cm^3min^{-1} for the growth. The furnace temperature during growth was set at 1000°C, while the Se temperature was measured to be ~290°C. By adjusting the position of Se crucible, we optimized the time at which Se vapor was introduced in order to grow the bilayer tungsten diselenide single crystals with uniform thickness. High yield growth was achieved by melting the ^{80}Se powder when the center of the furnace reached ~820°C. After the growth, the reactor was cooled to 750°C in 20 minutes; and then rapidly cooled to room temperature by opening the furnace lid.

2.4.2 X-ray Diffraction Characterization of Naturally Abundant and Isotopically Pure WSe_2

A Bruker D5005 X-ray diffractometer with Cu K_α radiation (λ = 1.54184 Å) operated at 40 kV and 40 mA was used to perform X-ray diffraction (XRD) measurements at room temperature. XRD analysis for *d*-spacing and crystallite size was performed by peak profile fitting with a pseudo-Voigt function using MDI Jade software. Room temperature X-ray diffraction (XRD) patterns for $^{NA}W^{NA}Se_2$ and $^{186}W^{80}Se_2$ are shown in Figure 2.11. The Si (004) peak position of the substrate at 2θ = 69.173° (Powder Diffraction File no. 05-0565) was employed as reference to correct for specimen displacement. The diffractograms of the thin films were referenced to a hexagonal phase of tungsten diselenide (P63/mmc, space group 194, Powder Diffraction File no. 38-1388[S120]). Since the X-ray beam size was on the order of a millimeter, the signal was collected from an ensemble average of deposited materials and allows for unit cell parameter refinements to be performed. All XRD patterns were aligned using the silicon peak to compensate for any peak shifts arising from height differences in sample mount. The XRD analysis for *d*-spacing and crystallite size was performed by peak profile fitting with a pseudo-Voigt function using MDI Jade software. The diffractograms of the thin films were referenced to a hexagonal phase of WSe_2 (P63/mmc, space group 194, powder diffraction file #38-1388)[120]. Besides the expected Si (004) peak at 2θ = 69.173°, the XRD patterns displayed four distinct characteristic peaks assigned to the (002), (004), (006) and (008) crystal planes of WSe_2, indicating the thin films are all oriented along the *c*-axis. The interlayer spacing determined from the (002) peak was 6.467 Å and the *c*-lattice parameter was 12.9341 Å for the $^{NA}W^{NA}Se_2$ samples, whereas the (002) interlayer spacing and the *c*-lattice parameter were 6.464 Å and 12.9298 Å for $^{186}W^{80}Se_2$ samples. The *c*-lattice parameter difference between $^{NA}W^{NA}Se_2$ and $^{186}W^{80}Se_2$ was relatively small at only 0.033 %, where the XRD

instrumental uncertainty after Rietveld refinement in this thesis was on the order of 9.5%. Heavier atomic mass isotopes tend to exhibit smaller van der Waals radii; the van der Waals radius of deuterium (^{2}H) was ~1.15 Å, whereas that of hydrogen (^{1}H) was ~1.20 Å[122]. By calculating the ratio of relative van der Waals radius change to relative change in atomic mass, we note that the small difference we observe in the *c*-axis unit cell parameter for WSe_2 (-0.027) actually corresponds well to that expected for hydrogen (-0.042). Although it was hard to draw a further quantitative conclusion of the isotopic effect on lattice parameters due to the instrumental uncertainty, the subsequent analysis indicates that such small lattice parameter changes were expected to have a negligible effect on the phonon dispersion and optical band gap in comparison to the isotope effect, which will be illustrated in Chapter 5.

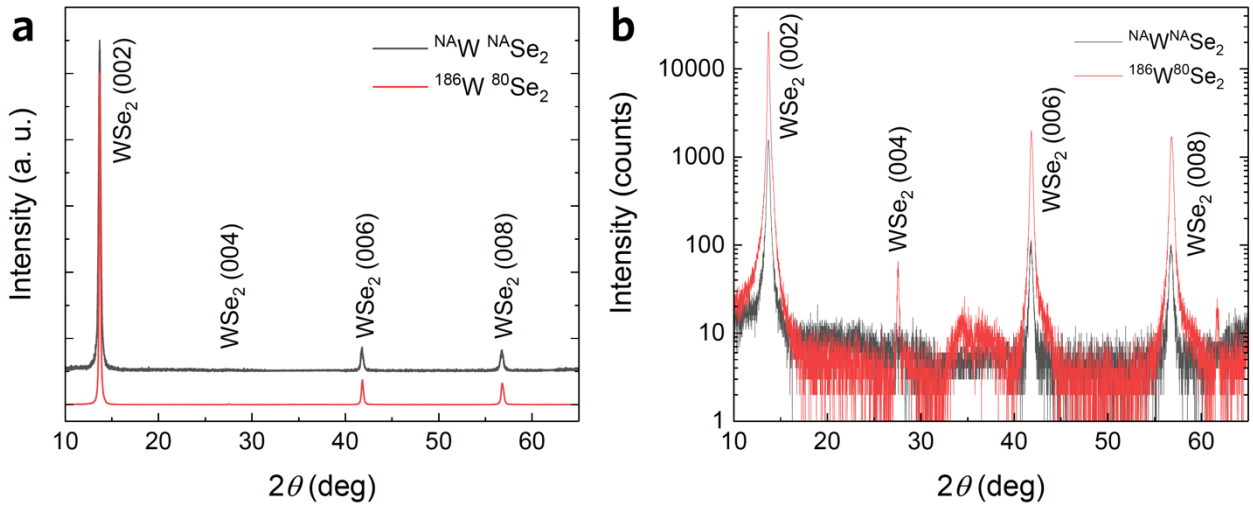

Figure 2. 11 (a) Linear- and (b) log-scale XRD spectra of naturally abundant $^{NA}W^{NA}Se_2$ (black line) and isotopically pure $^{186}W^{80}Se_2$ (red line). The diffractograms are aligned to the Si (004) peak to correct for specimen displacement.

2.4.3 Atomic Force Microscopy and Optoelectronic Characterization of Isotopically Pure Bilayer WSe_2 Single Crystals

Raman and photoluminescence spectroscopy were conducted on a Horiba LabRAM HR Evolution system. The spatially dependent room-temperature spectra were obtained using 2.33 eV (λ=532 nm) continuous wave laser excitation with a beam diameter on the order of 250 nm and total power of 86 μW measured by a THORLABS PM100D power meter. Power was kept below 100 μW to avoid sample damage or spectra shifts due to local heating effects. The integration time was 1 s and 2 s for spatially dependent Raman and photoluminescence maps, respectively. The gratings used were 1800 grooves/mm for Raman, and 600 grooves/mm for photoluminescence.

For temperature dependent Raman and photoluminescence analysis, both $^{NA}W^{NA}Se_2$ and $^{186}W^{80}Se_2$ samples on SiO_2-on-Si were mounted into a Janis Microscopy Cryostat ST-500 optical cryostat while a continuous liquid helium flow was supplied. Before cooling, the sample chamber was pumped to lower than 10^{-6} mbar. The sample mount temperature was controlled by a Lakeshore 335 temperature controller. The system was stabilized at each set-point temperature for at least 1 hour before characterization. To avoid non-uniform temperature distribution within or between samples, all the Raman spectra were aligned using the silicon peak at each temperature. The integration time was 4 s for Raman and 6 s for photoluminescence spectroscopy, respectively. The gratings used were 1800 grooves/mm for Raman, and 600 grooves/mm for photoluminescence.

Since the optical band gap is extremely sensitive to strain and crystalline quality[39,123,124], the $^{NA}W^{NA}Se_2$ and $^{186}W^{80}Se_2$ bilayers were synthesized under identical growth conditions, eliminating differences in structure caused by thermal expansion mismatch with the substrate[125]. To isolate the isotopic effect from the layer number[32,126] and edge effect[127] contributions to the

optical band gap, Fig. 2.12 demonstrates our bilayer WSe_2 single crystals were synthesized so that the top and bottom layers have the same lateral dimensions. Atomic force microscopy (AFM) analysis shows a uniform thickness of ~1.3 nm over the entire crystallite for both $^{NA}W^{NA}Se_2$ and $^{186}W^{80}Se_2$ bilayers (Fig. 2.12 b-c). Fig. 1.12 d-f illustrates that the Raman spectra of an isotopically pure bilayer $^{186}W^{80}Se_2$ crystallite was spatially uniform in intensity throughout the entire crystallite for the E_{2g}, A_{1g} and A^2_{1g} Raman active modes, which is similar as our previous reported naturally abundant bilayer $^{NA}W^{NA}Se_2$[39]. Photoluminescence (PL) also demonstrates spatially uniform peak intensity and in the entire crystallite (Fig. 2.12 g), further indicating the uniformity of atomic-level thickness.

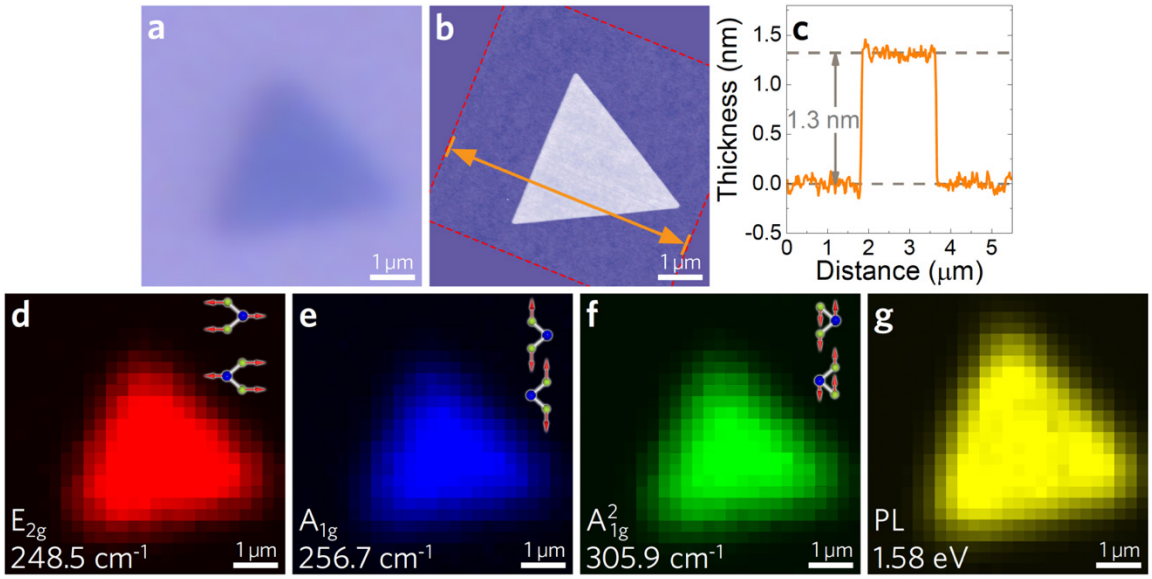

Figure 2. 12 Spatially dependent characterization of an isotopically pure bilayer $^{186}W^{80}Se_2$ crystal. (a) Optical image and (b) atomic force microscopy (AFM) characterization of $^{186}W^{80}Se_2$ on a 285 nm SiO_2-on-Si substrate. (c) AFM height profile corresponding to line shown in (b). Spatially resolved Raman intensity at (d) 248.5 cm^{-1} (E_{2g} mode), (e) 256.7 cm^{-1} (A_{1g} mode), and (f) 305.9

cm^{-1} (A^2_{1g} mode), where the vibrational modes are depicted schematically. (g) Spatially resolved photoluminescence (PL) intensity at the peak emission wavelength of 1.58 eV.

2.5 Conclusion

In this chapter, a modified chemical vapor deposition system with fast switching between vacuum and atmospheric pressure was designed and built. The dual-bubble helps prevent seal oil to flow back to gas lines. Using this CVD system, monolayer MoS_2 was synthesis in both diffusion and mass limited conditions. The diffusion limited growth shows uniform thickness, Raman spectra and photoluminescence spectra over the entire triangle shape domain region, whereas, the mass limited grown MoS_2 monolayer has tiny nucleation dots to the surface. The non-uniform photoluminescence mapping of limited grown MoS_2 monolayer indicates non-uniform band gap energy, where the flat region behaves lower band gap than the region having nucleation dots.

The naturally abundant WSe_2 bilayer was also synthesized by CVD method. In contrast with previous reports, the top and bottom layers of our bilayer WSe_2 has the same dimension and lattice orientation. The spatial Raman mapping shows the uniform phonon vibration mode over the entire crystal region. The bilayer structure has been further examined and confirmed by cross-sectional scanning transmission electron microscopy analysis.

Furthermore, the isotopically pure $^{186}W^{80}Se_2$ bilayer was also synthesized by using the same growth conditions as naturally abundant $^{NA}W^{NA}Se_2$ bilayer. The single crystal shows uniform thickness as the naturally abundant sample. Both spatial Raman and photoluminescence spectra indicates the uniform properties over the entire crystal region. The XRD shows $^{186}W^{80}Se_2$ has slightly shorted vdW bonds.

Chapter 3: Strain Dependent Optoelectronic Behavior in Atomically Thin Transition Metal Dichalcogenides

3.1 Sample Transfer and Encapsulation Method

The $^{NA}W^{NA}Se_2$ bilayers were synthesized by CVD method illustrated in Chapter 2. A thin layer of poly(methyl methacrylate) (PMMA, ~500 nm) was spin-coated onto the $WSe_2/SiO_2/Si$ sample at 500 rpm with a slow ramping rate of 15 rpm/s to prevent sample delamination or interlayer exfoliation and did not undergo a pre-exposure baking step. The coated substrate was then immersed into 1% HF to etch the SiO_2, followed by thoroughly rinsing the $PMMA/WSe_2$ composite in deionized H_2O. Meanwhile, another thin PMMA layer (~500 nm) was spin-coated onto a 1.00±0.01 mm-thick poly(ethylene terephthalate) (PET, Sigma Aldrich #GF74053818) substrate which served as the bottom flexible substrate used to apply strain in this experiment. The $PMMA/WSe_2$ composite was then transferred onto PMMA/PET substrate and naturally dried under an argon atmosphere to prevent WSe_2 degradation. To obtain high strain transfer from the substrate to the encapsulated sample, the $PMMA/WSe_2/PMMA/PET$ composite was annealed at 150°C for several hours until both the top and bottom PMMA layers become conformal[128]. The sample transfer and encapsulation processes are illustrated in Figure 3.1. The encapsulated bilayer and few-layer WSe_2 were still observable by an optical microscope after the annealing process as shown in Figure 3.2 c and Figure 3.3 b. We have found that lowering the PMMA annealing temperature below 150°C results in poor strain transfer from the substrate to the WSe_2, while increasing to temperatures higher than 150°C induces irreversible deformation of the $PMMA/WSe_2/PMMA/PET$ composite. After the annealing treatment, the PMMA encapsulation layer is strongly attached to the PET substrate and passed standard Scotch™ and Kapton® tape peeling tests.

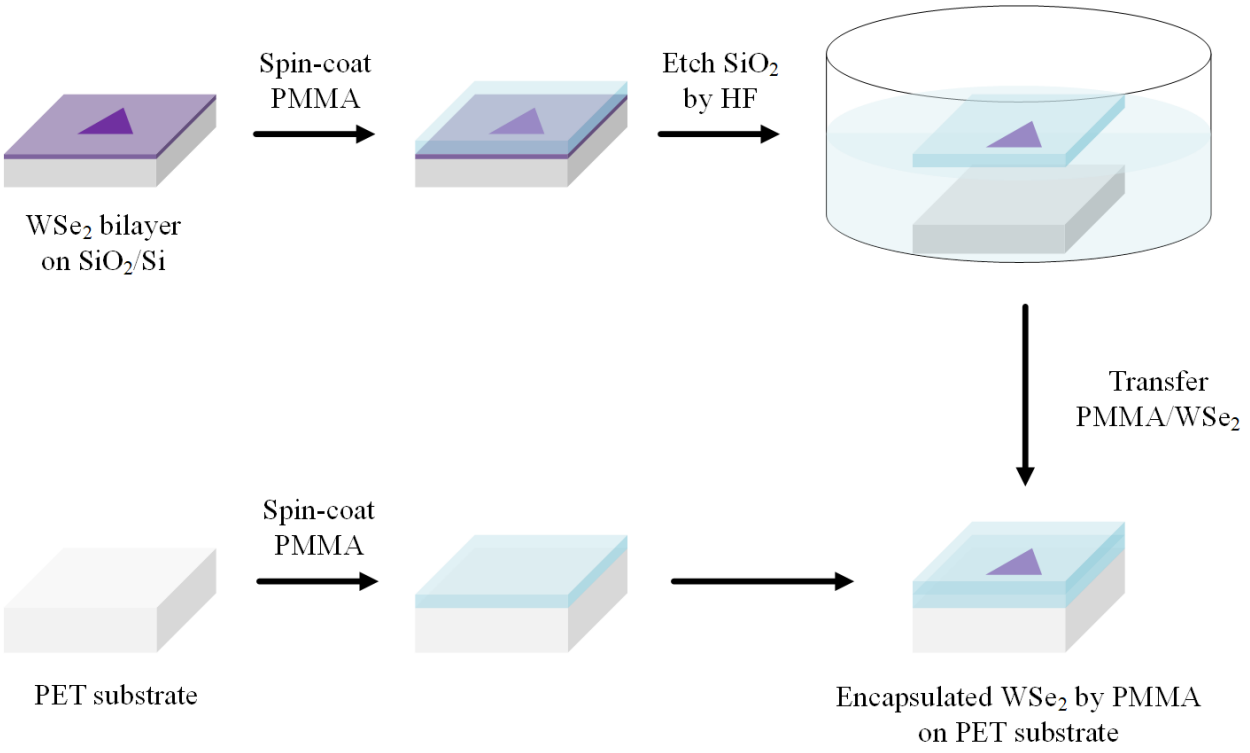

Figure 3. 1 Schematic illustration of WSe_2 encapsulation process. The thickness of each PMMA encapsulation layer is ~500 nm, and the thickness of flexible PET substrate is 1 mm.

As the PMMA/WSe_2 composite film was peeled from the SiO_2/Si substrate, AFM may not be an accurate tool to measure the thickness and layer number of WSe_2 on PMMA as the spin-coated PMMA follows the WSe_2 contour. It has been shown that the PL spectra of WSe_2 changes with different layer numbers from monolayer to bulk[126]. To demonstrate this effect in this thesis, we identified a CVD-grown WSe_2 crystal with different layer numbers and measured its thickness by AFM before transfer. We then measured the PL spectra after encapsulation in PMMA. Figure 3.2 shows the AFM of a WSe_2 crystal on SiO_2/Si substrate consists of bilayer, trilayer, sixlayer, and bulk thicknesses. Similar to what has been previously observed by ref. 126, the encapsulated sample exhibited a ~800 meV difference in the PL indirect peak energy of bilayer and trilayer WSe_2. We use this as an indicator of layer number for the encapsulated WSe_2 samples in this thesis.

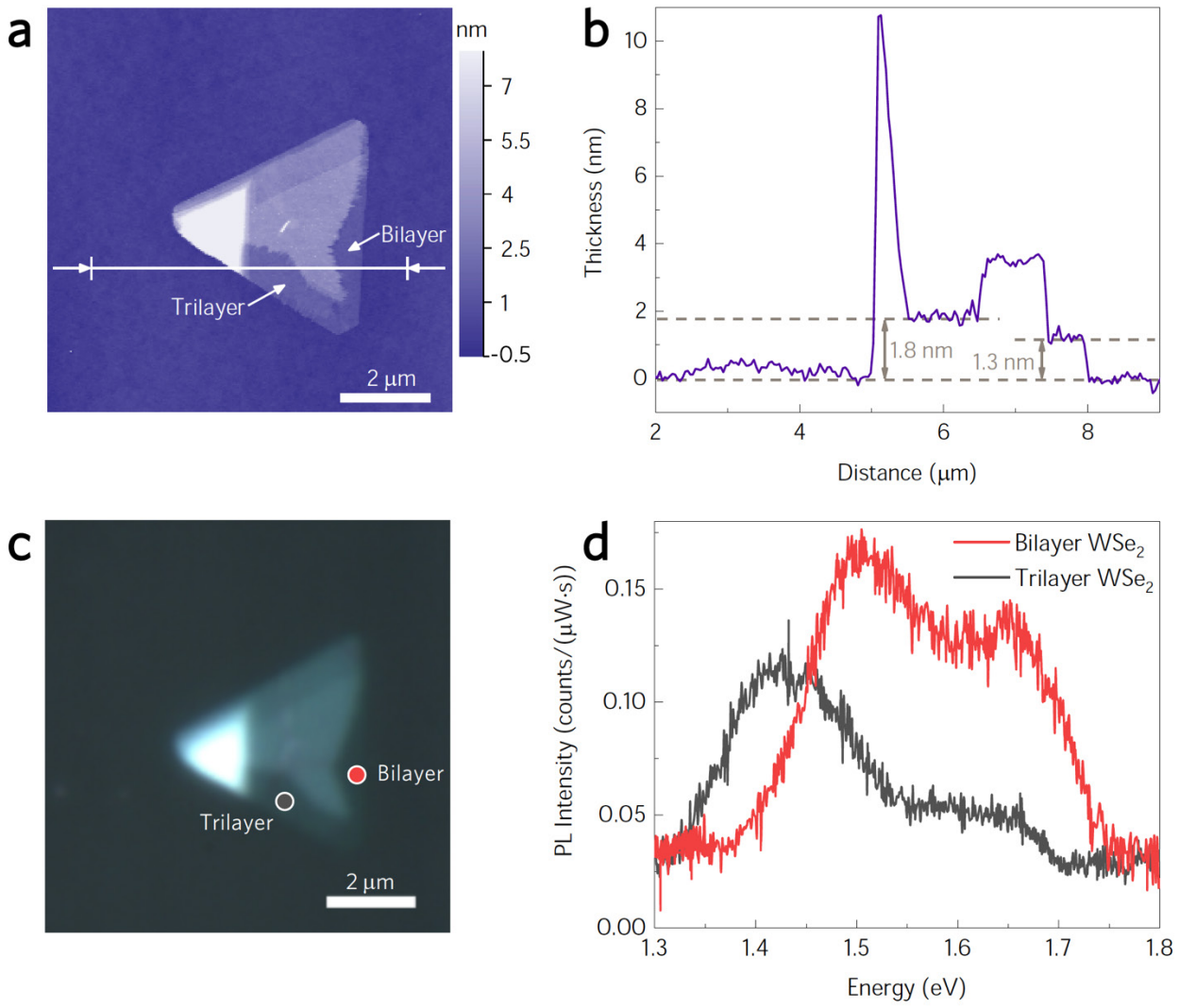

Figure 3. 2 Photoluminescence-based layer number determination of encapsulated WSe_2. (a) AFM analysis of WSe_2 crystal with bilayer, trilayer, and bulk features. (b) Cross-sectional height profiles demonstrate the thickness of bilayer (~1.3 nm) and trilayer (~1.8 nm) WSe_2. (c) Optical image of the PMMA/WSe_2/PMMA/PET composite. (d) Photoluminescence spectra of bilayer WSe_2 (red curve) and trilayer WSe_2 (black curve) taken from the corresponding regions depicted in (c).

3.2 Four-Point Bending Apparatus

A custom-designed four-point bending apparatus was used to apply tensile strain to bilayer WSe_2. The bending apparatus consists of two horizontal upper arms to apply the downward force, and two vertical lower supports whose height was adjusted using a precision vertical linear stage (Newport #M-MVN80) with 10 μm vertical graduations. Figure 3.3 shows the system with a strained PMMA/WSe_2/PMMA/PET composite. The bend radius was determined using image processing software (ImageJ 1.51k)[129], and the uniaxial strain on the WSe_2 was determined as $\varepsilon_{//} = \tau/(2r)$ where τ is the composite thickness, measured to be ~1 mm. We note that this value of strain was limited to the case of perfect strain transfer from the substrate to the encapsulated WSe_2.

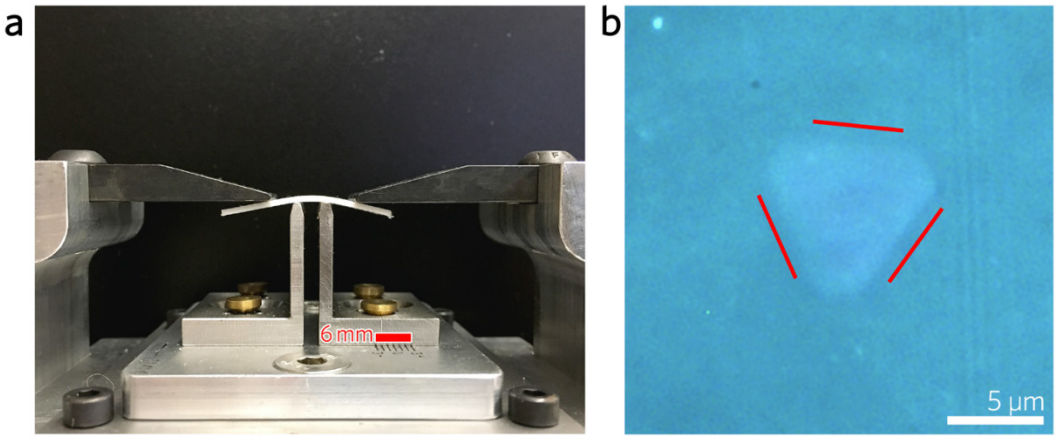

Figure 3. 3 Custom four-point bending apparatus. (a) Photograph of the four-point bending apparatus assembled onto Horiba Multiline Raman Spectrometer-LabRAM HR Evolution. (b) Photograph of the experimental apparatus applying uniaxial strain to a poly(methyl methacrylate) (PMMA)-encapsulated bilayer WSe_2 sample affixed to a flexible poly(ethylene terephthalate) (PET) substrate. Tick marks machined into the right of the device (below scale bar) indicate mm. (c) Optical microscope image of a bilayer WSe_2 crystallite encapsulated by two thin PMMA layers on a flexible PET substrate. The crystal is outlined in red as a guide to the eye.

3.3 Strain Analysis

3.3.1 Three-dimensional Poisson Effect Analysis

The Grüneisen parameter (γ) describes the effect of changes in cell volume on the phonon energies. The macroscopic Grüneisen parameter is defined as[130]

$$\gamma = V\left(\frac{\partial P}{\partial E}\right)_V = \frac{V}{C_V}\left(\frac{\partial S}{\partial V}\right)_T, \tag{3.1}$$

where P is the pressure, E is the internal energy, V is the volume of crystal, C_V is the specific heat at constant volume, S is the entropy, and T is the temperature. From the quasi-harmonic approximation, the entropy, S, can be expressed as[131]

$$S = -k_{\mathrm{B}}\sum_i\sum_{\mathbf{k}}\left\{\ln\left[1-\exp\left(-\frac{\hbar\omega_{\mathbf{k},i}}{k_{\mathrm{B}}T}\right)\right]+\frac{\hbar\omega_{\mathbf{k},i}}{k_{\mathrm{B}}T}\exp\left(\frac{\hbar\omega_{\mathbf{k},i}}{k_{\mathrm{B}}T}\right)\left[\exp\left(\frac{\hbar\omega_{\mathbf{k},i}}{k_{\mathrm{B}}T}\right)-1\right]^{-1}\right\}, \tag{3.2}$$

and its volume derivative at constant temperature can be expressed as

$$\left(\frac{\mathrm{d}S}{\mathrm{d}V}\right)_T = -k_{\mathrm{B}}\sum_i\sum_{\mathbf{k}}\frac{1}{\omega_{\mathbf{k},i}}\frac{\partial\omega_{\mathbf{k},i}}{\partial V}\frac{\left(\frac{\hbar\omega_{\mathbf{k},i}}{k_{\mathrm{B}}T}\right)^2\exp\left(\frac{\hbar\omega_{\mathbf{k},i}}{k_{\mathrm{B}}T}\right)}{\left[\exp\left(\frac{\hbar\omega_{\mathbf{k},i}}{k_{\mathrm{B}}T}\right)-1\right]^2}, \tag{3.3}$$

where k_{B} is the Boltzmann constant, $\hbar$ is the reduced Planck constant, i denotes the phonon mode index, $\mathbf{k}$ denotes the phonon wave vector, and $\omega_{\mathbf{k},i}$ is the angular frequency of phonon mode i at wavevector $\mathbf{k}$. The macroscopic Grüneisen parameter, γ, can be further expanded according to equations 3.1–3.3 as

$$\gamma = \frac{V}{C_V}\left(\frac{\partial S}{\partial V}\right)_T = -\frac{k_B}{C_V}\sum_i\sum_{\mathbf{k}}\frac{V}{\omega_{\mathbf{k},i}}\frac{\partial\omega_{\mathbf{k},i}}{\partial V}\frac{\left(\frac{\hbar\omega_{\mathbf{k},i}}{k_B T}\right)^2 \exp\left(\frac{\hbar\omega_{\mathbf{k},i}}{k_B T}\right)}{\left[\exp\left(\frac{\hbar\omega_{\mathbf{k},i}}{k_B T}\right)-1\right]^2}. \tag{3.4}$$

Based on Einstein's model[94], where all oscillators have the same energy, $\omega_{\mathbf{k},i} = \omega_{0,i}$ and the vibrational density of states was defined as $g(\omega_{0,i}) = \delta(\omega - \omega_{0,i})$. The specific heat can be expressed as

$$\begin{aligned} C_V &= \left(\frac{\partial U}{\partial T}\right)_V = \left(\frac{\partial}{\partial T}\sum_i\sum_{\mathbf{k}}\hbar\omega_{\mathbf{k},i}g\left(\omega_{\mathbf{k},i}\right)\left[\exp\left(\frac{\hbar\omega_{\mathbf{k},i}}{k_B T}\right)-1\right]^{-1}\right)_V \\ &= k_B\sum_i\left(\frac{\hbar\omega_{0,i}}{\kappa_B T}\right)^2\frac{\exp\left(\frac{\hbar\omega_{0,i}}{k_B T}\right)}{\left[\exp\left(\frac{\hbar\omega_{0,i}}{k_B T}\right)-1\right]^2} \end{aligned}. \tag{3.5}$$

Thus, in the Einstein limit of a non-propagating optical phonon with frequency $\omega_{0,i}$, the microscopic Grüneisen parameter can be expressed as

$$\gamma_i = -\frac{V}{\omega_{0,i}}\frac{\partial\omega_{0,i}}{\partial V} = -\frac{\Delta\omega_{0,i}}{\varepsilon_h\omega_{0,i}}, \tag{3.6}$$

where ε_h is the hydrostatic component of strain and $\Delta\omega_{0,i}$ is the phonon frequency change due to strain. In this thesis, the phonon polarizations of interest are the in-plane transverse optical E_{2g} mode and the out-of-plane transverse optical A_{1g} and A_{1g}^2 modes.

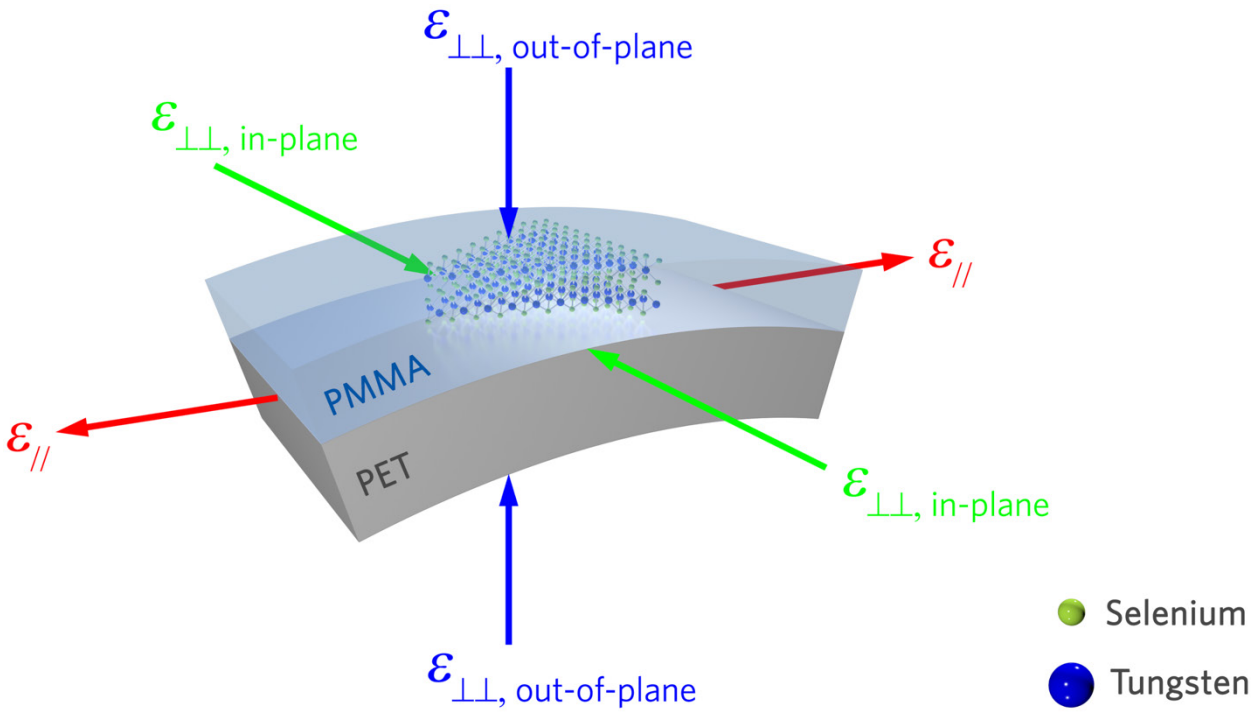

Figure 3. 4 Schematic of the Poisson effect on a uniaxially strained WSe_2 bilayer encapsulated in PMMA on top of a PET substrate: $\varepsilon_{//}$ is the uniaxial strain applied through the four-point bending apparatus, $\varepsilon_{\perp\perp,\text{ in-plane}}$ is the in-plane compressive strain caused by the Poisson effect of the PMMA/PET composite, and $\varepsilon_{\perp\perp,\text{ out-of-plane}}$ is the out-of-plane compressive strain from the Poisson effect on the PMMA encapsulation layer.

For a non-encapsulated and tensile-strained sample, an in-plane perpendicular compressive strain component ($\varepsilon_{\perp\perp,\text{ in-plane}}$) arises due to the Poisson effect of the substrate, which should be considered when estimating the Grüneisen parameter of strained atomically thin materials placed onto flexible substrates. It has been shown that the in-plane compressive strain component in the substrate can overcome the counter force from covalent bonds within graphene[46] and MoS_2[47]. For an encapsulated and tensile-strained sample, an additional out-of-plane compressive strain ($\varepsilon_{\perp\perp,\text{ out-of-plane}}$) will arise due to the Poisson effect of the encapsulation layer as illustrated in Figure 3.4.

The counterforce for this out-of-plane strain is the interlayer van der Waals bonds, which are orders of magnitude weaker in energy than the covalent bonds. Thus, for encapsulated layered materials, it is necessary to consider both the in-plane and the out-of-plane Poisson effects. In this thesis, ε_h has three components depicted in Figure 3.4: (i) $\varepsilon_{//}$, the uniaxial tensile strain applied by the bending substrate, (ii) $\varepsilon_{\perp\perp,\text{in-plane}}$, the compressive strain due to the Poisson effect of the PMMA/PET substrate in the sample plane and perpendicular to $\varepsilon_{//}$, and (iii) $\varepsilon_{\perp\perp,\text{out-of-plane}}$, the compressive strain due to the Poisson effect of the PMMA encapsulation layer perpendicular to both the sample plane and $\varepsilon_{//}$. The hydrostatic strain and Grüneisen parameter can then be expressed as

$$\varepsilon_h = \varepsilon_{//} + \varepsilon_{\perp\perp,\text{in-plane}} + \varepsilon_{\perp\perp,\text{out-of-plane}} = \varepsilon_{//}\left(1 - \nu_{\text{in-plane}} - \nu_{\text{out-of-plane}}\right) \text{ and} \tag{3.7}$$

$$\gamma_i = -\frac{\Delta\omega_{0,i}}{\varepsilon_{//}(1-\nu_{\text{in-plane}} - \nu_{\text{out-of-plane}})\omega_{0,i}}, \tag{3.8}$$

respectively, where $\nu_{\text{in-plane}}$ is the Poisson's ratio within the sample plane, and $\nu_{\text{out-of-plane}}$ is the Poisson's ratio along the direction perpendicular to sample plane. The semi-crystalline PET used here has a Poisson's ratio between 0.37–0.44 (range provided by manufacturer, Goodfellow Cambridge Ltd.). As the PET substrate is ~10^3 times thicker than the PMMA layers, we have chosen $\nu_{\text{in-plane}}$ = 0.4 for the PMMA/PET composite. Since the WSe_2 crystals are well-separated and cover only a small region of the PMMA layer, we treat the PMMA/WSe_2/PMMA composite as a PMMA block instead of a heterogeneous structure. Thus, the Poisson's ratio for the out-of-plane compressive strain, $\nu_{\text{out-of-plane}}$, was chosen as 0.33 since this value is commonly used for spin-coated PMMA[132]. The measured Raman spectra enables us to calculate the exact phonon frequency change with applied mechanical stimulus for Raman active modes. The E_{2g} Raman

active mode is an in-plane vibration. Since the E_{2g} mode decomposes into separate E^{+}_{2g} and E^{-}_{2g} peaks under uniaxial strain, we can define the frequency shifts and Grüneisen parameter of the E_{2g} mode as[46]

$$\begin{aligned}\Delta\omega^{\pm}_{0,\mathrm{E_{2g}}} &= \Delta\omega^{\mathrm{h}}_{0,\mathrm{E_{2g}}} \pm \frac{1}{2}\Delta\omega^{\mathrm{s}}_{0,\mathrm{E_{2g}}} \\ &= -\omega_{0,E_{2g}}\gamma_{\mathrm{E_{2g}}}\left(\varepsilon_{//}+\varepsilon_{\perp\perp,\text{in-plane}}+\varepsilon_{\perp\perp,\text{out-of-plane}}\right)\pm\frac{1}{2}\frac{\partial\omega^{\mathrm{s}}_{0,\mathrm{E_{2g}}}}{\partial\varepsilon_{\mathrm{s}}}\left(\varepsilon_{//}-\varepsilon_{\perp\perp,\text{in-plane}}-\varepsilon_{\perp\perp,\text{out-of-plane}}\right)\end{aligned} \quad \text{and} \quad (3.9)$$

respectively, where $\Delta\omega^{\mathrm{h}}_{0,\mathrm{E_{2g}}}$ and $\Delta\omega^{\mathrm{s}}_{0,\mathrm{E_{2g}}}$ are the phonon frequency changes corresponding to the hydrostatic component and shear component of strain, respectively. The phonon frequency of the E_{2g} mode at 0% strain is denoted as $\omega_{0,\mathrm{E_{2g}}}$. The Grüneisen parameters of the in-plane E_{2g} optical phonon mode and the out-of-plane A_{1g} and A^{2}_{1g} optical phonon modes can be now be expressed as

$$\gamma_i = -\frac{\Delta\omega^{+}_{0,i}+\Delta\omega^{-}_{0,i}}{2\varepsilon_{//}(1-\nu_{\text{in-plane}}-\nu_{\text{out-of-plane}})\omega_{0,i}},\ i=\mathrm{E_{2g}}\ \text{and} \quad (3.10)$$

$$\gamma_i = -\frac{\Delta\omega_{0,i}}{\varepsilon_{//}(1-\nu_{\text{in-plane}}-\nu_{\text{out-of-plane}})\omega_{0,i}},\ i=\mathrm{A_{1g}},\mathrm{A^{2}_{1g}}\,. \quad (3.11)$$

The above equations also apply to the non-encapsulated samples, where one can simply set the Poisson's ratio of the encapsulation layer, $\nu_{\text{out-of-plane}}$, to zero which reduces equations 3.10 and 3.11 to previously reported expressions[46,47].

3.3.2 Strain Reversibility Study

The strain reversibility verification was carried out through PL emission spectra measurements under repeated strains. The PL emission spectra and the maximum PL intensity in Figure 3.5 show that the strain effect is reversible until 1.56% strain. The PL spectra does not exhibit hysteresis in cyclic straining, indicating no slippage between two WSe_2 layers or between the WSe_2 bilayer and the PMMA. After 1.56% strain, the PET or PMMA enter the plastic regime so cyclic testing was not performed at strain values of 1.93% or above, but we did not observe creep or relaxation as evidenced by our Raman spectra at high strains.

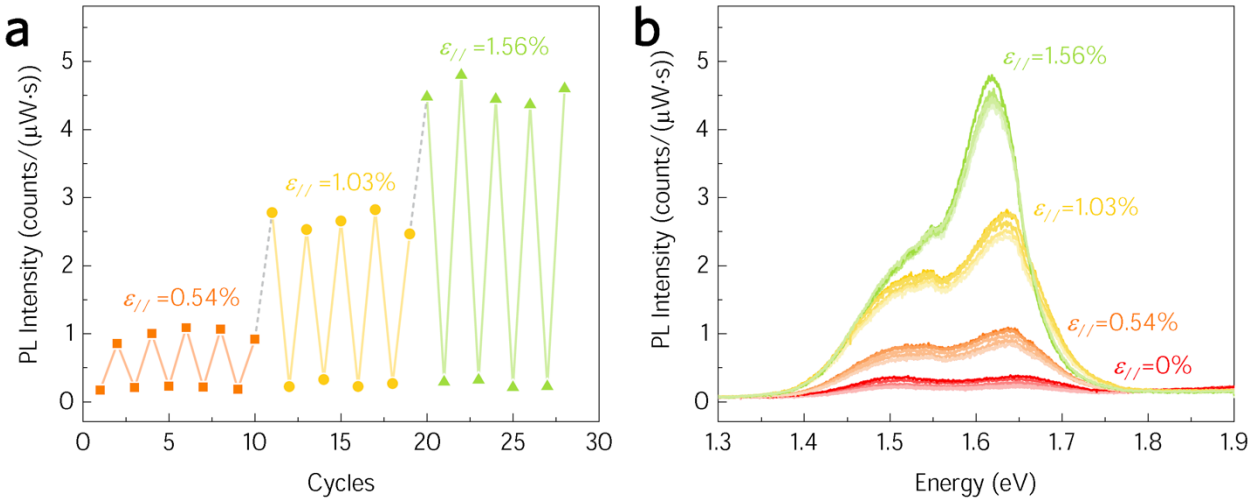

Figure 3. 5 Reproducibility of strain-controlled photoluminescence (PL) emission spectra. (a) Cyclic stability of the maximum PL intensities of bilayer WSe_2 at uniaxial strain, $\varepsilon_{//}$, demonstrating elastic and reversible strain up to 1.56%. (b) Corresponding PL spectra of cyclically strained bilayer WSe_2.

3.3.3 Strain Transfer Verification

It is critical to verify the amount of strain transferred from the flexible substrate to the WSe_2 sample. In this thesis, we have verified the strain transfer by measuring the Grüneisen parameter of monolayer graphene from the strain-dependent Raman spectra. The graphene was grown on copper foil (Alfa Aesar #13382) by thermal catalytic decomposition of methane, similar to ref. 133. This was performed by Dr. Robert A. Burke of the U. S. Army Research Laboratory in Adelphi, Maryland. The coating on the Cu foil was first removed with dilute nitric acid, where the pretreatment etching time was limited to prevent roughening of the Cu surface while removing the protective coating similar to what has been reported by ref. 134. After pretreatment, the foil was loaded into a low-pressure CVD reactor system and the growth was carried out at 1000°C for 30 minutes at ~0.333 mbar using 100 cm^3min^{-1} of H_2 and 1 cm^3min^{-1} of CH_4. We note that we have observed small areas of discontinuity in the graphene film for growth times of 20 minutes or less. For a 30-minute growth, we obtained full coverage while preventing the emergence of a disorder peak.

In contrast with a previous report[46], where only the bottom side of the exfoliated graphene was in contact with a SU-8/PET substrate, we encapsulated our graphene using PMMA to act as a control experiment to compare with WSe_2 bilayer. The graphene film was milled into triangular shapes with 12 μm edge lengths to simulate the domain size for our bilayer WSe_2 crystal. As this involved the use of focused ion beam patterning with Ga^+ ions (FEI Helios NanoLab 460F1). The ion beam current was set at 7 pA to avoid serious sample damage. As shown in Figure 3.6, the 2D peak: G peak Raman intensity ratio was 2:1 both before and after milling which indicates that the single layer structure remained intact[135]. The D peak appears for patterned graphene due the scattering of Ga^+ ions which creates defects away from the area directly exposed to the ion beam.

The PMMA/graphene film was removed from the Cu substrate using 0.1 M ammonium persulfate at room temperature. The Raman spectra was measured by a Horiba Multiline Raman Spectrometer-LabRAM HR Evolution. Since we were unable to resolve the G mode from the signal arising from the PMMA/PET substrate, we evaluated the Grüneisen parameter of dispersive in-plane transverse optical (iTO) phonons using the 2D mode of the sample and the three-dimensional Poisson effect model as described above (equation 3.11).

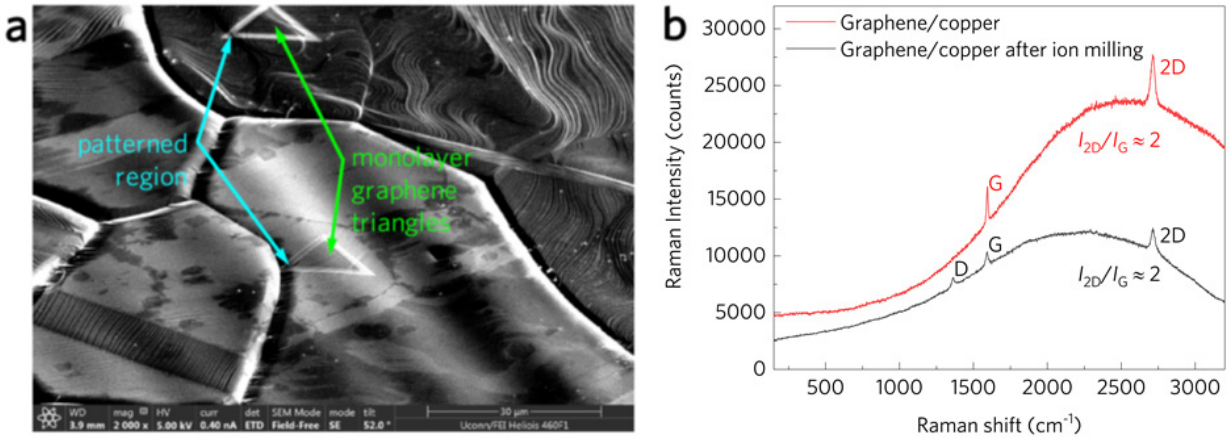

Figure 3. 6 Patterned graphene used in strain verification experiment. (a) Scanning electron microscopy image of a continuous monolayer graphene film patterned into triangular domains with edge lengths of ~12 μm. (b) Raman spectra of graphene before and after patterning. Although the defect-enabled D peak appears for graphene patterned by Ga^+ focused ion beam milling, the 2D-to-G peak intensity ratio remains ~2 as expected for monolayer graphene.

Figure 3.7 shows the evolution of the 2D peak with uniaxial strain. The linear strain dependence up to 2.49% strain indicates that the strain relaxation by slippage or plastic deformation is not observable. The difference in the slopes of the strain-dependent Raman shift between this thesis ($\delta\omega/\delta\varepsilon_{//} = -26.6\pm1.68$ cm^{-1}/% strain) and ref. 46 ($\delta\omega/\delta\varepsilon_{//} = -64.5\pm4.8$ cm^{-1}/% strain) arises from the fact that our encapsulated graphene experiences an out-of-plane

compressive stress due to the 3D Poisson effect of the substrate, while the graphene in ref. 46 was unencapsulated. The uncertainty in $\delta\omega/\delta\varepsilon_{//}$ was given as the upper and lower 95% confidence bounds of the linear regression model used to fit the data. For our encapsulated graphene, we have obtained a value of $\gamma_{2D} = 3.66$ with a standard deviation of 0.23 (Figure 3.7). The value we obtained for graphene is consistent with the value for the iTO modes we calculated by analyzing the 2D strain-dependent frequency shift reported in a similar study on graphene[46], $\gamma_{2D} = 3.583 \pm 0.267$, where we have defined the uncertainty from the upper and lower 95% confidence bounds. In our analysis of ref. 46, we did not consider the out-of-plane Poisson effect as the sample was not encapsulated, and the Grüneisen parameters were calculated as

$$\gamma_{2D,\text{non-encapsulated}} = -\frac{\Delta\omega_{0,2D}}{\varepsilon_{//}(1-\nu_{\text{in-plane}})\omega_{0,2D}}. \tag{3.12}$$

We have chosen a Poisson's ratio of 0.33 for the SU8-coated PET and Perspex substrates used in that report[46]. The small deviation of Grüneisen parameters between ref. 46 and this thesis likely arises from the uncertainty of the estimated Poisson's ratios of the different flexible substrates. For example, PET has a manufacturer-provided range of 0.37–0.44 for semi-crystalline PET, and PMMA has a range from 0.3–0.4. Additionally, we note the appropriateness of our 3D model as follows: if we were to adopt a two-dimensional Poisson effect model for our encapsulated samples as described by equation 3.12, the Grüneisen parameter of our graphene would be underestimated by roughly a factor of two.

Beside the study on patterned graphene, we also carried out the Raman measurement on unpatterned and isolated graphene with domain size as tens of μm. Figure 3.8 shows the strain dependent Raman spectra of unpatterned graphene. We have chosen the exact same analysis and

Grüneisen parameter calculation model as it for patterned graphene. Both patterned and unpatterned graphene exhibit similar 2D mode phonon frequency changes with strain as 26.6±1.7 cm^{-1}/% and 29.6±1.6 cm^{-1}/%. The Grüneisen parameter is calculated as 3.894±0.214. The slight larger Grüneisen parameter comparing with it of patterned graphene may contribute by uncertainty of strain value estimation or other aspects, but still in agreement with previous reported Grüneisen parameter as 3.58[46]. The maximum applied strain is 1.6% which is ~23% higher than previous reported using four-point bending method with uncapsulated graphene[46].

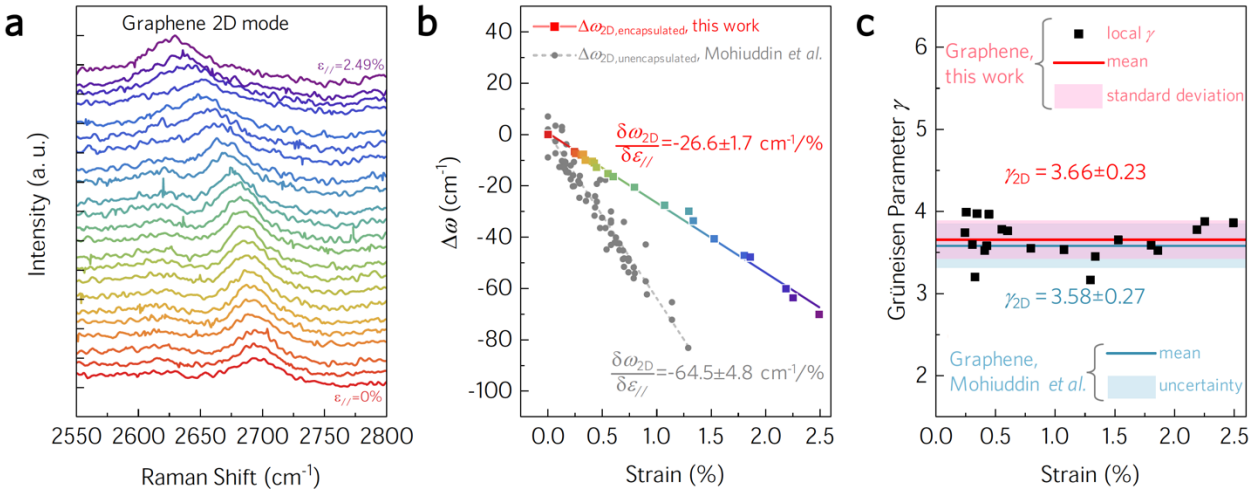

Figure. 3. 7 Measured Raman spectra and Grüneisen parameter of the 2D mode of CVD-grown encapsulated graphene patterned into triangles. (a) Raman spectra as a function of applied uniaxial strain. (b) Strain dependence of the 2D peak Raman shift, obtained by deconvolution of the experimental spectra using Lorentzian distributions. Also shown is the strain dependence of the 2D mode of unencapsulated graphene reproduced from ref. 46. Uncertainties in $\partial\omega/\partial\varepsilon_{//}$ are given as the upper and lower 95% confidence bounds of a linear regression model for both data sets. The linear train dependence of the Raman shift indicates no observable strain relaxation. (c) The Grüneisen parameter for the 2D mode is obtained from the strain-dependent Raman spectra as 3.66

with a standard deviation of 0.23. This is in agreement with the 2D mode value of 3.583±0.267 calculated from ref. 46, where uncertainty is defined using the upper and lower 95% confidence bounds.

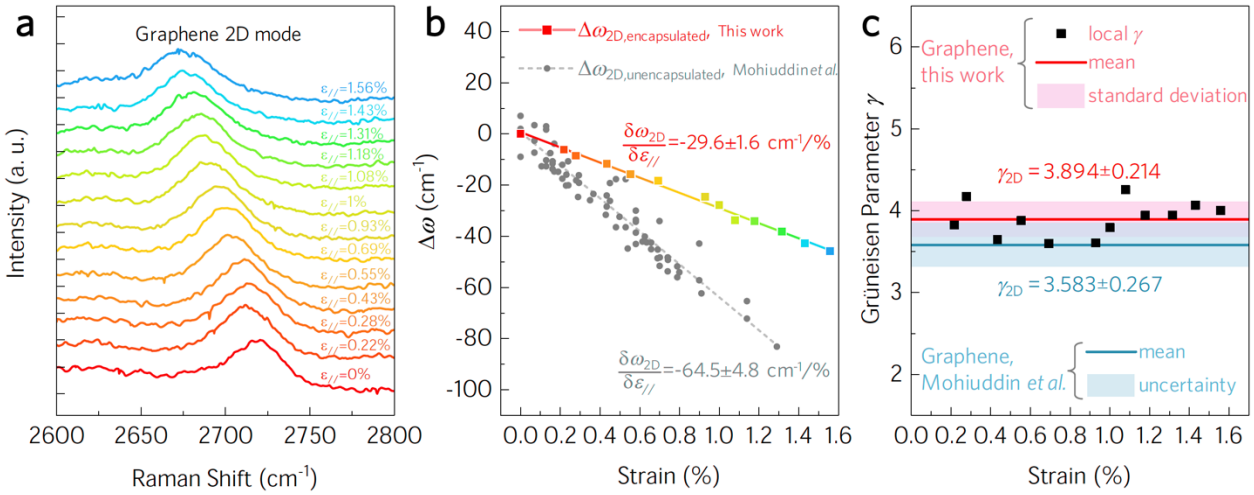

Figure 3. 8 Measured Raman spectra and Grüneisen parameter of the 2D mode of CVD-grown encapsulated unpatterned graphene. (a) Raman spectra as a function of applied uniaxial strain. (b) Strain dependence of the 2D peak Raman shift, obtained by deconvolution of the experimental spectra using Lorentzian distributions. Also shown is the strain dependence of the 2D mode of unencapsulated graphene reproduced from ref. 46. Uncertainties in $\partial\omega/\partial\varepsilon_{//}$ are given as the upper and lower 95% confidence bounds of a linear regression model for both data sets. The linear train dependence of the Raman shift indicates no observable strain relaxation. (c) The Grüneisen parameter for the 2D mode is obtained from the strain-dependent Raman spectra as 3.894 with a standard deviation of 0.214. This is in agreement with the 2D mode value of 3.583±0.267 calculated from ref. 46, where uncertainty is defined using the upper and lower 95% confidence bounds.

3.4 Strain Dependent Phonon Dispersion

Strain-dependence of the phonon energies in bilayer WSe_2 yield information on atomic displacement and fundamental thermodynamic properties. Figure 3.9 shows the evolution of optical phonon energies with strain as obtained by Raman spectroscopy. The unstrained sample shows three major Raman active modes: (i) the in-plane transverse optical E_{2g} mode at 250.1 cm^{-1}, (ii) the out-of-plane transverse A_{1g} mode at 259.5 cm^{-1}, and (iii) the out-of-plane transverse A_{1g}^2 mode at 310.7 cm^{-1}. The E_{2g} and A_{1g} peak energies are comparable to those reported for unstrained CVD-grown[117] and mechanically exfoliated WSe_2 thin layers[136], while the A_{1g}^2 mode only appears for multilayer WSe_2[112,117]. As increasing the uniaxial tensile strain breaks the crystal symmetry, the doubly degenerate E_{2g} mode evolves into two discrete modes, E_{2g}^+ and E_{2g}^-, corresponding to the in-plane atomic vibrations perpendicular and parallel to the applied strain direction, respectively. Both the E_{2g}^+ and E_{2g}^- modes exhibit a consistent shift with strain (Figure 3.9b), indicating a lack of Raman-observable slippage between the WSe_2/PMMA, PMMA/PET, and WSe_2/WSe_2 interfaces over a large range of strain (0%-3.59%). The redshift of the E_{2g}^- mode arises from phonon softening in the presence of tensile strain ($\varepsilon_{//}$), while the blueshift of the E_{2g}^+ mode indicates stiffening due to perpendicular compressive strain ($\varepsilon_{\perp\perp}$) resulting from the Poisson effect of the substrate. In contrast with previous un-encapsulated cases that only consider the in-plane two-dimensional Poisson effect[46], we have evaluated the Grüneisen parameter of our encapsulated bilayer WSe_2 with a three-dimensional Poisson effect model developed to incorporate the compressive strain in the out-of-plane direction arising from the strained encapsulation layer. Using this three-dimensional Poisson effect model, the phonon polarization specific Grüneisen parameters are evaluated as

$$\gamma_i = \begin{cases} -\dfrac{\Delta\omega_{0,i}^{+} + \Delta\omega_{0,i}^{-}}{2\varepsilon_{//}(1-\nu_{\text{in-plane}}-\nu_{\text{out-of-plane}})\omega_{0,i}}, & i = \mathrm{E_{2g}} \\ -\dfrac{\Delta\omega_{0,i}}{\varepsilon_{//}(1-\nu_{\text{in-plane}}-\nu_{\text{out-of-plane}})\omega_{0,i}}, & i = \mathrm{A_{1g}}, \mathrm{A_{1g}^2} \end{cases}, \tag{3.13}$$

where $\omega_{0,i}$ is the frequency of the unstrained phonon mode i, $\Delta\omega_{0,i}$ is the change in frequency of the phonon mode i with uniaxial strain, $\nu_{\text{in-plane}}$ is the Poisson's ratio of the PMMA/PET composite, and $\nu_{\text{out-of-plane}}$ is the Poisson's ratio of the PMMA. Over the range of 0–3.59% strain, the Grüneisen parameter (γ) of the E_{2g} mode is measured as 1.149 with a standard deviation of 0.027, γ of the A_{1g} mode is 0.307 with a standard deviation of 0.061, and γ of the A_{1g}^2 mode is 0.357 with a standard deviation of 0.103, which are comparable with MoS_2[47]. We justify the importance of our 3D model for encapsulated atomically thin materials as follows. If we applied a two-dimensional Poisson effect model to our experimental data, the Grüneisen parameter of our samples would be calculated as 0.517±0.012, 0.138±0.027 and 0.161±0.046 for the E_{2g}, A_{1g} and A^2_{1g} modes respectively. Thus, by neglecting the out-of-plane Poisson effect in encapsulated samples, the Grüneisen parameter would be underestimated by a factor of 2.2, which was of importance as it governed the anisotropic intrinsic phonon scattering processes in these materials[137-140].

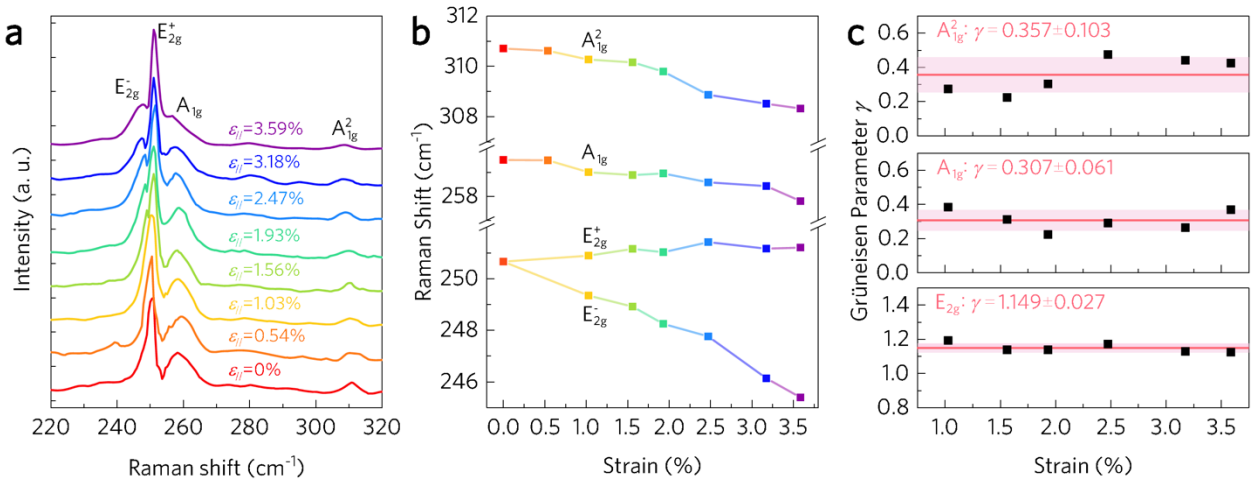

Figure 3. 9 Raman spectra of bilayer WSe_2 as it is strained up to 3.59%. (a) Raman spectra as a function of uniaxial strain ($\varepsilon_{//}$). As strain increases, the in-plane E_{2g} optical phonon mode evolves into separate E^{+}_{2g} and E^{-}_{2g} modes. (b) Strain dependence of the peak Raman shifts for the E^{+}_{2g}, E^{-}_{2g}, A_{1g}, and A^{2}_{1g} modes, obtained by deconvolution of the experimental Raman spectra using Lorentzian distributions. The linear strain dependence of the Raman shift indicates strain relaxation by slippage or plastic deformation is not observed. (c) Mode-specific Grüneisen parameters of bilayer WSe_2 are constant over the range of $0.01 \leq \varepsilon_{//} \leq 0.036$.

3.5 Strain Dependent Photoluminescence and Optical Band Gap Evolution

The PL emission spectra of WSe_2 bilayer were obtained using a 2.33 eV ($\lambda = 532$ nm) continuous wave excitation at low power (86 μW) to avoid sample damage and spectral shifts due to local heating effects[47]. Figure 3.10 and 3.11 shows the PL emission response to uniaxial tensile strain. The PL emission spectra was deconvolved for each strain value using Gaussian distributions as shown in Figure 3.10. We note that the coefficient of determination (R^2) is 0.983 for the unstrained sample due to the low PL signal-to-noise ratio, and higher than 0.997 for all strained

cases. The PL spectra were deconvolved by two Gaussian peaks which differ in energy by ~138 meV for the unstrained bilayer WSe_2 and by ~8 meV for a strain of 3.59 % (Figure 3.10).

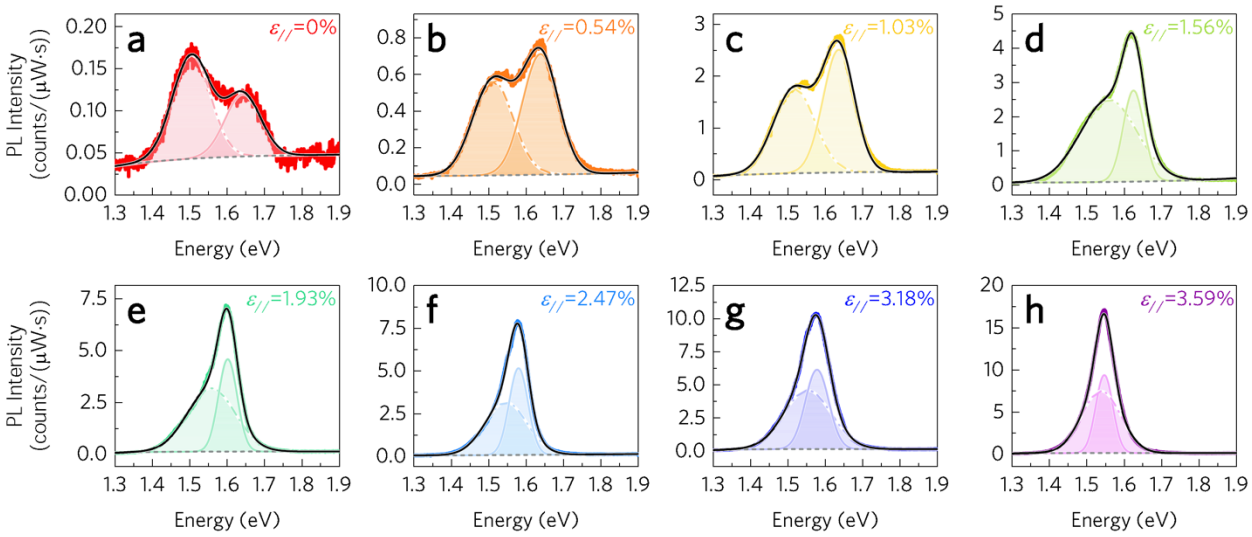

Figure 3. 10 Photoluminescence spectra of bilayer WSe_2 with increasing uniaxial strain. PL intensity versus emission energy is shown for $\varepsilon_{//}$ = (a) 0, (b) 0.54, (c) 1.03, (d) 1.56, (e) 1.93, (f) 2.47, (g) 3.18, and (h) 3.59% under continuous wave excitation at an energy of 2.33 eV (λ = 532 nm). The indirect (dash-dotted lines) and direct (solid lines) optical transition peaks were deconvolved using Gaussian distributions, and the background is shown as a gray dashed line.

To elucidate the mechanisms driving the measured strain-coupled optoelectronic effects, our collaborators Dr. Jin Wang and Prof. Avinash Dongare at the University of Connecticut Department of Materials Science and Engineering have developed a full theoretical analysis of the electronic dispersion evolution with strain using density functional theory (DFT), the main results of which are shown in Figure 3.11. Spin orbital coupling (SOC), van der Waals interaction (vdW) of WSe_2 layers, and the Poisson effect of the substrate are all taken into account for the electronic

band structure calculation. As Figure 3.11 b depicts, the experimental strain-dependent indirect and direct emission peaks matched well with their theoretical prediction, with only a slight difference arising from the assumption of strain-independent binding energy and the estimation of the substrate's Poisson ratio. We also compared our experimental results with a previous DFT prediction using the Heyd-Scuseria-Ernzerhof (HSE) hybrid functional which did not consider vdW interactions or the Poisson effect[50] (Figure 3.11 b). The HSE-DFT result predicted an indirect-to-direct transition crossover at a small strain of ~0.5%, which differs from our experimental and theoretical results by an order of magnitude. This large deviation indicates the importance of the vdW interaction for layered TMDs such as bilayer WSe_2 and the Poisson effect of the substrate in achieving physically reproducible theoretical predictions for strain-coupled transport phenomena. We note that it is reasonable to neglect the vdW interaction for un-encapsulated monolayer TMDs, however, this component is critical for multilayer TMDs.

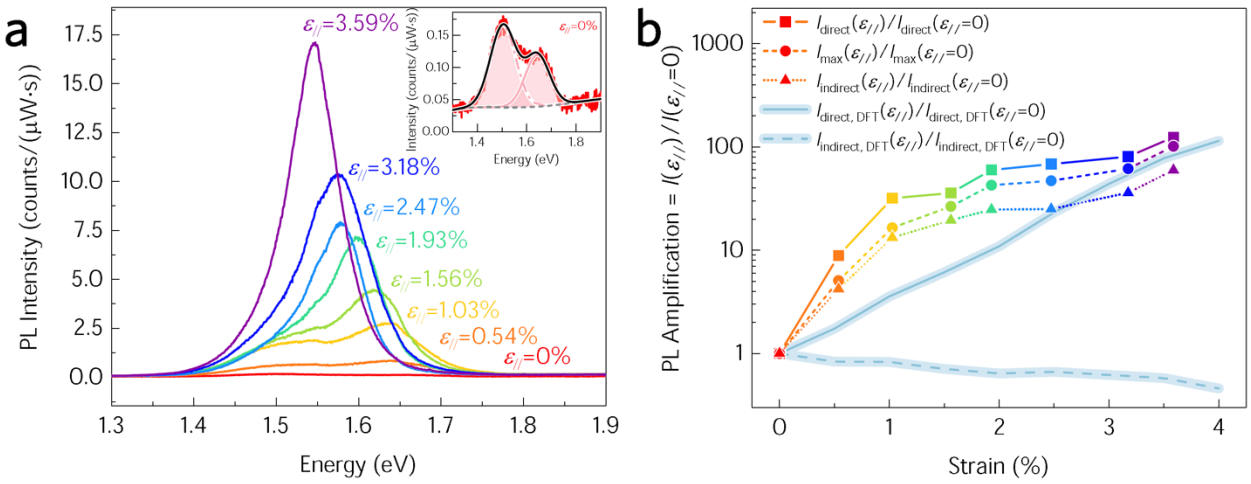

Figure 3. 11 Amplification of the photoluminescence (PL) emission intensity of WSe_2 bilayer when strained up to 3.59%. (a) PL emission spectra resulting from excitation at 2.33 eV as a function of applied uniaxial strain. Inset shows the PL spectra of the unstrained material, $\varepsilon_{//}=0$, where the indirect (dash-dotted line) and direct (solid line) electronic transitions have been deconvolved using Gaussian distributions. (b) Experimental PL amplification versus strain, defined as $I(\varepsilon_{//}) / I(\varepsilon_{//}=0)$. Subscripts max, direct, and indirect denote amplification obtained using the max intensity of the experimental PL, the max intensity of the deconvolved direct sub-peak, and the max intensity of the deconvolved indirect sub-peak, respectively. All computational results were conducted by Dr. Jin Wang and Prof. Avinash Dongare, University of Connecticut Materials Science and Engineering, and obtained by density functional theory (DFT) including the effect of spin orbit coupling, van der Waals interactions, and Poisson effect from PMMA/PET are shown for the direct (solid light blue line) and indirect (dashed light blue line) electronic transitions.

To assign the two PL sub peaks to electronic transitions, we first compared the PL peak energy difference to the spin-orbit valence band splitting energy at the K-point in the Brillouin zone, which is ~0.5 eV from 0 to 2% uniaxial tensile strain[123]. The valance band splitting energy is at least four times larger than our measured PL peak energy difference, and its dependence on strain is much less than we measured here. Secondly, neither of the two PL peaks are expected to result from trion emission since the charged exciton energy was only ~30 meV lower than the exciton energy for unstrained bilayer WSe_2[141], which is ~4.6 times lower than we have measured. Thirdly, these two PL peaks do not belong to biexcitonic recombination since its observability should significantly diminish above 70 K[142]. We can also conclude that these two peaks do not stem from slippage between the top and bottom WSe_2 layers at high strain. As slippage will increase with strain, the difference between these two peaks would revert to a larger energy closer to that of the unstrained material, which is contradictory with our experimental observation of continuously decreasing separation with strain. As shown in the inset of Figure 3.10a, the unstrained PL peak at 1.50 eV has a full width at half maximum (FWHM) of 121.03 meV, which is similar to the reported FWHM of the indirect band transition of unstrained bilayer WSe_2[136]. Additionally, the strain-dependent blue (red) shift of the lower (higher) energy PL sub peak also matches the indirect (direct) electronic band gap strain dependence calculated by our *ab initio* model which includes spin-orbit coupling, interlayer van der Waals bonding, and the Poisson effect from the PMMA encapsulation layer (Figure 3.11). Thus, we assign the lower energy PL sub peak to the indirect electron transition between the conduction band minimum at the Σ-point (CBM_Σ) and the valence band maximum at the K-point (VBM_K), and the higher energy sub peak to the direct electronic transition at the K-point (CBM_K–VBM_K). The PL indirect band gap linearly increased with strain at a rate of 11.14 meV/% to 1.54 eV (FWHM = 123.08 meV) at 3.59%

uniaxial tensile strain. The PL direct band gap decreased with strain at a rate of 27.9 meV/% from 1.64 eV (FWHM = 117.2 meV) in the unstrained material to 1.54 eV (FWHM = 53.6 meV) at 3.59 % uniaxial tensile strain. The FWHM of the direct transition peak is similar to that reported for mechanically exfoliated monolayer WSe_2 (FWHM = 56 meV)[136]. Our theoretical model predicts that the PL indirect-to-direct crossover will occur at 4.28 %, however, the ability to reach this value experimentally is limited by the fatigue of the PMMA/PET substrate.

Since the bilayer WSe_2 is by definition an indirect semiconductor under uniaxial strain up to 3.59%, we report optical strain-coupled behavior for direct and indirect transitions separately int this thesis. Figure 3.11b shows the PL intensity corresponding to the direct excitonic transition (colored squares) is enhanced by 124.3 times at 3.59% strain. The enhancement of the overall maximum PL intensity (colored triangles) is 101.4 times at 3.59% strain. Even at 1.93% uniaxial strain, the maximum PL intensity enhancement is ~42.6 times, which is 42% larger than previously reported at 2% strain[50] due to the high amount of strain transferred to the TMD sample in this thesis as verified experimentally using thin graphite. The maximum PL intensity enhancement is smaller than the enhancement of the direct transition since the indirect transition has a higher PL intensity than the direct transition for the unstrained sample. As the strain increases to values higher than ~0.5%, the direct transition begins to dominate the PL response as shown in Figure 3.10.

To elucidate the mechanisms responsible for the large enhancement observed here and to understand the maximum achievable amplification, we have used our DFT-vdW-Poisson theoretical model to calculate the enhancements of the direct and indirect excitonic transitions. To estimate the PL intensity enhancement of the direct transition, we use a similar approach as reported in ref. 50 and define the radiative efficiency η for the direct transition as[143]

$$\eta = \frac{Anp}{Anp + Bnp^2 + Cn}, \tag{3.14}$$

where n is the electron concentration, p is the hole concentration, Anp represents radiative recombination, Bnp^2 represents Auger recombination, and Cn represents Shockley-Read-Hall recombination. The PL intensity of the direct electronic transition can be estimated as

$$I_{\text{direct}} \propto \eta \cdot \left(\frac{n_{\text{direct}}}{n_{\text{direct}} + n_{\text{indirect}}} \right) \cdot \left(n_{\text{direct}} + n_{\text{indirect}} \right), \tag{3.15}$$

where n_{direct} and n_{indirect} are the electron concentrations at the direct and indirect conduction band minima, $\text{CBM}_{\text{direct}}$ and $\text{CBM}_{\text{indirect}}$, respectively. To estimate the PL intensity amplification, we simplify the above equation by assuming the radiative efficiency, η, remains constant with strain. The PL intensity enhancement can be expressed as

$$\frac{I_{\text{direct}}\left(\varepsilon_{//}\right)}{I_{\text{direct}}\left(\varepsilon_{//}=0\right)} = \frac{n_{\text{direct}}\left(\varepsilon_{//}\right)}{n_{\text{direct}}\left(\varepsilon_{//}=0\right)}. \tag{3.16}$$

Using the Boltzmann approximation, we approximate n_{direct} using the strain-dependent direct electronic band gap obtained by our DFT-vdW calculations, ΔE_{direct}, as

$$\frac{I_{\text{direct}}\left(\varepsilon_{//}\right)}{I_{\text{direct}}\left(\varepsilon_{//}=0\right)} = \frac{e^{-\frac{\Delta E_{\text{direct}}\left(\varepsilon_{//}\right)}{k_{\text{B}}T}}}{e^{-\frac{\Delta E_{\text{direct}}\left(\varepsilon_{//}=0\right)}{k_{\text{B}}T}}}. \tag{3.17}$$

A similar treatment can be used to predict attenuation of the indirect transitions as

$$\frac{I_{\text{indirect}}\left(\varepsilon_{//}\right)}{I_{\text{indirect}}\left(\varepsilon_{//}=0\right)} = \frac{e^{-\frac{\Delta E_{\text{indirect}}\left(\varepsilon_{//}\right)}{k_{\text{B}}T}}}{e^{-\frac{\Delta E_{\text{indirect}}\left(\varepsilon_{//}=0\right)}{k_{\text{B}}T}}}. \tag{3.18}$$

where $\Delta E_j(\varepsilon_{//})$ and $\Delta E_j(\varepsilon_{//}=0)$ are the band transition energies of the strained and unstrained bilayer WSe_2. The PL intensity enhancement for the experimental direct transition (colored squares in Figure 3.12b) and theoretical prediction results (light blue solid line in Figure 3.12b) were consistent. The experimental PL enhancement was 124.3 times and the calculated result was 81.35 times at 3.59% strain. The deviation at lower strain may arise from simplifying assumptions for Equation 1 and the assumption of a strain-independent binding energy in the DFT-vdW-Poisson model.

As can be seen in Figure 3.12b for the indirect transition, a large disagreement in both trend and magnitude between the experimental (colored triangles) and calculated (light blue solid line) amplification of the indirect transition likely arises due to enhanced scattering between K and Σ valleys in the conduction band, which become closer in energy with strain as will be discussed. This mechanism is also likely responsible for reducing the overall experimentally observed PL amplification in comparison with calculated amplification of the direct transition for strains above 2%. The experimental PL intensity of the indirect transition f amplified by ~59.7 times at 3.59% strain, which was contrary to both our experimental observation and theoretical prediction of an increase in indirect band gap energy with tensile strain. Applying Equation 1 to the indirect transition, the PL intensity is expected to attenuate with tensile strain to a value of $I_{indirect}/I_{indirect}(\varepsilon_{//}=0) = 0.52$ at 3.59% strain. This can be explained by an increase in the phonon-assisted electron scattering from the conduction band minimum at the K-point (CBM_{direct}) to the conduction band minimum at the Σ-point ($CBM_{indirect}$) as illustrated in Figure 3.12a. The PL intensity of the indirect transition is the result of competition between: (i) an increase in the indirect band gap with strain which weakens the radiative recombination rate and (ii) phonon-assisted CBM_{direct}-to-$CBM_{indirect}$ electron scattering which enhances the indirect recombination rate. The

phonon-assisted CBM_{direct}-to-$CBM_{indirect}$ intervalley transition rate is proportional to the direct transition rate which increases with strain. Thus, the indirect transition PL intensity is enhanced with strain. Meanwhile, increasing the indirect band gap with strain counteracts the PL intensity enhancement due to the phonon-assisted CBM_{direct}-to-$CBM_{indirect}$ intervalley transitions. The energy difference between CBM_{direct} and $CBM_{indirect}$ drives this intraband electron transition and can be evaluated as

$$\Delta E_{\mathrm{CBM_{direct}-CBM_{indirect}}} = \Delta E_{\mathrm{direct-indirect}} = E_{\mathrm{direct}} - E_{\mathrm{indirect}}\,. \tag{3.19}$$

Our theoretical results shown in Figure 3.12b indicate that $\Delta E_{\text{indirect-direct}}$ decreases with increased strain at a rate of 35.7 meV/%, from 155 meV at $\varepsilon_{//}$=0% to 12.2 meV at $\varepsilon_{//}$=4%. Thus, the phonon-assisted CBM_{direct}-to-$CBM_{indirect}$ transition rate is expected to increase with tensile strain by 250.6 times at 4% uniaxial tensile strain according to

$$\frac{I_{\mathrm{intraband}}\left(\varepsilon_{//}\right)}{I_{\mathrm{intraband}}\left(\varepsilon_{//}=0\right)} = \frac{e^{-\frac{\Delta E_{\mathrm{CBM_{direct}-CMB_{indirect}}}\left(\varepsilon_{//}\right)}{k_{\mathrm{B}}T}}}{e^{-\frac{\Delta E_{\mathrm{CBM_{direct}-CMB_{indirect}}}\left(\varepsilon_{//}=0\right)}{k_{\mathrm{B}}T}}}\,. \tag{3.20}$$

The consequences of increased intraband scattering can be observed in Figure 3.12b, where the maximum PL enhancement becomes closer to the direct transition enhancement at high strain while entering into an apparent saturation regime as the valley minima near degeneracy. Additionally, the high amplification of the indirect transition intensity with strain (as opposed to the theoretically predicted attenuation) results from the greatly increased intraband scattering processes as $\Delta E_{\text{indirect-direct}}$ decreases towards degeneracy.

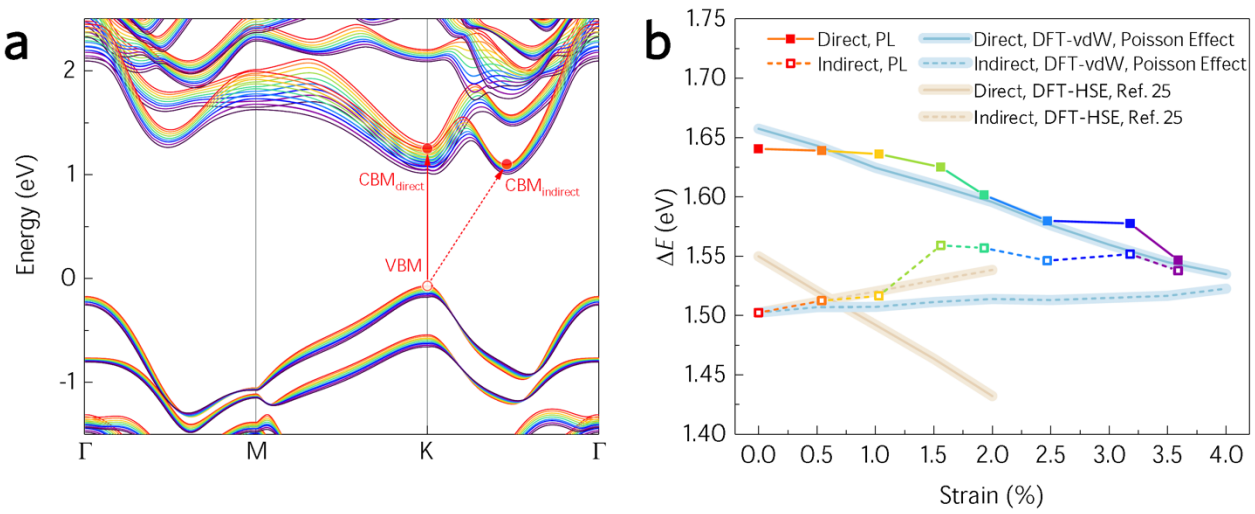

Figure 3. 12 Indirect-to-direct electronic band transition conversion through strain. (a) Evolution of the electronic band structure in response to uniaxial strain calculated using density functional theory including both spin orbit coupling, interlayer van der Waals interactions, and the Poisson effect (DFT-vdW-Poisson) for $\varepsilon_{//}$ = 0% (red) to 4% (purple) in increments of 0.5%. Direct and indirect electronic transitions are depicted. (b) Strain-dependence of the interband transition energies normalized to that of the unstrained indirect PL transition. Experimental values have been obtained by deconvolution of the PL emission spectra using Gaussian distributions and are shown in comparison with a DFT-vdW-Poisson model (blue lines, DFT calculations by Dr. Jin Wang and Prof. Avinash Dongare, University of Connecticut Materials Science and Engineering) and a calculation neglecting van der Waals interactions (DFT-HSE, obtained from ref. 50). The indirect-to-direct conversion occurs at $\varepsilon_{//} > 3.5\%$ in both the experiment and DFT-vdW-Poisson calculation and at ~0.5% when vdW interactions are neglected (DFT-HSE[50]), indicating that increased interlayer coupling strength may lead to weaker strain-coupled effects in layered materials.

3.6 Strain Transfer Analysis of Unencapsulated WSe_2 Bilayer Single Crystals

Straining unencapsulated atomically thin materials has been widely used in previous reports[46,47,50,111,144,145]. Due to non-ideal contact for bottom and top side, the unencapsulation method may have strain transfer issues, such as yield and strain transfer efficiency. We are using our strain transfer method to analyze previously reported strained WSe_2 bilayers[39] . Figure 1.3 (Chapter 1) shows that a previously reported WSe_2 bilayer was strained up to 1.5% with an overestimated and constantly decreasing Grüneisen parameter over their entire strain range. This is an unphysical result, which is indicative of non-uniform application of strain the previous report of Desai *et al.*[50] In contrast, our result shows consistent Grüneisen parameters of all three Raman active modes up to 3.59% uniaxial tensile strain, and it is comparable with previous reported monolayer MoS_2[47].

Regarding the direct and indirect bang gap energies, we deconvoluted the photoluminescence spectra reported in ref. 50. We have examined the optical indirect and direct band gap energy evolution with strain (Figure 3.13) to conclude that there is no evidence that the indirect-to-direct transition was observed in that report and that the PL intensity enhancement is instead due to the decreasing of the direct band gap energy and an increasing of indirect band gap energy rather than band gap type switching.

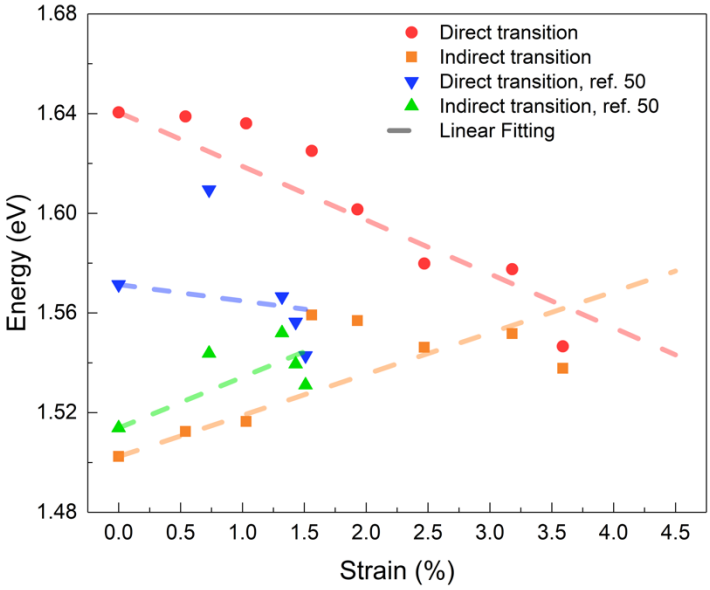

Figure 3. 13 Comparison of experimentally observed optical direct and indirect band gap energy in this thesis (red circles, orange squares) and in a report by Desai *et al.*[50] (blue and green triangles). The direct and indirect band gap energies for the previous work[50] are obtained by deconvolution of the photoluminescence spectra reported in that publication.

3.7 Conclusion

In conclusion, we have demonstrated that a two orders of magnitude photoluminescence enhancement in WSe_2 bilayers stems from strain-dependent electronic band gap evolution in the elastic regime. The encapsulation technique and four-point bending method developed for this thesis enable us to apply up to ~3.59% uniaxial strain on our atomically thin material while preventing sample degradation from exposure to air during thermal processing and laser irradiation. We have postulated an important materials design guideline related to band degeneracy as suppression of intervalley electron scattering events through band engineering may lead to further increases in emission enhancement. This thesis also demonstrates the necessity of considering van der Waals interactions and the Poisson effect in the atomically thin material's surrounding environment for theoretical predictions of strain-coupled optoelectronic phenomena.

Chapter 4: Single Photon Source in Atomically Thin Transition Metal Dichalcogenides

4.1 Epitaxial Nominally Bilayer WSe_2 Growth and Characterization

Scalability issues in the synthesis of two-dimensional (2D) materials is a major roadblock to large-scale device integration. The powder vaporization[119,146-148] chemical vapor deposition has been widely adopted as previous session shown, but it usually results in the non-continuous crystals with dimensions as tens of μm. To overcome the scalability challenges, the chemical vapor deposition-based techniques using gaseous sources offer accessibility for wafer scale integration was used here. The epitaxial wafer-scale WSe_2 used in this chapter was provided by Prof. Joan M. Redwing of the 2D Crystal Consortium–Materials Innovation Platform at The Pennsylvania State University and synthesized according to ref. 149. The synthesis method employs $W(CO)_6$ and H_2Se vapor-phase sources enabling control over WSe_2 nucleation density and lateral domain growth which are necessary to achieve uniform epitaxial films on sapphire (0001). Our nominally bilayer WSe_2 was grown by a recently developed vertical cold-wall CVD reaction scheme[149] to deposit WSe_2 over a roughly 1 cm^2 sapphire *c*-plane (0001) substrate, where the above challenges have been solved by using H_2Se as the selenium precursor with a significant amount of excess chalcogen - Se: W ratio of ~26,000: 1 - to obtain stoichiometric and uniform films verified by X-ray photoelectron spectroscopy as shown in Figure 4.1. The PL mapping at cryo-temperature, 4K, was also conducted for as-grown WSe_2 on sapphire as Figure 4.2 showing. It is showing no PL-observable defect emission peak in as-grown WSe_2 on sapphire through the entire mapping region.

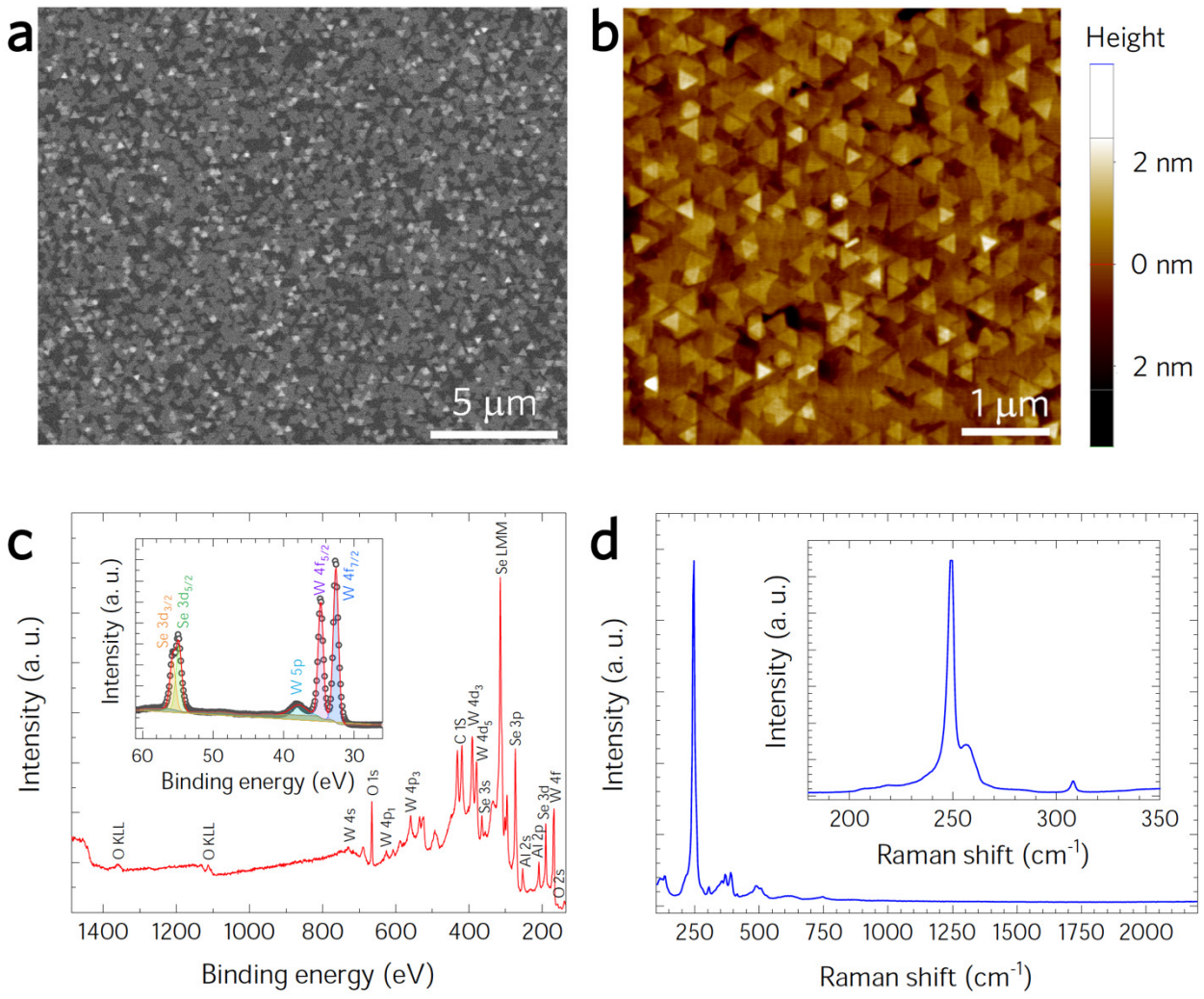

Figure 4. 1 Wafer-scale, nominally bilayer epitaxial WSe_2 synthesized on *c*-plane sapphire. (a) Scanning electron micrographs showing large-area coalesced and uniform coverage of small-grain size WSe_2 synthesized by gas source chemical vapor deposition. (b) Atomic force microscopy analysis showing textured growth of predominantly bilayer to trilayer WSe_2. (c) X-ray photoelectron spectroscopy analysis demonstrates a 1:2 atomic ratio tungsten:selenium, and no detectable coordination with oxygen. (d) Raman spectroscopy exhibits no carbonaceous peaks and indicates 2–3 layer WSe_2 (inset).

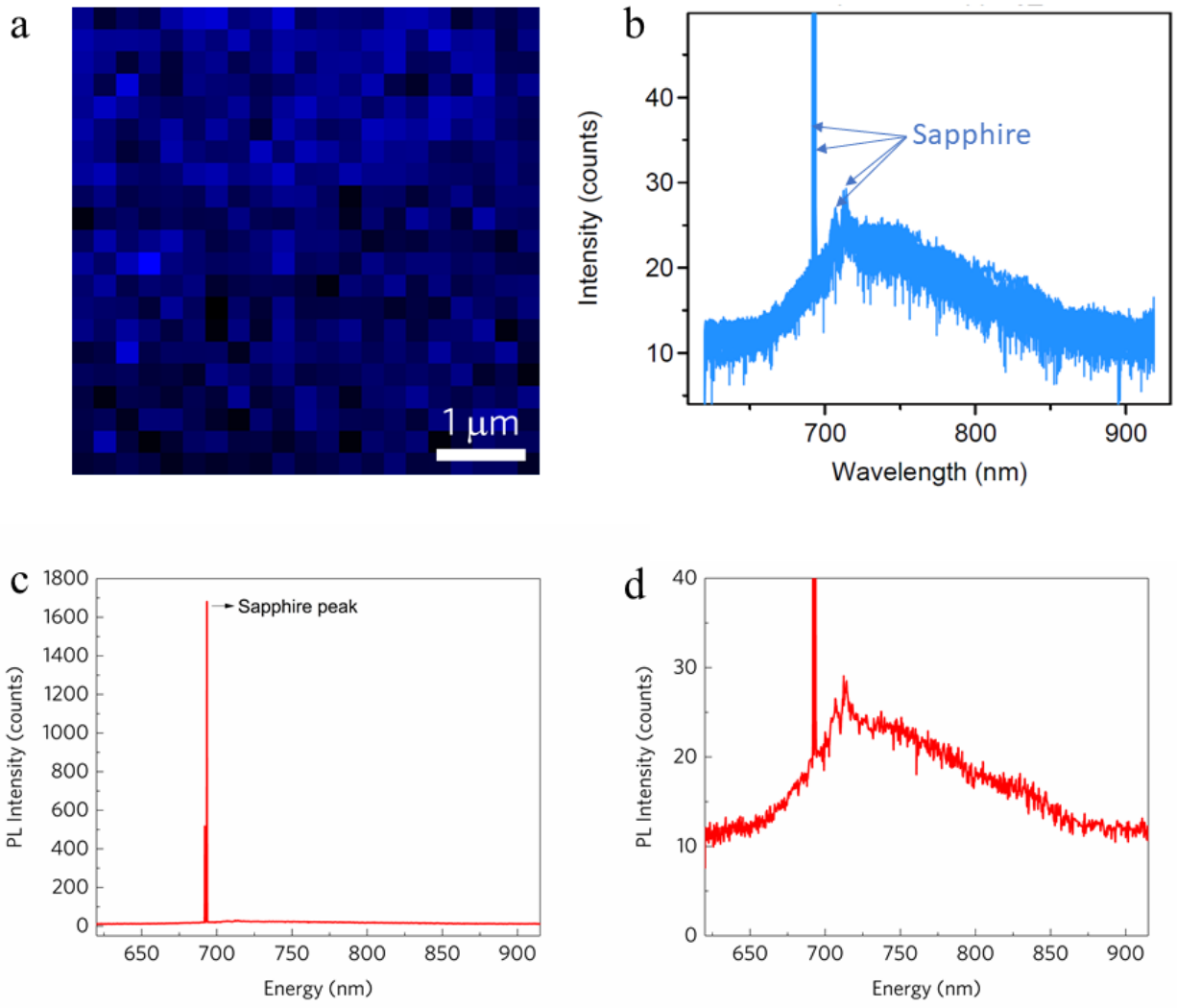

Figure 4. 2 The photoluminescence mapping at 4K of as-grown WSe_2 on sapphire *c*-plane (0001) substrate. (a) Photoluminescence mapping of emission peak center at 758 nm at 4K temperature. (b) All PL spectra of mapping shows no defect emission from WSe_2 at each pixel. (c) The point-PL emission spectra show two high intensity PL peak originating from sapphire. (d) Point-PL spectra shows the emission of nominally bilayer WSe_2 on sapphire.

4.2 Transfer Epitaxial Nominally Bilayer WSe_2 onto Sharp Tip Arrays

Transfer of the WSe_2 film from the sapphire substrate to the ultra-sharp tips was carried out by spin-coating 950,000 molecular weight PMMA (4% in anisole) onto the WSe_2/sapphire substrate at 1000 rpm for 1 minute without postbaking, which resulted in a ~ 500 nm thick film. A 2.5 M potassium hydroxide (KOH) solution was used to etch the growth substrate and release the PMMA/WSe_2 composite film which was then thoroughly rinsed in deionized water. To minimize or prevent puncture, we placed the composite film so that the PMMA acted as a buffer layer between the WSe_2 and the sharp tip. We loaded the substrate into a tube furnace with 100 sccm nitrogen, purged for 2 hours, and then increased the temperature slowly from 25–400°C in 3 hours. The slow ramp rate softened the PMMA first to ensure contact between tip and PMMA. Thermal annealing at 400°C under nitrogen for 1 hour was then was used to remove residual PMMA and create a conformal WSe_2 film over the sharp SiO_2 tips, after which the furnace lid was opened and allowed to cool to room temperature under nitrogen flow. Figure 4.3 shows the sample wafer-scale transfer process before and after PMMA removal.

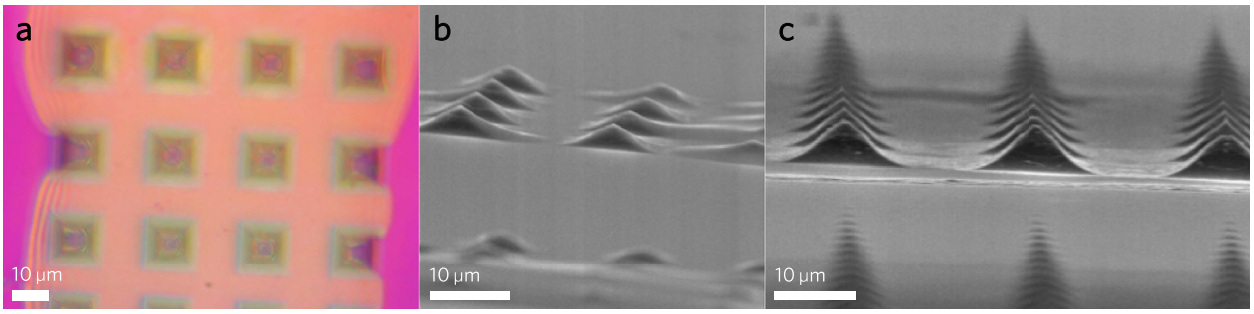

Figure 4. 3 Demonstration of ability to transfer of large-area WSe_2 onto ultra-sharp tip arrays. (a) Optical microscopy and (b) scanning electron microscopy images of MOCVD-grown nominally bilayer WSe_2 coated with ~500 nm of poly(methyl methacrylate) (PMMA) transferred onto a tip array. (c) Scanning electron microscopy image of the WSe_2 on the tip array after removal of PMMA with acetone and hydrogen annealing.

We postulate that spatially controlled bending based on the sharp radius of the tips gives rise to electronic localization effects through morphology alone, as the WSe_2 experiences a uniform SiO_2 dielectric environment in the device geometry chosen for this investigation. Figure 4.4a and b illustrate that for a 1–5-layer sample placed onto a 10-nm diameter tip, a maximum strain of 3.2–16.2 % will arise with an ultra-high strain gradient on the order of 10^{10} $\%m^{-1}$. The strain is estimated as:

$$\varepsilon = \tau / r \tag{6.1}$$

where τ is the half thickness of bilayer WSe_2, r is the sharp tip radius.

This symmetric strain profile thus should have an observable effect on excitonic emission[39] and kinetics, although the true strain experienced will depend on a number of other issues such as

compliance. The relationship of thermal expansion coefficient (α) to elastic modulus (E) can be expressed as $\alpha = \gamma\rho c_v/E$, where γ is the Grüneisen parameter, ρ is the mass density, and c_v is the specific heat. Since this thermophysical property is inversely proportional to the elastic constant, and since α has been recently reported to increase significantly as layer number is reduced[37], it is likely that mono- and few-layer TMD materials are more compliant than their bulk counterparts and thus more able to be strained locally by the sharp tips.

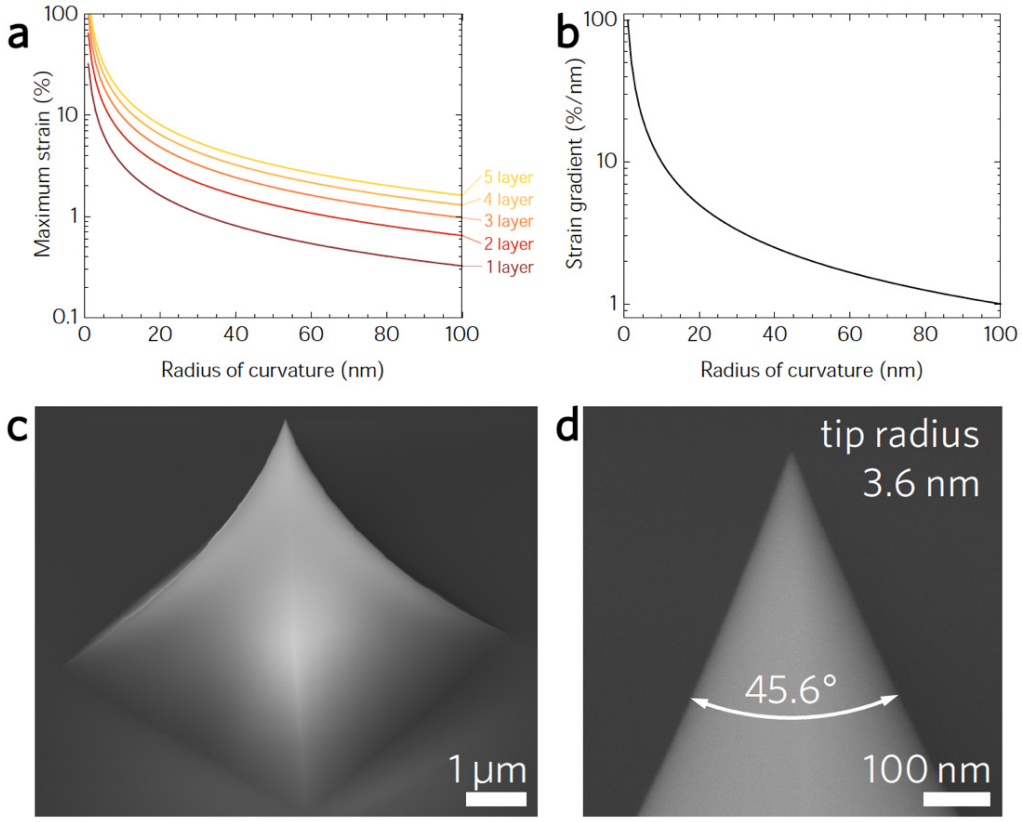

Figure 4. 4 Ultra-large strain and strain gradients are possible for atomically thin crystals transferred onto ultra-sharp tips. (a) Calculated maximum strain that will arise on the top (tensile) and bottom (compressive) surfaces of an n-layer WSe_2 film as a function of tip radius according to equation 6.1. (b) Calculated strain gradient occurring across the sample. (c-d) Scanning electron micrographs of a representative sharp tip.

4.3 Single Photon Emission in Epitaxial Nominally Bilayer WSe_2

4.3.1 Continuous-wave Photoluminescence Spectroscopy of Epitaxial Nominally Bilayer WSe_2 on Sharp Tip

The spatial continuous-wave PL emission spectra of WSe_2 is obtained using a confocal Raman micro-spectrometer (LabRAM HR Evolution, Horiba Scientific, Ltd.) with a 2.33 eV (λ = 532 nm) continuous wave excitation at low power (86 μW) to avoid sample damage and spectral shifts due to local heating effects[47]. The sample temperature is controlled between 4K to room temperature by Janis continuous flow cryostat with flowing liquid helium. Although the laser beam diameter is ~250 nm, the mapping spatial resolution is set to 2 μm due to the beam reflection and interference effect when passing through the optical viewport of cryostat.

Figure 4.5 gives the photoluminescence intensity mapping of the emission peak at 758 nm over a sharp tip at liquid helium temperature, 4.14 K. It shows the defect originating from the exact tip center within the spatial resolution of the excitation beam. Since the sharp tip is relative high, few μm, the laser focal plane may not correctly set and cause non-identical background signal among each site. It is necessary to remove the background signal firstly. Figure 4.5b shows the PL intensity mapping of peak at 758 nm after background signal removal.

As the laser moves away from the apex of the sharp tip, the emission intensity decreases and eventually disappears at the flat part of substrate. As the geometry of sharp tip showing in Figure 4.4c and d, the applied local strain on WSe_2 also gradually decreases when the location moves away from the apex of sharp tip. The consistent changing trend between emission intensity

and local strain distribution indicates the emission stems from the strain induced engineered defects on nominally bilayer WSe_2.

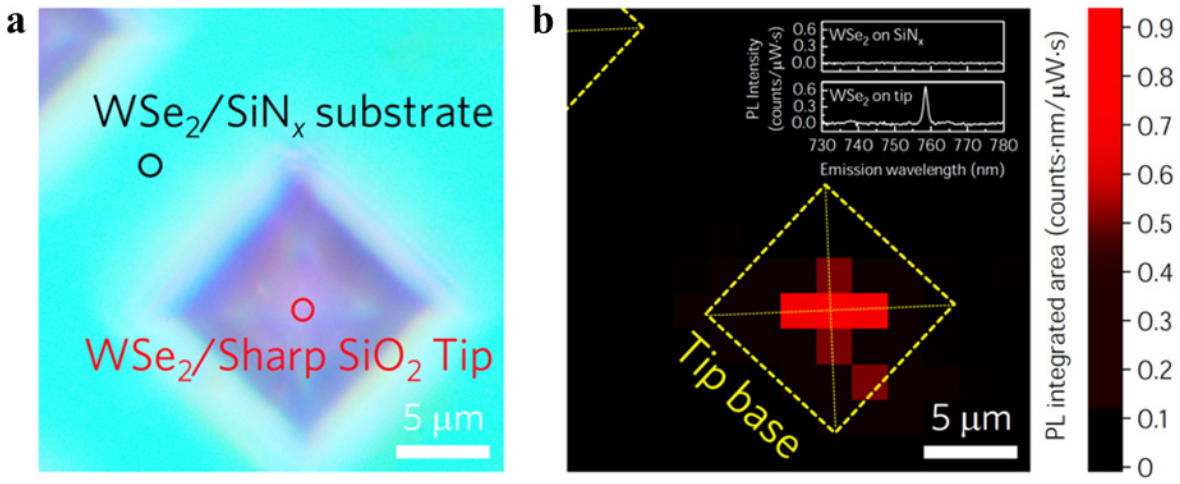

Figure 4. 5 Continuous-wave photoluminescence spectra shows the engineered emission sites. (a) Optical micrograph and (b) spatial continuous-wave excitation PL of nominally bilayer epitaxial WSe_2 transferred onto an ultra-sharp SiO_2 tip on a SiN_x-on-Si substrate, where the integrated area of the localized exciton peak over the free exciton is shown versus x-y coordinate.

4.3.2 Power and Temperature Dependent Photoluminescence of Epitaxial Nominally Bilayer WSe_2 on Sharp Tip

The operation temperature of the quantum emitter was examined by the temperature dependent PL spectra, obtained by Dr. C. Kavir Dass and Dr. Joshua R. Hendrickson at the U. S. Air Force Research Laboratory in Dayton, Ohio. Figure 4.6 gives the temperature dependent emission spectra of a localized quantum emission site. Over the temperature range of 3.5–25 K, the emission energy remains relatively constant with a mean and standard deviation of 772.953 nm (1.604 eV) and 0.830 nm (1.72 meV), respectively. The emission peak center wavelength shows consistent over 3.5-25 K indicating the stability of the emitters characterized in this thesis. The emission intensity is depressed when temperature increasing. Similar to previous studies[6-12,16,83], localized emission is not observable at temperatures above 25 K.

The power dependent PL peak emission wavelength is also studied in this thesis, center wavelength 772.882 nm (1.604 eV) and a standard deviation of 0.274 nm (0.57 meV) as shown in Figure 4.7, which agrees with temperature depend PL spectra showing in Figure 4.6.

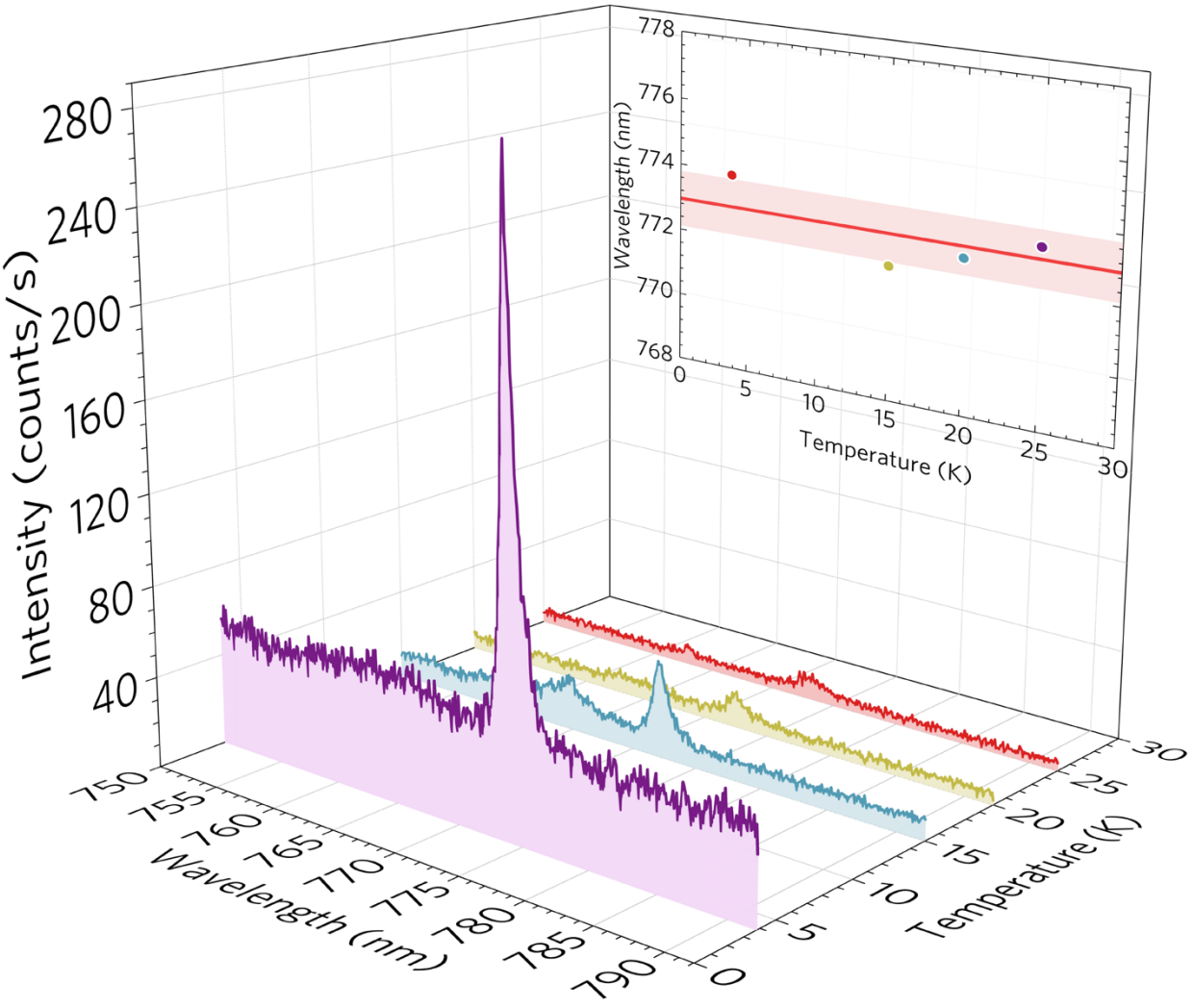

Figure 4. 6 Temperature dependence of localized emission. Photoluminescence spectra of localized emission from WSe_2 on an ultra-sharp SiO_2 tip as a function of temperature obtained using femtosecond excitation at 540 nm. Inset shows that the peak emission wavelength is relatively constant over the measured temperature range with a mean of 772.95 nm and a standard deviation of 0.83 nm. This experiment was conducted by Dr. C. Kavir Dass and Dr. Joshua R. Hendrickson at the U. S. Air Force Research Laboratory in Dayton, Ohio.

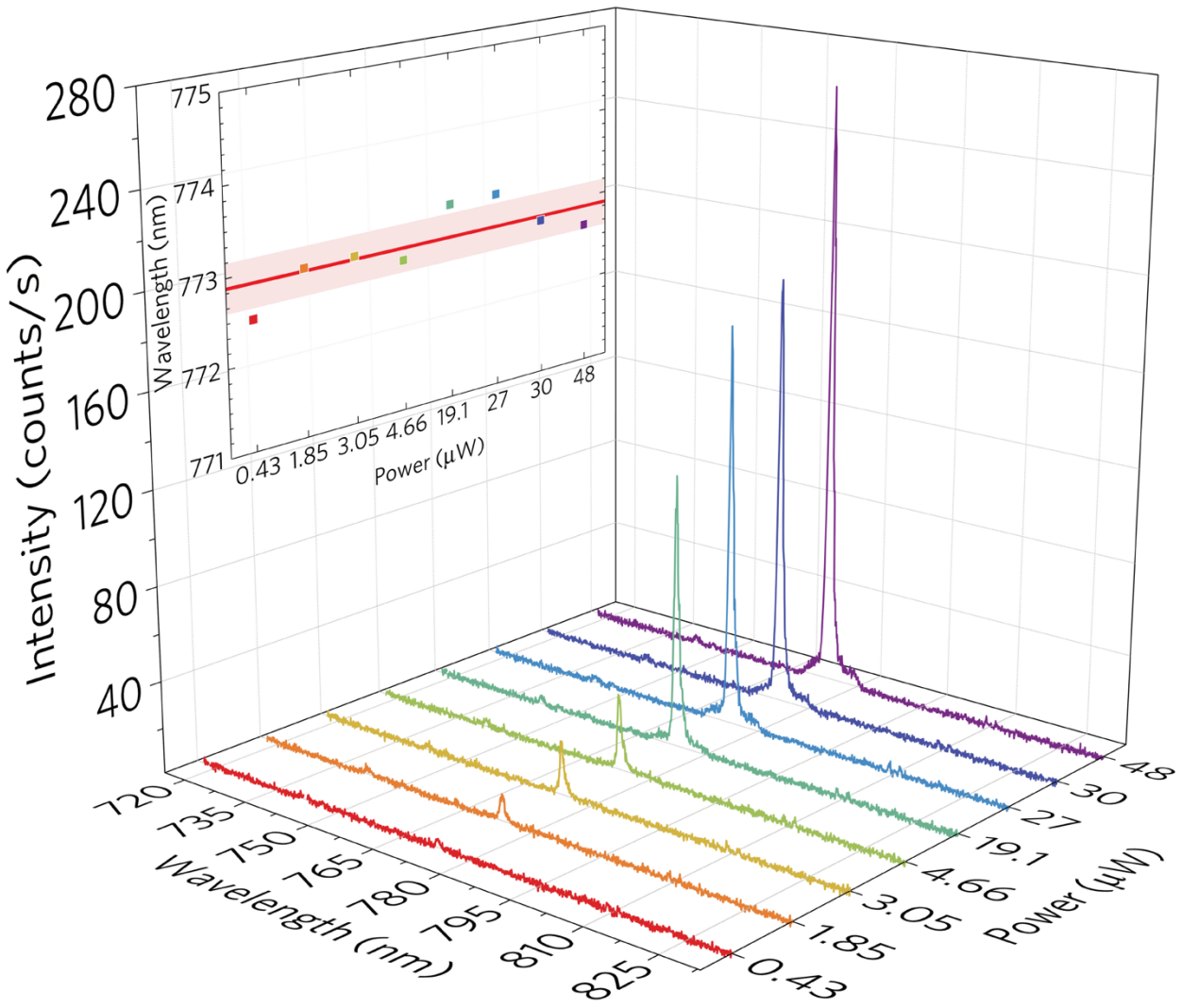

Figure 4. 7 Power dependent PL spectra of localized emission. (inset) Peak emission wavelength is relatively constant over the measured excitation power range with a mean of 772.88 nm and a standard deviation of 0.27 nm. This experiment was conducted by Dr. C. Kavir Dass and Dr. Joshua R. Hendrickson at the U. S. Air Force Research Laboratory in Dayton, Ohio.

4.3.3 Time Resolved Photoluminescence of Epitaxial Nominally Bilayer WSe_2 on Sharp Tip

In order to determine the underlying carrier relaxation dynamics and single photon generation characteristics of the WSe_2, ultra-fast optical characterization was performed using a Ti:Sapphire femtosecond laser (140 fs, 80 MHz repetition rate) for time resolved photoluminescence (TRPL) and Hanbury Brown-Twiss (HBT) interferometry was performed using a HeNe continuous wave laser with spectral windows defined by inserting band-pass and tunable long- and short-pass filters into the beam path. Figure 4.8 gives the spectroscopic characterization results of optical emission arising WSe_2 on the apex of an ultra-sharp SiO_2 tip. The TRPL spectra was obtained by Dr. C. Kavir Dass and Dr. Joshua R. Hendrickson at the U. S. Air Force Research Laboratory in Dayton, Ohio.

The gas source CVD WSe_2 films contain grains smaller than the 0.7–1 μm excitation beam diameter, thus the contribution of grain boundary defects to quantum emission is an additioanl remaining unknown in this field. As the TRPL intensity $I(\Delta t)$ at any defect emission wavelength contains contributions from both free and localized (bound) excitons, we implement a bi-exponential rise and decay model to gain insight into the lifetimes of bound and free excitons as

$$I(\Delta t) - I_{\text{bkgd}} = \sum_{j=\text{fast, slow}} \sum_{i=-\infty}^{\infty} I_{0,j} \left[\left(e^{+(\Delta t - iT)/\tau_{\text{rise},j}} \right)^{-1} + \left(e^{-(\Delta t - iT)/\tau_{\text{decay},j}} \right)^{-1} \right]^{-1} \quad (6.2)$$

where I_{bkgd} is the background count rate, the subscript j indicates the fast and slow processes which we attribute to free and localized excitons respectively, the subscript i is the peak index, $I_{0,j}$ is the exciton emission intensity, Δt is the time delay, T is the period, and $\tau_{\text{rise},j}$ and $\tau_{\text{decay},j}$ are the characteristic lifetimes of excitonic rise and decay respectively. The experimental and fitted data is shown in Figure 4.8.

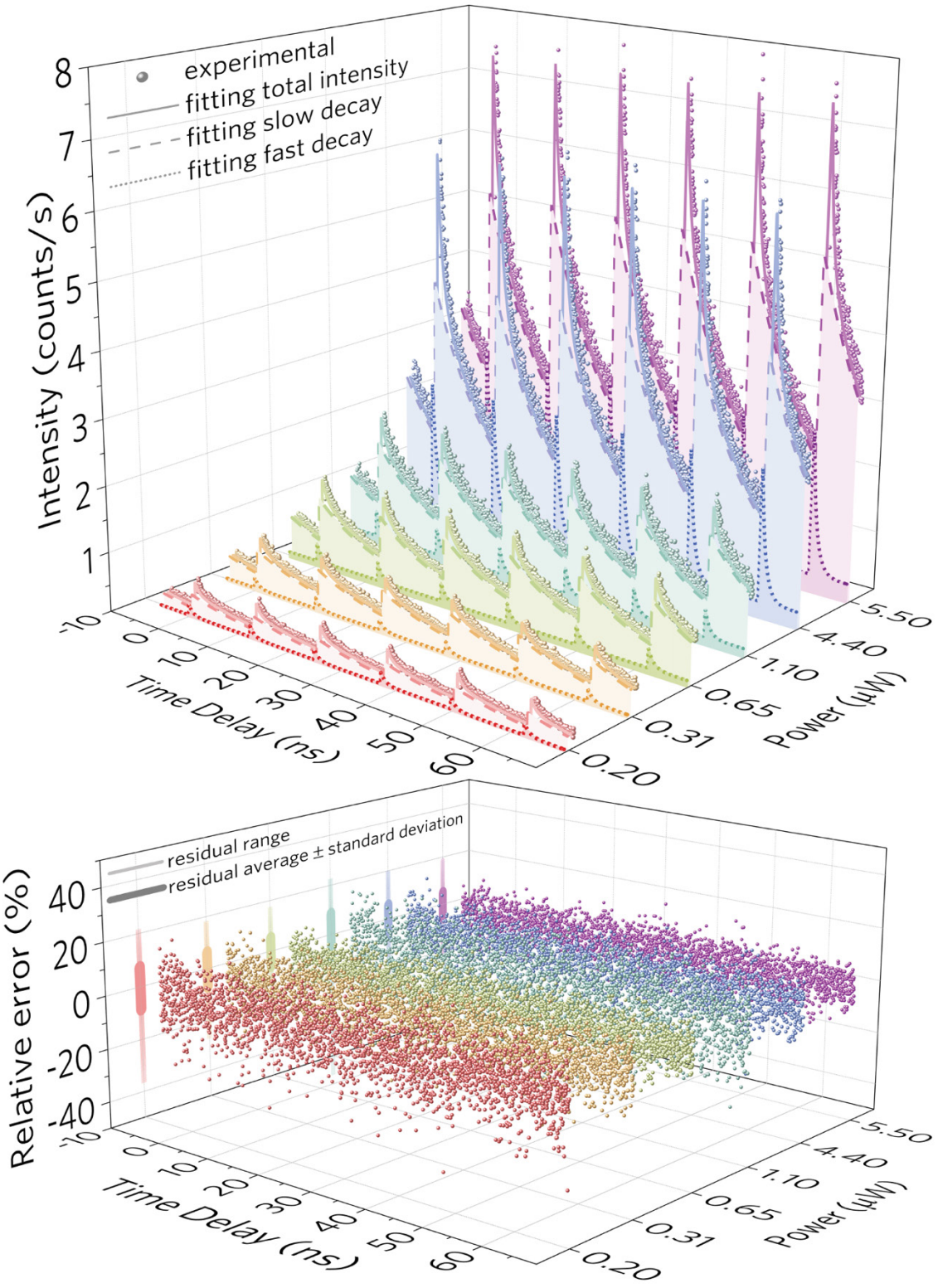

Figure 4. 8 Time resolved photoluminescence (TRPL) spectra of localized emission from WSe_2 on an ultra-sharp SiO_2 tip as a function of average excitation power obtained using femtosecond

excitation at 540 nm. Equation 6.2 is used to deconvolve free (fast decay, dotted line) and bound (slow decay, dashed line) exciton contributions to the measured event count. The bottom graph shows the fitting residue at each laser power. This experiment was conducted by Dr. C. Kavir Dass and Dr. Joshua Hendrickson at the U. S. Air Force Research Laboratory in Dayton, Ohio.

The second order photon correlation can be described as the probability of detecting a photon in the time frame of Δt as[150]:

$$g^{(2)}(\Delta t) = \frac{\langle I(t)I(t+\Delta t)\rangle}{\langle I(t)\rangle^2}, \tag{6.2}$$

where $\langle\ \rangle$ express the statistical average, $I(t)$ and $I(t+\Delta t)$ indicate the detected photon number at time of t and $t+\Delta t$. The time-dependent photon field intensity correlation, $g^{(2)}(\Delta t)$, for an engineered localized emitter is shown in Figure 4.8 which proves spatially localized quantum emission at the apex of an ultra-sharp SiO_2 tip at ~ 3.5 K (measurement conducted by Dr. C. Kavir Dass and Dr. Joshua R. Hendrickson at the U. S. Air Force Research Laboratory in Dayton, Ohio). The data can be modeled using a single exponential decay (two level) photon antibunching model[13]:

$$g^{(2)}(\Delta t) = 1 - [1 - g^{(2)}(\Delta t{=}0)]\, e^{-|\Delta t|/\tau_{\text{decay}}}, \tag{6.3}$$

where Δt is the time delay, τ_{decay} is the lifetime, and $g^{(2)}(\Delta t{=}0)$ is the second order photon correlation parameter for single photon emission, and $[1 - g^{(2)}(\Delta t{=}0)]$ is defined as the single photon purity. A high degree of photon antibunching was obtained $g^{(2)}(0) < 0.3$ over a 0.75 h collection time, and exhibited stable emission up to 8 hours. Such long collection times were

needed as the event count rate at the single photon detectors was on the order of several thousand events per second, in contrast to state-of-the-art diamond nitrogen-vacancy complexes[68,151] which emit ~10^5–10^6 s^{-1}. Improving the emission rate for the engineered emission sites in this thesis may be possible using resonant excitation[152].

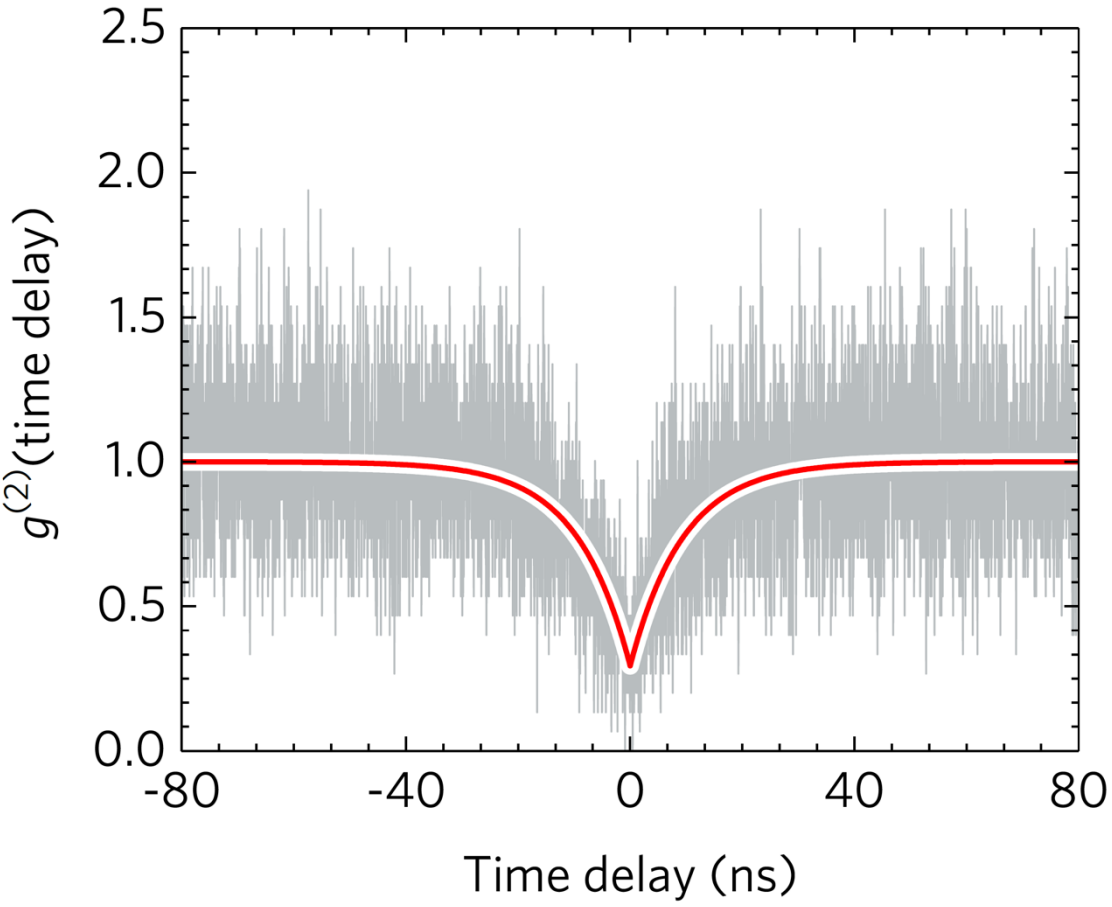

Figure 4. 9 Second order photon correlation of nominally bilayer WSe_2 on the apex of sharp tip. Measured second order photon correlation $g^{(2)}(\Delta t)$ obtained using continuous wave excitation at 532 nm and collected at $\lambda_{emission}$ = 772.9 nm using short- and long-pass tunable filters for a collection period of 45 minutes as a function of time delay Δt. This experiment was conducted by Dr. C. Kavir Dass and Dr. Joshua Hendrickson at the U. S. Air Force Research Laboratory in Dayton, Ohio.

4.3.4 Polarized Photoluminescence of Epitaxial Nominally Bilayer WSe_2 on Sharp Tip

The emission is random-unpolarized when excited with linearly polarized light with a polarizer placed in the collection beam path. We note that if the emission site was actually localized because of a symmetric strain potential then there would be no preferred polarization to the emitter, as we observed. This is unlike the case of an intrinsic defect localization, where the defect is likely to have some trap potential asymmetries. In comparison to this thesis, the pillars used in previous works[7,8] are quite wide (150–280 nm diameter) with observable asymmetry, which may explain why those works observe fine structure splitting and we do not. We note that to conclusively establish mechanisms resulting in strain-based quantum emission, the atomic arrangement and induced defect structures located at the tip apex will need to be studied in more detail both through experiment and theory.

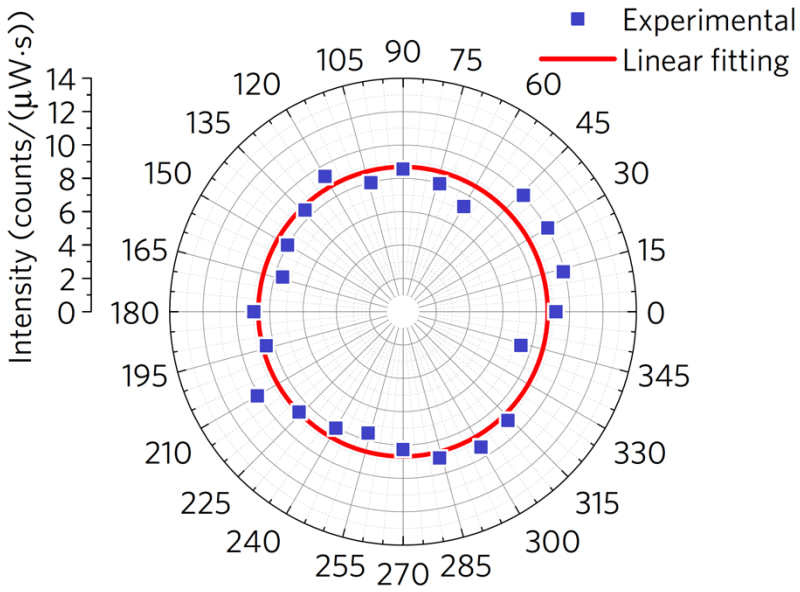

Figure 4. 10 Polarization dependence of the localized peak emission intensity (squares) demonstrates no preferential orientation of the emitted photons, which can be fit as 8.68±0.18 counts$\cdot s^{-1}\cdot\mu W^{-1}$ (line).

4.4 Continuous-wave Photoluminescence from Intrinsic Defects

We note that WSe_2 thin films can contain different types of intrinsic defect beside strain engineered defect discussed in above sessions. First, the WSe_2 contains grains smaller than the 0.7–1 μm excitation beam diameter which results grain boundary defects to quantum emission. Second, the W- or Se- defects can be created during growth duo to non-equilibrium growth condition. Thirdly, the introduced defects may be caused by transfer process. In this session, we focus the intrinsic defects created during sample transfer process. Figure 4.11 shows the defect PL emissions at ~740, 750, and 765 nm center wavelength of WSe_2 over a sharp tip which optical image was shown in Figure 4.11. In contrast with the emission mapping of 758nm peak, the mapping shows difference distribution which is not in agreement with sharp tip location. We believe these types of defect is intrinsic from growth or created during WSe_2 transfer process due to the location mismatch between these emission sites and sharp tip, instead of stemming from strain effect. However, we were not able to examine the seconder order photon correlation of these intrinsic defect sites and thus more focused experiments are required to understand intrinsic localized emitters in epitaxial WSe_2, which may be influenced by surface conditions as shown for other 2D materials[20,153-156].

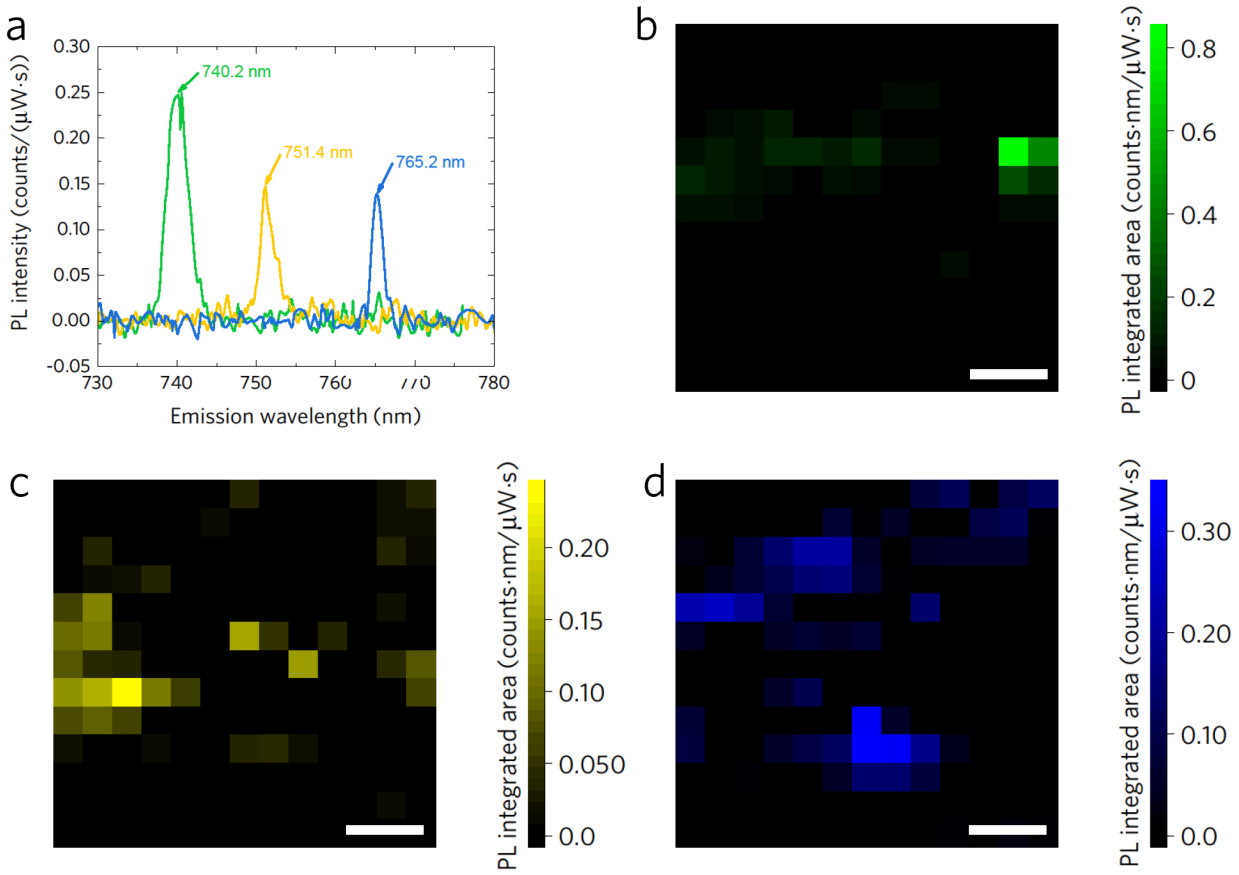

Figure 4. 11 Continuous-wave spatial photoluminescence of WSe_2. (a) PL intensity of three intrinsic defect emission peaks. Spatial PL mapping of emission peaks at (b) 740 nm, (c) 750 nm, and (d) 765 nm. The peaks shown in (a) are obtained from the brightest pixel in corresponding panels (b-d) and are weaker than the quantum emitter detected on the sharp tip apex (see Figure 4.5b).

4.5 Conclusion

In conclusion, we have demonstrated a new route to engineer spatially localized defect emission sites in the 750–800 nm regime using epitaxial nominally bilayer WSe_2 and ultra-sharp SiO_2 tip arrays. Engineering of quantum emission in 2D materials is still in a very early stage, and further efforts are required to increase the yield of deterministically placed quantum emitters and the thermal detrapping energy for room-temperature operation. Future large scale statistical investigations are also required to better understand defect emission including fine structure and polarization characteristics in the 2D material/ultra-sharp tip array system.

Chapter 5: Isotope Effect on the Indirect Excitonic Transition in an Atomically-thin Transition Metal Dichalcogenides

5.1 Phonon Dispersion of Naturally Abundant and Isotopically Pure WSe_2 Bilayers

Atomic vibrations described as phonons have energies which are dependent on the atomic mass, where frequency changes stemming from isotopic substitution can be monitored by Raman spectroscopy[157]. Figure 5.1a and b show the evolution of optical phonon energies with temperature in $^{NA}W^{NA}Se_2$ and $^{186}W^{80}Se_2$ bilayers using Raman spectroscopy and 532 nm laser excitation with a point-to-point resolution of ~0.51 cm^{-1} using an 1800 gr/mm grating. To minimize the instrumental uncertainty, we conducted 6 sets of measurements with spectral windows defined by initial points differing by 0.1 cm^{-1} to fully cover the point-to-point separation. The mean and standard deviation of modeled peak positions and full width at half maximum (FWHM) obtained for each of these 6 spectra was used as the uncertainty for each data point. To avoid any influence from the slightly non-uniform temperature distribution on the sample mount in the optical cryostat, all Raman spectra were aligned using the silicon substrate peak at each nominal temperature.

The frequency of optical lattice vibrations is expected to decrease with heavier isotopic atomic mass according to a simple one-dimensional harmonic oscillator model[94] as $\omega = [2C/(M_1^{-1}+M_2^{-1})]^{1/2}$ for zone center and $\omega = (2C/M_j)^{1/2}$, j = 1,2, for zone boundary phonons where C is the force constant and M_i is the mass of the j-th atom in the two atom basis chain. The experimental frequency difference between $^{NA}W^{NA}Se_2$ and $^{186}W^{80}Se_2$ bilayers for each Raman active mode is evaluated as $\Delta\omega_i = \omega_{i,NA} - \omega_{i,isotope}$, $i = E_{2g}, A_{1g}, A_{1g}^2$, where ω_i is the Raman peak frequency of the i-th Raman active mode. Figures 2c and 3 show that the phonon frequency globally red-shifts in the isotopic samples over the entire temperature range from 4.41 to 300 K. The E_{2g} mode

corresponds to intralayer tungsten and selenium atoms vibrating against each other in the hexagonal basal plane, in which the phonon frequency difference between $^{NA}W^{NA}Se_2$ and $^{186}W^{80}Se_2$ bilayers is $\Delta\omega_{E_{2g}}$ = 1.378±0.048 cm^{-1}. The A_{1g} mode represents selenium atom vibrations along the out-of-plane direction with $\Delta\omega_{A_{1g}}$ = 1.526±0.072 cm^{-1}. The more interesting mode here is A_{1g}^2 with $\Delta\omega_{A_{1g}^2}$ = 1.942±0.061 cm^{-1}. The A_{1g}^2 mode represents an interlayer vibration involving both tungsten and selenium atoms from different van der Waals layers, and only appears for two or more layers of WSe_2[112]. We observe that the isotopic effect on the interlayer out-of-plane A_{1g}^2 mode is larger than on the in-plane E_{2g} mode or the intralayer out-of-plane A_{1g} mode, which arises from the fact that the isotopic effect on the weak interlayer van der Waals interaction is larger than it is on the strong intralayer W-Se covalent interaction.

Besides the harmonic oscillation of phonons, the contribution of van der Waals bond length on phonon frequency also needs to be evaluated to support the statement above. The phonon frequency changes due to strain can be defined as[39] $\Delta\omega_{i,\text{strain}} = -\varepsilon\gamma_i\omega_i$ where γ is the Grüneisen parameter, ε is the hydrostatic strain, and i represents the phonon mode. The interlayer van der Waals bond length change can be treated as $\Delta c = \varepsilon c$ where Δc is the c-lattice parameter change due to isotopic substitution and c is the natural abundance c-lattice parameter, and ε_{zz} is the out-of-plane strain component. Thus, the phonon frequency change due to isotopic substitution in this thesis can be approximated as $\Delta\omega_{i,\text{strain}} = -\gamma_i\omega_i\Delta c/c$. By adopting the experimental Grüneisen parameter of the A_{1g}^2 mode in bilayer WSe_2 as 0.357[39] and the c-lattice parameters obtained from XRD analysis the phonon frequency changes expected due to isotope induced changes in van der Waals bond length can be estimated on the order of $\Delta\omega_{A_{1g}^2,\text{strain}}$ = 0.04 cm^{-1}, which is negligible compared to the measured experimental frequency changes.

The phonon lifetime is an important parameter that describes phonon scattering processes, and can be estimated from the FWHM of the Raman peak as[158] $\tau = \hbar/\Gamma$ where τ is the phonon lifetime, $\hbar$ is the reduced Planck constant, and Γ is the FWHM. Figure 2d,e illustrates that isotopically pure $^{186}W^{80}Se_2$ exhibits larger phonon lifetimes for both the intralayer in-plane E_{2g} mode and the interlayer out-of-plane A_{1g}^2 mode, which is expected due to the two-orders of magnitude higher mass variance parameter in the naturally abundant sample than the purified sample. The observed decrease of the phonon lifetime with temperature arises from an increase of phonon occupancy and phonon-phonon interaction with temperature[159]. At 4.41 K, the phonon lifetime of bilayer $^{186}W^{80}Se_2$ is ~2.9 ps for the E_{2g} mode and ~2.2 ps for the A_{1g}^2 mode which is 11.5% and 15.8% higher than that of bilayer $^{NA}W^{NA}Se_2$.

Figure 5.1 a-c shows the temperature dependent Raman shift of the E_{2g}, A_{1g}, and A_{1g}^2 modes of bilayer $^{NA}W^{NA}Se_2$ and $^{186}W^{80}Se_2$. As the temperature increases from 4.41 to 300 K, the E_{2g} mode frequency decreases by 1.313±0.025 cm^{-1} in $^{NA}W^{NA}Se_2$ and by and 1.223±0.031 cm^{-1} in $^{186}W^{80}Se_2$. The A_{1g} mode frequency drops a similar amount over the same temperature range, 1.580±0.105 cm^{-1} and 1.533±0.055 cm^{-1} in $^{NA}W^{NA}Se_2$ and $^{186}W^{80}Se_2$ respectively. The A_{1g}^2 mode frequency drops by nearly twice as much, 2.575±0.031 cm^{-1} and 2.447±0.039 cm^{-1} in $^{NA}W^{NA}Se_2$ and $^{186}W^{80}Se_2$ bilayers respectively. This behavior can be explained by the positive thermal expansion coefficient (TEC) of both in-plane and out-of-plane unit cell parameters[37,160]. We observe that the out-of-plane vibrational modes – A_{1g} and A_{1g}^2 – have ~1.2 and ~1.9 times higher frequency changes than the in-plane vibration mode (E_{2g}), respectively, which arises from an out-of-plane TEC approximately 1.6 times higher than the in-plane TEC[160].

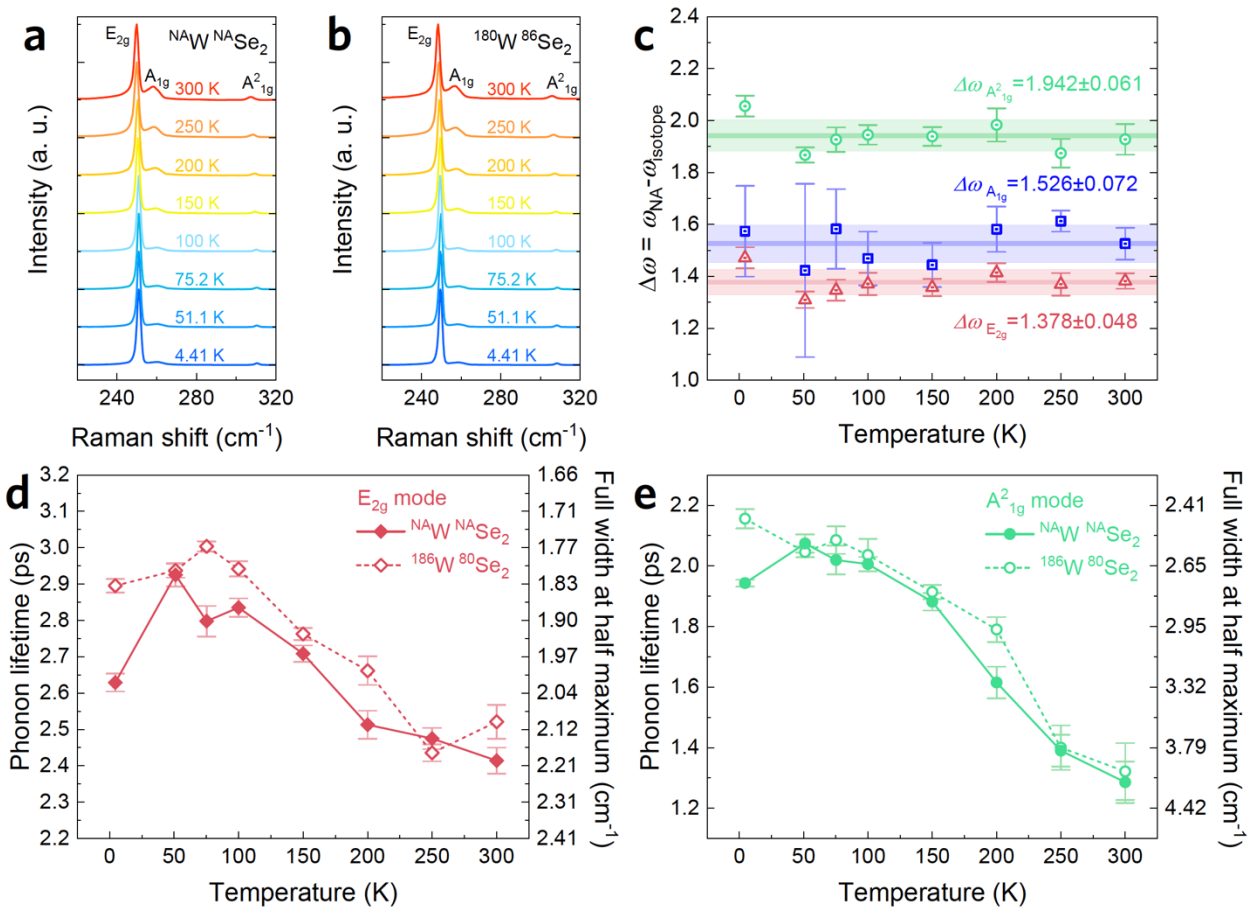

Figure 5. 1 Isotopic mass dependent Raman spectra of bilayer WSe_2. Normalized Raman spectra of (a) naturally abundant $^{NA}W^{NA}Se_2$, and (b) isotopically pure $^{186}W^{80}Se_2$ over the temperature range from 4.41 to 300 K. (c) The phonon frequency difference ($\Delta\omega$) of E_{2g} (red), A_{1g} (blue) and A^2_{1g} (green) modes between $^{NA}W^{NA}Se_2$ and $^{186}W^{80}Se_2$, where error is defined by the standard deviation of 6 measurements each with a different spectral window initial point in order to minimize the instrumental uncertainty. Temperature-dependent phonon lifetime and full width at half maximum of the (d) E_{2g} mode and (e) A^2_{1g} mode from 4.41 to 300 K.

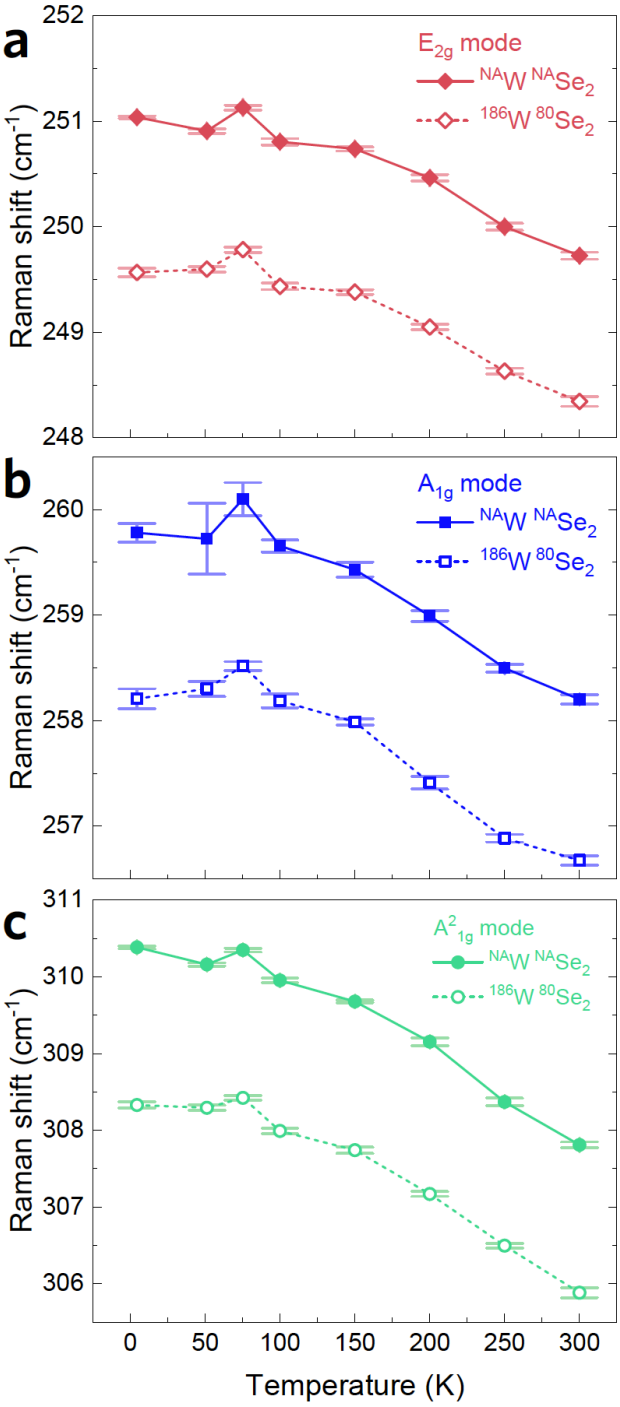

Figure 5. 2 Temperature dependence of Raman active mode peak positions isotopically engineered bilayer WSe_2. Raman shift for the (a) E_{2g}, (b) A_{1g}, and (c) A^2_{1g} modes of naturally abundant $^{NA}W^{NA}Se_2$ (solid symbols) and isotopically pure $^{186}W^{80}Se_2$ (open symbols).

5.2 Optical Band Gap of Naturally Abundant and Isotopically Pure WSe_2 Bilayers

Electronic transitions from filled to empty states must conserve electron momentum. Bilayer WSe_2 is known as a semiconductor with an indirect electronic band gap[32], in which the conduction band minimum at the Σ-point (CBM_Σ) and valence band maximum at the K-point (VBM_K) are not at the same electron momentum in reciprocal space. Since the momentum of photons is negligible, especially in the wavelength range used in this thesis, the transition between CBM_Σ and VBM_K must involve phonon assistance to obey the rule of momentum conservation, which means the band gap can be affected by the isotope effect. Figure 5.3 reports the temperature dependent PL spectra for bilayer $^{NA}W^{NA}Se_2$ and $^{186}W^{80}Se_2$. To avoid uncertainty arising from non-identical local heating by the excitation laser, all the samples were characterized under the same conditions including laser power and acquisition time at each temperature. Surprisingly, we observe a higher optical band gap energy in bilayer $^{186}W^{80}Se_2$ compared with bilayer $^{NA}W^{NA}Se_2$ where the PL spectra of the isotopically pure sample blue-shifts by 3.92 ±0.71 meV over the entire temperature range from 4.41 to 300 K (Fig. 5.3c). This trend is similar to the PL spectra blue-shift with increasing atomic mass phenomenon observed in other isotopically purified indirect band gap semiconductors, where the indirect band gap renormalization energy changes ~4.4 meV between *h*-$^{10}B^{NA}N$ and *h*-$^{NA}B^{NA}N$[88], and ~2.2 meV between ^{70}Ge and ^{76}Ge[99].

The mechanism responsible for this observable change in emission energy is indirect band gap renormalization[95]. When evaluating the normalized electronic states in an indirect band gap semiconductor, the band gap renormalization energy inversely proportional to the square root of effective mass and depends on the zero-point vibrational energy, calculated with all phonon modes at zero temperature. The isotope effect on indirect band gap renormalization energy has been proven in bulk *h*-BN[88]. It is also important to evaluate the contribution of van der Waals bond

length change to optical band gap energy, as out-of-plane compressive strain has been shown to decrease the indirect optical band gap energy in bilayer WSe_2[39]. A similar trend has also been predicted for bilayer MoS_2, in which the indirect band gap decreases with shorter *c*-lattice parameter[161]. This is contrary to our observation of the higher optical band gap in bilayer $^{186}W^{80}Se_2$ which possesses a smaller *c*-lattice parameter than $^{NA}W^{NA}Se_2$. Therefore, we conclude that the van der Waals bond length is not the dominant factor resulting in the optical band gap energy change with isotopic purification in this thesis.

The temperature evolution of the optical band gap is shown in Fig. 5.3d, which decreases from 1.649 eV at 4.41 K to 1.599 eV at 300 K for $^{NA}W^{NA}Se_2$ and from 1.652 eV at 4.41 K to 1.574 eV at 300 K for $^{186}W^{80}Se_2$. This behavior can be modeled using the empirical Varshni relation[162] as $E_g(T) = Eg(T=0) - (\alpha T^2)/(\beta+T)$ where $E_g(T=0)$ is the band gap energy at 0 K, T is the absolute temperature, and α and β are adjustable constants. We obtained $E_g(T=0)$=1.6504 eV, α = 0.365 meV/K, and β = 93.926 K for $^{NA}W^{NA}Se_2$, and $E_g(T=0)$=1.6539 eV, α = 0.379 meV/K and β = 112.964 K for $^{186}W^{80}Se_2$. Coefficients of determination were 0.991 and 0.992 for $^{NA}W^{NA}Se_2$ and $^{186}W^{80}Se_2$, respectively. The slight difference between our experimental data and the empirical modeling at low temperature arises from the quadratic temperature dependence of the empirical Varshni relation, whereas theoretical and experimental observations are reported to exhibit T^4 dependence at low temperature[95,163,164].

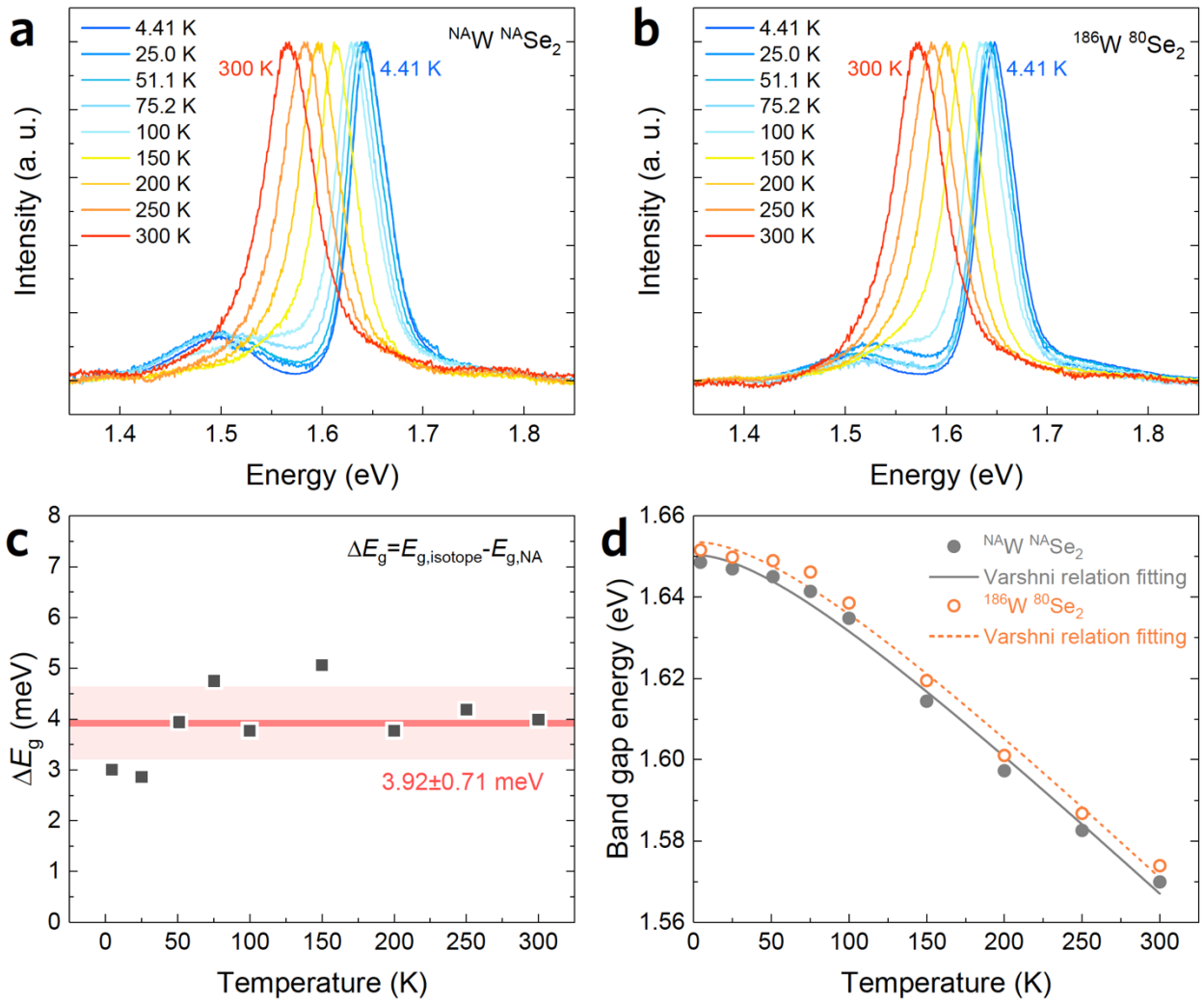

Figure 5. 3 Isotopic mass dependent photoluminescence and optical band gap. Normalized photoluminescence spectra over a temperature range from 4.41 to 300 K for (a) naturally abundant bilayer $^{NA}W^{NA}Se_2$, and (b) isotopically pure bilayer $^{186}W^{80}Se_2$. (c) Difference in optical band gap between $^{NA}W^{NA}Se_2$ and $^{186}W^{80}Se_2$. (d) Temperature dependence of the band gap of $^{NA}W^{NA}Se_2$ and $^{186}W^{80}Se_2$, where modeling results using the empirical Varshni relation are given by solid and dashed lines, respectively.

5.3 Conclusion

We present a new route of tuning the electronic band gap and phonon dispersion using isotope engineering in a semiconducting 2D crystal. The naturally abundant $^{Na}W^{Na}Se_2$ and isotopically enriched $^{186}W^{80}Se_2$ bilayers were grown by a chemical vapor deposition method under same growth conditions. The spatially resolved Raman and photoluminescence spectra show the uniformity of the bilayer samples which minimized the measurement uncertainty arising from sample-to-sample variation in crystal quality. Using X-ray diffraction, a shorter interlayer van der Waals bond was observed in a $^{186}W^{80}Se_2$ textured film (6.464 Å) than for a $^{Na}W^{Na}Se_2$ textured film (6.467 Å). The Raman spectra indicates that isotopic effects are more efficient for weak interlayer van der Waals interactions compared with strong intralayer covalent bonds. The very close full width at half maximum (FWHM) of PL emission in $^{Na}W^{Na}Se_2$ and $^{186}W^{80}Se_2$ bilayers indicated the observed difference in band gap does not arise from differences in crystalline quality. The observed band gap in a $^{186}W^{80}Se_2$ bilayer is larger than that of a $^{Na}W^{Na}Se_2$ bilayer by an amount ranging from ~2 nm to ~1.6 nm at various temperatures.

Chapter 6: Conclusion

This thesis aims to advance the knowledge of strain and isotopic effects on optoelectronic behavior in atomically thin van der Waals transition metal dichalcogenides (TMDs), specifically WSe_2, and to explore the promise of TMDs using these new phenomena in flexible and quantum emission applications.

A high repeatability vapor deposition (CVD) method for monolayer MoS_2 and bilayer WSe_2 using our own designed and built the modified CVD system was developed. The diffusion limited and mass limited growth regimes for monolayer MoS_2 showed different electronic band gap energies due to the crystalline imperfection from nucleation dots on top of crystal. The CVD grown bilayer WSe_2 has top and bottom layer sharing the same dimension and lattice orientation. The bilayer structure has been further confirmed by cross-section scanning transmission electron microscopy. Furthermore, the isotopically pure $^{186}W^{80}Se_2$ bilayer was synthesized by CVD method in order to study the isotopic effect on atomically thin TMDs.

The strain dependent optoelectronic transport and phonon dispersion relationship is examined using encapsulated CVD grown WSe_2 bilayers. A two-order of magnitude of photoluminescence (PL) response enhancement is observed at 3.59% uniaxially strained WSe_2 bilayer. The Grüneisen parameters of E_{2g}, A_{1g} and A^2_{1g} Raman active modes are measured as 1.149±0.027, 0.307±0.061, and 0.357±0.103 through whole strain range up to 3.59%. The encapsulation four-point bending method is verified by straining patterned and unpatterned monolayer graphene. The new technique achieves ~2 times higher strain value then previous reports.

A new route of creating spatially localized quantum emission sites is reported using a continuous epitaxial film of nominally bilayer WSe_2 on silicon oxide tip arrays. The second order photon correlation was measured as ~0.3, which confirms the single photon emission phenomenon.

The isotopic effect on phonon dispersion and electronic band gap energy is studied by examining CVD grown single crystal naturally abundant $^{Na}W^{Na}Se_2$ and isotopically enriched $^{186}W^{80}Se_2$ bilayer single crystals. A shorter interlayer van der Waals bond in $^{186}W^{80}Se_2$ than in $^{Na}W^{Na}Se_2$ was observed by X-ray diffraction characterization. The measured optical band gap in a $^{186}W^{80}Se_2$ bilayer is globally larger than that of a $^{Na}W^{Na}Se_2$ bilayer over the entire temperature range from the boiling point of liquid helium to near room temperature.

With the knowledge arising from this thesis, the future research that can be also raised is: (1) strain induced phase transition of TMDs could be interesting for strain dependent optoelectronic and electronic transport studies in memory and sensing applications; (2) controllable emission wavelengths, wider operating temperature and tunable emission life times of quantum emission defects will need to be better understood in atomically thin materials; (3) different isotopic enrichments of atomically thin TMDs combined with ultralow frequency Raman spectroscopy for probing the interlayer breathing mode is needed for a better understanding of the mechanism behind the van der Waals interaction effect on electronic band structure and phonon dispersion relationships.

References

1. Novoselov, K. S., Jiang, D., Schedin, F., Booth, T. J., Khotkevich, V. V., Morozov, S. V., & Geim, A. K. Two-dimensional atomic crystals. *Proceedings of the National Academy of Sciences of the United States of America* **102**, 10451-10453 (2005). http://dx.doi.org/10.1073/pnas.0502848102

2. van der Zande, A. M., Huang, P. Y., Chenet, D. A., Berkelbach, T. C., You, Y., Lee, G. H., Heinz, T. F., Reichman, D. R., Muller, D. A., & Hone, J. C. Grains and grain boundaries in highly crystalline monolayer molybdenum disulphide. *Nature Materials* **12**, 554-561 (2013). http://dx.doi.org/10.1038/nmat3633

3. Eichfeld, S. M., Hossain, L., Lin, Y. C., Piasecki, A. F., Kupp, B., Birdwell, A. G., Burke, R. A., Lu, N., Peng, X., Li, J., Azcatl, A., McDonnell, S., Wallace, R. M., Kim, M. J., Mayer, T. S., Redwing, J. M., & Robinson, J. A. Highly scalable, atomically thin WSe_2 grown via metal-organic chemical vapor deposition. *ACS Nano* **9**, 2080-2087 (2015). http://dx.doi.org/10.1021/nn5073286

4. Voiry, D., Goswami, A., Kappera, R., e Silva Cde, C., Kaplan, D., Fujita, T., Chen, M., Asefa, T., & Chhowalla, M. Covalent functionalization of monolayered transition metal dichalcogenides by phase engineering. *Nature Chemistry* **7**, 45-49 (2015). http://dx.doi.org/10.1038/nchem.2108

5. Lee, C. H., Lee, G. H., van der Zande, A. M., Chen, W., Li, Y., Han, M., Cui, X., Arefe, G., Nuckolls, C., Heinz, T. F., Guo, J., Hone, J., & Kim, P. Atomically thin p-n junctions with van der Waals heterointerfaces. *Nature Nanotechnology* **9**, 676-681 (2014). http://dx.doi.org/10.1038/nnano.2014.150

6. Palacios-Berraquero, C., Barbone, M., Kara, D. M., Chen, X., Goykhman, I., Yoon, D., Ott, A. K., Beitner, J., Watanabe, K., Taniguchi, T., Ferrari, A. C., & Atature, M. Atomically thin quantum light-emitting diodes. *Nature Communications* **7**, 12978 (2016). http://dx.doi.org/10.1038/ncomms12978

7. Branny, A., Kumar, S., Proux, R., & Gerardot, B. D. Deterministic strain-induced arrays of quantum emitters in a two-dimensional semiconductor. *Nature Communications* **8**, 15053 (2017). http://dx.doi.org/10.1038/ncomms15053

8. Palacios-Berraquero, C., Kara, D. M., Montblanch, A. R., Barbone, M., Latawiec, P., Yoon, D., Ott, A. K., Loncar, M., Ferrari, A. C., & Atature, M. Large-scale quantum-emitter arrays in atomically thin semiconductors. *Nature Communications* **8**, 15093 (2017). http://dx.doi.org/10.1038/ncomms15093

9. Tonndorf, P., Schmidt, R., Schneider, R., Kern, J., Buscema, M., Steele, G. A., Castellanos-Gomez, A., van der Zant, H. S. J., Michaelis de Vasconcellos, S., & Bratschitsch, R. Single-photon emission from localized excitons in an atomically thin semiconductor. *Optica* **2**, 347-352 (2015). http://dx.doi.org/10.1364/optica.2.000347

10. Srivastava, A., Sidler, M., Allain, A. V., Lembke, D. S., Kis, A., & Imamoğlu, A. Optically active quantum dots in monolayer WSe_2. *Nature Nanotechnology* **10**, 491–496 (2015). http://dx.doi.org/10.1038/nnano.2015.60

11. Koperski, M., Nogajewski, K., Arora, A., Cherkez, V., Mallet, P., Veuillen, J. Y., Marcus, J., Kossacki, P., & Potemski, M. Single photon emitters in exfoliated WSe_2 structures. *Nature Nanotechnology* **10**, 503-506 (2015). http://dx.doi.org/10.1038/nnano.2015.67

12. Chakraborty, C., Kinnischtzke, L., Goodfellow, K. M., Beams, R., & Vamivakas, A. N. Voltage-controlled quantum light from an atomically thin semiconductor. *Nature Nanotechnology* **10**, 507-511 (2015). http://dx.doi.org/10.1038/nnano.2015.79

13. Tran, T. T., Bray, K., Ford, M. J., Toth, M., & Aharonovich, I. Quantum emission from hexagonal boron nitride monolayers. *Nature Nanotechnology* **11**, 37-41 (2016). http://dx.doi.org/10.1038/nnano.2015.242

14. Kumar, S., Kaczmarczyk, A., & Gerardot, B. D. Strain-induced spatial and spectral isolation of quantum emitters in mono- and bilayer WSe_2. *Nano Letters* **15**, 7567-7573 (2015). http://dx.doi.org/10.1021/acs.nanolett.5b03312

15. He, X., Hartmann, N. F., Ma, X., Kim, Y., Ihly, R., Blackburn, J. L., Gao, W., Kono, J., Yomogida, Y., Hirano, A., Tanaka, T., Kataura, H., Htoon, H., & Doorn, S. K. Tunable room-temperature single-photon emission at telecom wavelengths from sp3 defects in carbon nanotubes. *Nature Photonics* **11**, 577-582 (2017). http://dx.doi.org/10.1038/nphoton.2017.119

16. Tonndorf, P., Schwarz, S., Kern, J., Niehues, I., del Pozo-Zamudio, O., Dmitriev, A. I., Bakhtinov, A. P., Borisenko, D. N., Kolesnikov, N. N., Tartakovskii, A. I., de Vasconcellos, S. M., & Bratschitsch, R. Single-photon emitters in GaSe. *2D Materials* **4**, 021010 (2017). http://dx.doi.org/10.1088/2053-1583/aa525b

17. Novoselov, K. S., Geim, A. K., Morozov, S. V., Jiang, D., Zhang, Y., Dubonos, S. V., Grigorieva, I. V., & Firsov, A. A. Electric field effect in atomically thin carbon films. *Science* **306**, 666-669 (2004). http://dx.doi.org/10.1126/science.1102896

18. Bolotin, K. I., Sikes, K. J., Jiang, Z., Klima, M., Fudenberg, G., Hone, J., Kim, P., & Stormer, H. L. Ultrahigh electron mobility in suspended graphene. *Solid State Communications* **146**, 351–355 (2008). http://dx.doi.org/10.1016/j.ssc.2008.02.024

19. Balandin, A. A., Ghosh, S., Bao, W., Calizo, I., Teweldebrhan, D., Miao, F., & Lau, C. N. Superior thermal conductivity of single-layer graphene. *Nano Letters* **8**, 902-907 (2008). http://dx.doi.org/10.1021/nl0731872

20. Pettes, M. T., Jo, I., Yao, Z., & Shi, L. Influence of polymeric residue on the thermal conductivity of suspended bilayer graphene. *Nano Letters* **11**, 1195-1200 (2011). http://dx.doi.org/10.1021/nl104156y

21. Seol, J. H., Jo, I., Moore, A. L., Lindsay, L., Aitken, Z. H., Pettes, M. T., Li, X., Yao, Z., Huang, R., Broido, D., Mingo, N., Ruoff, R. S., & Shi, L. Two-dimensional phonon transport in supported graphene. *Science* **328**, 213-216 (2010). http://dx.doi.org/10.1126/science.1184014

22. Lee, G. H., Yu, Y. J., Cui, X., Petrone, N., Lee, C. H., Choi, M. S., Lee, D. Y., Lee, C., Yoo, W. J., Watanabe, K., Taniguchi, T., Nuckolls, C., Kim, P., & Hone, J. Flexible and transparent MoS_2 field-effect transistors on hexagonal boron nitride-graphene heterostructures. *ACS Nano* **7**, 7931-7936 (2013). http://dx.doi.org/10.1021/nn402954e

23. Kim, Y. D., Kim, H., Cho, Y., Ryoo, J. H., Park, C. H., Kim, P., Kim, Y. S., Lee, S., Li, Y., Park, S. N., Yoo, Y. S., Yoon, D., Dorgan, V. E., Pop, E., Heinz, T. F., Hone, J., Chun, S. H., Cheong, H., Lee, S. W., Bae, M. H., & Park, Y. D. Bright visible light emission from graphene. *Nature Nanotechnology* **10**, 676-681 (2015). http://dx.doi.org/10.1038/nnano.2015.118

24. Liu, M., Yin, X., Ulin-Avila, E., Geng, B., Zentgraf, T., Ju, L., Wang, F., & Zhang, X. A graphene-based broadband optical modulator. *Nature* **474**, 64-67 (2011). http://dx.doi.org/10.1038/nature10067

25. Chen, H., Xu, H., Wang, S., Huang, T., Xi, J., Cai, S., Guo, F., Xu, Z., Gao, W., & Gao, C. Ultrafast all-climate aluminum-graphene battery with quarter-million cycle life. *Science Advances* **3**, eaao7233 (2017). http://dx.doi.org/10.1126/sciadv.aao7233

26. Geim, A. K. & Grigorieva, I. V. Van der Waals heterostructures. *Nature* **499**, 419-425 (2013). http://dx.doi.org/10.1038/nature12385

27. Chhowalla, M., Shin, H. S., Eda, G., Li, L. J., Loh, K. P., & Zhang, H. The chemistry of two-dimensional layered transition metal dichalcogenide nanosheets. *Nature Chemistry* **5**, 263-275 (2013). http://dx.doi.org/10.1038/nchem.1589

28. Butler, S. Z., Hollen, S. M., Cao, L., Cui, Y., Gupta, J. A., Gutierrez, H. R., Heinz, T. F., Hong, S. S., Huang, J., Ismach, A. F., Johnston-Halperin, E., Kuno, M., Plashnitsa, V. V., Robinson, R. D., Ruoff, R. S., Salahuddin, S., Shan, J., Shi, L., Spencer, M. G., Terrones, M., Windl, W., & Goldberger, J. E. Progress, challenges, and opportunities in two-dimensional materials beyond graphene. *ACS Nano* **7**, 2898-2926 (2013). http://dx.doi.org/10.1021/nn400280c

29. Bhimanapati, G. R., Lin, Z., Meunier, V., Jung, Y., Cha, J., Das, S., Xiao, D., Son, Y., Strano, M. S., Cooper, V. R., Liang, L., Louie, S. G., Ringe, E., Zhou, W., Kim, S. S., Naik, R. R., Sumpter, B. G., Terrones, H., Xia, F., Wang, Y., Zhu, J., Akinwande, D., Alem, N., Schuller, J. A., Schaak, R. E., Terrones, M., & Robinson, J. A. Recent advances in two-dimensional materials beyond graphene. *ACS Nano* **9**, 11509-11539 (2015). http://dx.doi.org/10.1021/acsnano.5b05556

30. Mak, K. F., Lee, C., Hone, J., Shan, J., & Heinz, T. F. Atomically thin MoS_2: a new direct-gap semiconductor. *Physical Review Letters* **105**, 136805 (2010). http://dx.doi.org/10.1103/PhysRevLett.105.136805

31. Gutierrez, H. R., Perea-Lopez, N., Elias, A. L., Berkdemir, A., Wang, B., Lv, R., Lopez-Urias, F., Crespi, V. H., Terrones, H., & Terrones, M. Extraordinary room-temperature photoluminescence in triangular WS_2 monolayers. *Nano Letters* **13**, 3447-3454 (2013). http://dx.doi.org/10.1021/nl3026357

32. Zhao, W., Ghorannevis, Z., Chu, L., Toh, M., Kloc, C., Tan, P. H., & Eda, G. Evolution of electronic structure in atomically thin sheets of WS_2 and WSe_2. *ACS Nano* **7**, 791-797 (2013). http://dx.doi.org/10.1021/nn305275h

33. Tongay, S., Sahin, H., Ko, C., Luce, A., Fan, W., Liu, K., Zhou, J., Huang, Y. S., Ho, C. H., Yan, J., Ogletree, D. F., Aloni, S., Ji, J., Li, S., Li, J., Peeters, F. M., & Wu, J. Monolayer behaviour in bulk ReS_2 due to electronic and vibrational decoupling. *Nature Communications* **5**, 3252 (2014). http://dx.doi.org/10.1038/ncomms4252

34. Mak, K. F., He, K., Lee, C., Lee, G. H., Hone, J., Heinz, T. F., & Shan, J. Tightly bound trions in monolayer MoS_2. *Nature Materials* **12**, 207-211 (2013). http://dx.doi.org/10.1038/nmat3505

35. Gong, Y., Lin, J., Wang, X., Shi, G., Lei, S., Lin, Z., Zou, X., Ye, G., Vajtai, R., Yakobson, B. I., Terrones, H., Terrones, M., Tay, B. K., Lou, J., Pantelides, S. T., Liu, Z., Zhou, W., & Ajayan, P. M. Vertical and in-plane heterostructures from WS_2/MoS_2 monolayers. *Nature Materials* **13**, 1135-1142 (2014). http://dx.doi.org/10.1038/nmat4091

36. Kang, J., Tongay, S., Zhou, J., Li, J., & Wu, J. Band offsets and heterostructures of two-dimensional semiconductors. *Applied Physics Letters* **102**, 012111 (2013). http://dx.doi.org/10.1063/1.4774090

37. Hu, X., Yasaei, P., Jokisaari, J., Ogut, S., Salehi-Khojin, A., & Klie, R. F. Mapping Thermal Expansion Coefficients in Freestanding 2D Materials at the Nanometer Scale. *Physical Review Letters* **120**, 055902 (2018). http://dx.doi.org/10.1103/PhysRevLett.120.055902

38. Bertolazzi, S., Brivio, J., & Kis, A. Stretching and breaking of ultrathin MoS_2. *ACS Nano* **5**, 9703-9709 (2011). http://dx.doi.org/10.1021/nn203879f

39. Wu, W., Wang, J., Ercius, P., Wright, N. C., Leppert-Simenauer, D. M., Burke, R. A., Dubey, M., Dogare, A. M., & Pettes, M. T. Giant mechano-optoelectronic effect in an atomically thin semiconductor. *Nano Letters* **18**, 2351-2357 (2018). http://dx.doi.org/10.1021/acs.nanolett.7b05229

40. Johari, P. & Shenoy, V. B. Tuning the electronic properties of semiconducting transition metal dichalcogenides by applying mechanical strains. *ACS Nano* **6**, 5449-5456 (2012). http://dx.doi.org/10.1021/nn301320r

41. Dong, L., Dongare, A. M., Namburu, R. R., O'Regan, T. P., & Dubey, M. Theoretical study on strain induced variations in electronic properties of *2H*-MoS_2 bilayer sheets. *Applied Physics Letters* **104**, 053107 (2014). http://dx.doi.org/10.1063/1.4863827

42. Hui, Y. Y., Liu, X., Jie, W., Chan, N. Y., Hao, J., Hsu, Y. T., Li, L. J., Guo, W., & Lau, S. P. Exceptional tunability of band energy in a compressively strained trilayer MoS_2 sheet. *ACS Nano* **7**, 7126-7131 (2013). http://dx.doi.org/10.1021/nn4024834

43. Lloyd, D., Liu, X., Christopher, J. W., Cantley, L., Wadehra, A., Kim, B. L., Goldberg, B. B., Swan, A. K., & Bunch, J. S. Band gap engineering with ultralarge biaxial strains in suspended monolayer MoS_2. *Nano Letters* **16**, 5836-5841 (2016). http://dx.doi.org/10.1021/acs.nanolett.6b02615

44. Manzeli, S., Allain, A., Ghadimi, A., & Kis, A. Piezoresistivity and strain-induced band gap tuning in atomically thin MoS_2. *Nano Letters* **15**, 5330-5335 (2015). http://dx.doi.org/10.1021/acs.nanolett.5b01689

45. Castellanos-Gomez, A., Roldan, R., Cappelluti, E., Buscema, M., Guinea, F., van der Zant, H. S., & Steele, G. A. Local strain engineering in atomically thin MoS2. *Nano Letters* **13**, 5361-5366 (2013). http://dx.doi.org/10.1021/nl402875m

46. Mohiuddin, T. M. G., Lombardo, A., Nair, R. R., Bonetti, A., Savini, G., Jalil, R., Bonini, N., Basko, D. M., Galiotis, C., Marzari, N., Novoselov, K. S., Geim, A. K., & Ferrari, A. C. Uniaxial strain in graphene by Raman spectroscopy: *G* peak splitting, Grüneisen parameters, and sample orientation. *Physical Review B* **79**, 205433 (2009). http://dx.doi.org/10.1103/PhysRevB.79.205433

47. Conley, H. J., Wang, B., Ziegler, J. I., Haglund, R. F., Jr., Pantelides, S. T., & Bolotin, K. I. Bandgap engineering of strained monolayer and bilayer MoS_2. *Nano Letters* **13**, 3626-3630 (2013). http://dx.doi.org/10.1021/nl4014748

48. Sanjurjo, J. A., López-Cruz, E., Vogl, P., & Cardona, M. Dependence on volume of the phonon frequencies and the ir effective charges of several III-V semiconductors. *Physical Review B* **28**, 4579-4584 (1983). http://dx.doi.org/10.1103/PhysRevB.28.4579

49. Kern, G., Kresse, G., & Hafner, J. Ab initiocalculation of the lattice dynamics and phase diagram of boron nitride. *Physical Review B* **59**, 8551-8559 (1999). http://dx.doi.org/10.1103/PhysRevB.59.8551

50. Desai, S. B., Seol, G., Kang, J. S., Fang, H., Battaglia, C., Kapadia, R., Ager, J. W., Guo, J., & Javey, A. Strain-induced indirect to direct bandgap transition in multilayer WSe_2. *Nano Letters* **14**, 4592-4597 (2014). http://dx.doi.org/10.1021/nl501638a

51. Dolbow, J. & Gosz, M. Effect of out-of-plane properties of a polyimide film on the stress fields in microelectronic structures. *Mechanics of Materials* **23**, 311-321 (1996). http://dx.doi.org/10.1016/0167-6636(96)00021-x

52. Li, Y., Hu, Z., Lin, S., Lai, S. K., Ji, W., & Lau, S. P. Giant Anisotropic Raman Response of Encapsulated Ultrathin Black Phosphorus by Uniaxial Strain. *Advanced Functional Materials* **27**, 1600986-1-9 (2017). http://dx.doi.org/10.1002/adfm.201600986

53. Androulidakis, C., Koukaras, E. N., Parthenios, J., Kalosakas, G., Papagelis, K., & Galiotis, C. Graphene flakes under controlled biaxial deformation. *Scientific Reports* **5**, 18219 (2015). http://dx.doi.org/10.1038/srep18219

54. Zabel, J., Nair, R. R., Ott, A., Georgiou, T., Geim, A. K., Novoselov, K. S., & Casiraghi, C. Raman spectroscopy of graphene and bilayer under biaxial strain: bubbles and balloons. *Nano Letters* **12**, 617-621 (2012). http://dx.doi.org/10.1021/nl203359n

55. Metzger, C., Remi, S., Liu, M., Kusminskiy, S. V., Castro Neto, A. H., Swan, A. K., & Goldberg, B. B. Biaxial strain in graphene adhered to shallow depressions. *Nano Letters* **10**, 6-10 (2010). http://dx.doi.org/10.1021/nl901625v

56. Metten, D., Federspiel, F., Romeo, M., & Berciaud, S. All-Optical Blister Test of Suspended Graphene Using Micro-Raman Spectroscopy. *Physical Review Applied* **2**, 054008 (2014). http://dx.doi.org/10.1103/PhysRevApplied.2.054008

57. Ding, F., Ji, H., Chen, Y., Herklotz, A., Dorr, K., Mei, Y., Rastelli, A., & Schmidt, O. G. Stretchable graphene: a close look at fundamental parameters through biaxial straining. *Nano Letters* **10**, 3453-3458 (2010). http://dx.doi.org/10.1021/nl101533x

58. Wang, Y., Cong, C., Qiu, C., & Yu, T. Raman spectroscopy study of lattice vibration and crystallographic orientation of monolayer MoS2 under uniaxial strain. *Small* **9**, 2857-2861 (2013). http://dx.doi.org/10.1002/smll.201202876

59. Rice, C., Young, R. J., Zan, R., Bangert, U., Wolverson, D., Georgiou, T., Jalil, R., & Novoselov, K. S. Raman-scattering measurements and first-principles calculations of strain-induced phonon shifts in monolayer MoS2. *Physical Review B* **87**, 081307 (2013). http://dx.doi.org/10.1103/PhysRevB.87.081307

60. Lee, J. U., Woo, S., Park, J., Park, H. C., Son, Y. W., & Cheong, H. Strain-shear coupling in bilayer MoS_2. *Nature Communications* **8**, 1370-1-7 (2017). http://dx.doi.org/10.1038/s41467-017-01487-3

61. Wang, F., Kinloch, I. A., Wolverson, D., Tenne, R., Zak, A., O'Connell, E., Bangert, U., & Young, R. J. Strain-induced phonon shifts in tungsten disulfide nanoplatelets and nanotubes. *2D Materials* **4**, 015007 (2016). http://dx.doi.org/10.1088/2053-1583/4/1/015007

62. Dadgar, A. M., Scullion, D., Kang, K., Esposito, D., Yang, E. H., Herman, I. P., Pimenta, M. A., Santos, E. J. G., & Pasupathy, A. N. Strain Engineering and Raman Spectroscopy

of Monolayer Transition Metal Dichalcogenides. *Chemistry of Materials* **30**, 5148-5155 (2018). http://dx.doi.org/10.1021/acs.chemmater.8b01672

63. Ashcroft, N. W. & Mermin, N. D. *Solid state physics*, College ed. (Philadelphia: W.B. Saunders, Philadelphia, 1976).

64. Eisaman, M. D., Fan, J., Migdall, A., & Polyakov, S. V. Invited review article: Single-photon sources and detectors. *Review of Scientific Instruments* **82**, 071101 (2011). http://dx.doi.org/10.1063/1.3610677

65. Santori, C., Fattal, D., & Yamamoto, Y. *Single Photon Devices and Applications* (Wiley Verlag GmbH & Co. KGaA, Weinheim, 2010). http://www.wiley.com/WileyCDA/WileyTitle/productCd-352740807X.html

66. Aharonovich, I. & Neu, E. Diamond nanophotonics. *Advanced Optical Materials* **2**, 911–928 (2014). http://dx.doi.org/10.1002/adom.201400189

67. Lounis, B. & Orrit, M. Single-photon sources. *Reports on Progress in Physics* **68**, 1129–1179 (2005). http://dx.doi.org/10.1088/0034-4885/68/5/R04

68. Aharonovich, I., Castelletto, S., Simpson, D. A., Su, C. H., Greentree, A. D., & Prawer, S. Diamond-based single-photon emitters. *Reports on Progress in Physics* **74**, 076501 (2011). http://dx.doi.org/10.1088/0034-4885/74/7/076501

69. Gordon, L., Weber, J. R., Varley, J. B., Janotti, A., Awschalom, D. D., & Van de Walle, C. G. Quantum computing with defects. *MRS Bulletin* **38**, 802−807 (2013). http://dx.doi.org/10.1557/mrs.2013.206

70. Acosta, V. & Hemmer, P. Nitrogen-vacancy centers: Physics and applications. *MRS Bulletin* **38**, 127−130 (2013). http://dx.doi.org/10.1557/mrs.2013.18

71. Yin, J., Cao, Y., Li, Y.-H., Liao, S.-K., Zhang, L., Ren, J.-G., Cai, W.-Q., Liu, W.-Y., Li, B., Dai, H., Li, G.-B., Lu, Q.-M., Gong, Y.-H., Xu, Y., Li, S.-L., Li, F.-Z., Yin, Y.-Y., Jiang, Z.-Q., Li, M., Jia, J.-J., Ren, G., He, D., Zhou, Y.-L., Zhang, X.-X., Wang, N., Chang, X., Zhu, Z.-C., Liu, N.-L., Chen, Y.-A., Lu, C.-Y., Shu, R., Peng, C.-Z., Wang, J.-Y., & Pan, J.-W. Satellite-based entanglement distribution over 1200 kilometers. *Science* **356**, 1140–1144 (2017). http://dx.doi.org/10.1126/science.aan3211

72. Brown, R. H. & Twiss, R. Q. Correlation between Photons in two Coherent Beams of Light. *Nature* **177**, 27-29 (1956). http://dx.doi.org/10.1038/177027a0

73. Senellart, P., Solomon, G., & White, A. High-performance semiconductor quantum-dot single-photon sources. *Nature Nanotechnology* **12**, 1026-1039 (2017). http://dx.doi.org/10.1038/nnano.2017.218

74. Hogele, A., Galland, C., Winger, M., & Imamoglu, A. Photon antibunching in the photoluminescence spectra of a single carbon nanotube. *Physical Review Letters* **100**, 217401 (2008). http://dx.doi.org/10.1103/PhysRevLett.100.217401

75. Lounis, B. & Moerner, W. E. Single photons on demand from a single molecule at room temperature. *Nature* **407**, 491-493 (2000). http://dx.doi.org/10.1038/35035032

76. Kurtsiefer, C., Mayer, S., Zarda, P., & Weinfurter, H. Stable solid-state source of single photons. *Physical Review Letters* **85**, 290-293 (2000). http://dx.doi.org/10.1103/PhysRevLett.85.290

77. Michler, P., Kiraz, A., Becher, C., Schoenfeld, W. V., Petroff, P. M., Zhang, L., Hu, E., & Imamoglu, A. A quantum dot single-photon turnstile device. *Science* **290**, 2282-2285 (2000). http://dx.doi.org/10.1126/science.290.5500.2282

78. Michler, P., Imamoglu, A., Mason, M. D., Carson, P. J., Strouse, G. F., & Buratto, S. K. Quantum correlation among photons from a single quantum dot at room temperature. *Nature* **406**, 968-970 (2000). http://dx.doi.org/10.1038/35023100

79. Wang, J., Zhou, Y., Wang, Z., Rasmita, A., Yang, J., Li, X., von Bardeleben, H. J., & Gao, W. Bright room temperature single photon source at telecom range in cubic silicon carbide. *Nature Communications* **9**, 4106 (2018). http://dx.doi.org/10.1038/s41467-018-06605-3

80. Kern, J., Niehues, I., Tonndorf, P., Schmidt, R., Wigger, D., Schneider, R., Stiehm, T., Michaelis de Vasconcellos, S., Reiter Doris, E., Kuhn, T., & Bratschitsch, R. Nanoscale positioning of single‐photon emitters in atomically thin WSe_2. *Advanced Materials* **28**, 7101–7105 (2016). http://dx.doi.org/10.1002/adma.201600560

81. Noh, G., Choi, D., Kim, J. H., Im, D. G., Kim, Y. H., Seo, H., & Lee, J. Stark Tuning of Single-Photon Emitters in Hexagonal Boron Nitride. *Nano Letters* **18**, 4710-4715 (2018). http://dx.doi.org/10.1021/acs.nanolett.8b01030

82. Tonndorf, P., Del Pozo-Zamudio, O., Gruhler, N., Kern, J., Schmidt, R., Dmitriev, A. I., Bakhtinov, A. P., Tartakovskii, A. I., Pernice, W., Michaelis de Vasconcellos, S., & Bratschitsch, R. On-chip waveguide coupling of a layered semiconductor single-photon source. *Nano Letters* **17**, 5446−5451 (2017). http://dx.doi.org/10.1021/acs.nanolett.7b02092

83. He, Y.-M., Clark, G., Schaibley, J., R., He, Y., Chen, M.-C., Wei, Y.-J., Ding, X., Zhang, Q., Yao, W., Xu, X., Lu, C.-Y., & Pan, J.-W. Single quantum emitters in monolayer semiconductors. *Nature Nanotechnology* **10**, 497–502 (2015). http://dx.doi.org/10.1038/nnano.2015.75

84. Andres-Penares, D., Cros, A., Martínez-Pastor, J. P., & Sánchez-Royo, J. F. Quantum size confinement in gallium selenide nanosheets: Band gap tunability versus stability limitation. *Nanotechnology* **28**, 175701 (2017). http://dx.doi.org/10.1088/1361-6528/aa669e

85. Ma, X., Hartmann, N. F., Baldwin, J. K. S., Doorn, S. K., & Htoon, H. Room-temperature single-photon generation from solitary dopants of carbon nanotubes. *Nature Nanotechnology* **10**, 671–675 (2015). http://dx.doi.org/10.1038/nnano.2015.136

86. Hofmann, M. S., Noé, J., Kneer, A., Crochet, J. J., & Högele, A. Ubiquity of exciton localization in cryogenic carbon nanotubes. *Nano Letters* **16**, 2958–2962 (2016). http://dx.doi.org/10.1021/acs.nanolett.5b04901

87. Toyli, D. M., Weis, C. D., Fuchs, G. D., Schenkel, T., & Awschalom, D. D. Chip-scale nanofabrication of single spins and spin arrays in diamond. *Nano Letters* **10**, 3168–3172 (2010). http://dx.doi.org/10.1021/nl102066q

88. Vuong, T. Q. P., Liu, S., Van der Lee, A., Cuscó, R., Artús, L., Michel, T., Valvin, P., Edgar, J. H., Cassabois, G., & Gil, B. Isotope engineering of van der Waals interactions in hexagonal boron nitride. *Nature Materials* **17**, 152-158 (2017). http://dx.doi.org/10.1038/nmat5048

89. Soddy, F. Intra-atomic charge. *Nature* **92**, 399-400 (1913). http://dx.doi.org/10.1038/092399c0

90. Thomson, J. J. On the appearance of helium and neon in vacuum tubes. *Nature* **90**, 645-647 (1913). http://dx.doi.org/10.1038/090645d0

91. Aston, F. W. Isotopes and atomic weights. *Nature* **105**, 617-619 (1920). http://dx.doi.org/10.1038/105617a0

92. Klemens, P. G. The sscattering of low-frequency lattice waves by static imperfections. *Proceedings of the Physical Society. Section A* **68**, 1113-1128 (1955). http://dx.doi.org/10.1088/0370-1298/68/12/303

93. Tamura, S.-i. Isotope scattering of dispersive phonons in Ge. *Physical Review B* **27**, 858-866 (1983). http://dx.doi.org/10.1103/PhysRevB.27.858

94. Kittel, C. *Introduction to Solid State Physics*, 8th ed. (John Wiley & Sons, New York, 2005). ISBN : 978-0-471-41526-8, http://www.wiley.com/WileyCDA/WileyTitle/productCd-EHEP000803.html

95. Cardona, M. & Thewalt, M. L. W. Isotope effects on the optical spectra of semiconductors. *Reviews of Modern Physics* **77**, 1173-1224 (2005). http://dx.doi.org/10.1103/RevModPhys.77.1173

96. Zhang, J. M., Giehler, M., Göbel, A., Ruf, T., Cardona, M., Haller, E. E., & Itoh, K. Optical phonons in isotopic Ge studied by Raman scattering. *Physical Review B* **57**, 1348-1351 (1998). http://dx.doi.org/10.1103/PhysRevB.57.1348

97. Göbel, A., Ruf, T., Zhang, J. M., Lauck, R., & Cardona, M. Phonons and fundamental gap in ZnSe: Effects of the isotopic composition. *Physical Review B* **59**, 2749-2759 (1999). http://dx.doi.org/10.1103/PhysRevB.59.2749

98. Cardona, M. & Ruf, T. Phonon self-energies in semiconductors: anharmonic and isotopic contributions. *Solid State Communications* **117**, 201-212 (2001). http://dx.doi.org/10.1016/s0038-1098(00)00443-9

99. Etchegoin, P., Weber, J., Cardona, M., Hansen, W. L., Itoh, K., & Haller, E. E. Isotope effect in Ge: A photoluminescence study. *Solid State Communications* **83**, 843-848 (1992). http://dx.doi.org/10.1016/0038-1098(92)90897-i

100. Broido, D. A., Lindsay, L., & Reinecke, T. L. Ab initiostudy of the unusual thermal transport properties of boron arsenide and related materials. *Physical Review B* **88**, 214303 (2013). http://dx.doi.org/10.1103/PhysRevB.88.214303

101. Belay, K., Etzel, Z., Onn, D. G., & Anthony, T. R. The thermal conductivity of polycrystalline diamond films: Effects of isotope content. *Journal of Applied Physics* **79**, 8336-8340 (1996). http://dx.doi.org/10.1063/1.362546

102. Asen-Palmer, M., Bartkowski, K., Gmelin, E., Cardona, M., Zhernov, A. P., Inyushkin, A. V., Taldenkov, A., Ozhogin, V. I., Itoh, K. M., & Haller, E. E. Thermal conductivity of germanium crystals with different isotopic compositions. *Physical Review B* **56**, 9431-9447 (1997). http://dx.doi.org/10.1103/PhysRevB.56.9431

103. Morelli, D. T., Heremans, J. P., & Slack, G. A. Estimation of the isotope effect on the lattice thermal conductivity of group IV and group III-V semiconductors. *Physical Review B* **66**, 195304 (2002). http://dx.doi.org/10.1103/PhysRevB.66.195304

104. Lindsay, L. & Broido, D. A. Enhanced thermal conductivity and isotope effect in single-layer hexagonal boron nitride. *Physical Review B* **84**, 155421-1-6 (2011). http://dx.doi.org/10.1103/PhysRevB.84.155421

105. Jo, I., Pettes, M. T., Kim, J., Watanabe, K., Taniguchi, T., Yao, Z., & Shi, L. Thermal conductivity and phonon transport in suspended few-layer hexagonal boron nitride. *Nano Letters* **13**, 550-554 (2013). http://dx.doi.org/10.1021/nl304060g

106. Smith, A. W. Low-Temperature Thermal Conductivity of a Canadian Natural Graphite. *Physical Review* **95**, 1095-1096 (1954). http://dx.doi.org/10.1103/PhysRev.95.1095

107. Sichel, E. K., Miller, R. E., Abrahams, M. S., & Buiocchi, C. J. Heat capacity and thermal conductivity of hexagonal pyrolytic boron nitride. *Physical Review B* **13**, 4607-4611 (1976). http://dx.doi.org/10.1103/PhysRevB.13.4607

108. Raman, C. V. & Krishnan, K. S. A New Type of Secondary Radiation. *Nature* **121**, 501-502 (1928). http://dx.doi.org/10.1038/121501c0

109. Sfeir, M. Y., Wang, F., Huang, L., Chuang, C. C., Hone, J., O'Brien S, P., Heinz, T. F., & Brus, L. E. Probing electronic transitions in individual carbon nanotubes by Rayleigh scattering. *Science* **306**, 1540-1543 (2004). http://dx.doi.org/10.1126/science.1103294

110. Wang, F., Sfeir, M. Y., Huang, L., Huang, X. M., Wu, Y., Kim, J., Hone, J., O'Brien, S., Brus, L. E., & Heinz, T. F. Interactions between individual carbon nanotubes studied by Rayleigh scattering spectroscopy. *Physical Review Letters* **96**, 167401 (2006). http://dx.doi.org/10.1103/PhysRevLett.96.167401

111. Huang, M., Yan, H., Chen, C., Song, D., Heinz, T. F., & Hone, J. Phonon softening and crystallographic orientation of strained graphene studied by Raman spectroscopy. *Proceedings of the National Academy of Sciences of the United States of America* **106**, 7304-7408 (2009). http://dx.doi.org/10.1073/pnas.0811754106

112. Terrones, H., Del Corro, E., Feng, S., Poumirol, J. M., Rhodes, D., Smirnov, D., Pradhan, N. R., Lin, Z., Nguyen, M. A., Elias, A. L., Mallouk, T. E., Balicas, L., Pimenta, M. A., & Terrones, M. New first order Raman-active modes in few layered transition metal dichalcogenides. *Scientific Reports* **4**, 4215 (2014). http://dx.doi.org/10.1038/srep04215

113. Saito, R., Tatsumi, Y., Huang, S., Ling, X., & Dresselhaus, M. S. Raman spectroscopy of transition metal dichalcogenides. *Journal of Physics: Condensed Matter* **28**, 353002 (2016). http://dx.doi.org/10.1088/0953-8984/28/35/353002

114. Coblentz, W. W. *Investigations of infra-red spectra* (Washington, D.C.: Carnegie institution of Washington, 1905).

115. Zhao, Y., Luo, X., Li, H., Zhang, J., Araujo, P. T., Gan, C. K., Wu, J., Zhang, H., Quek, S. Y., Dresselhaus, M. S., & Xiong, Q. Interlayer breathing and shear modes in few-trilayer MoS_2 and WSe_2. *Nano Letters* **13**, 1007-1015 (2013). http://dx.doi.org/10.1021/nl304169w

116. Huang, S., Liang, L., Ling, X., Puretzky, A. A., Geohegan, D. B., Sumpter, B. G., Kong, J., Meunier, V., & Dresselhaus, M. S. Low-frequency interlayer Raman modes to probe interface of twisted bilayer MoS_2. *Nano Letters* **16**, 1435-1444 (2016). http://dx.doi.org/10.1021/acs.nanolett.5b05015

117. Liu, B., Fathi, M., Chen, L., Abbas, A., Ma, Y., & Zhou, C. Chemical Vapor Deposition Growth of Monolayer WSe_2 with Tunable Device Characteristics and Growth Mechanism Study. *ACS Nano* **9**, 6119-6127 (2015). http://dx.doi.org/10.1021/acsnano.5b01301

118. Roddaro, S., Pingue, P., Piazza, V., Pellegrini, V., & Beltram, F. The optical visibility of graphene: interference colors of ultrathin graphite on SiO_2. *Nano Letters* **7**, 2707-2710 (2007). http://dx.doi.org/10.1021/nl071158l

119. Chen, J., Liu, B., Liu, Y., Tang, W., Nai, C. T., Li, L., Zheng, J., Gao, L., Zheng, Y., Shin, H. S., Jeong, H. Y., & Loh, K. P. Chemical vapor deposition of large-sized hexagonal WSe_2 crystals on dielectric substrates. *Advanced Materials* **27**, 6722–6727 (2015). http://dx.doi.org/10.1002/adma.201503446

120. Wong-Ng, W., McMurdie, H. F., Paretzkin, B., Zhang, Y., Davis, K. L., Hubbard, C. R., Dragoo, A. L., & Stewart, J. M. Reference X-ray diffraction powder patterns of fifteen

ceramic phases. *Powder Diffraction* **2**, 257-265 (1987). http://dx.doi.org/10.1017/S0885715600012926

121. Bilgin, I., Liu, F., Vargas, A., Winchester, A., Man, M. K., Upmanyu, M., Dani, K. M., Gupta, G., Talapatra, S., Mohite, A. D., & Kar, S. Chemical vapor deposition synthesized atomically thin molybdenum disulfide with optoelectronic-grade crystalline quality. *ACS Nano* **9**, 8822–8832 (2015). http://dx.doi.org/10.1021/acsnano.5b02019

122. Libby, W. F. Isotope Size Effect in Van der Waals Radii and the Barrier to Rotation around the Carbon‐Carbon Single Bond. *The Journal of Chemical Physics* **35**, 1527-1527 (1961). http://dx.doi.org/10.1063/1.1732100

123. Schmidt, R., Niehues, I., Schneider, R., Drüppel, M., Deilmann, T., Rohlfing, M., Michaelis de Vasconcellos, S., Castellanos-Gomez, A., & Bratschitsch, R. Reversible uniaxial strain tuning in atomically thin WSe_2. *2D Materials* **3**, 021011 (2016). http://dx.doi.org/10.1088/2053-1583/3/2/021011

124. Liu, Z., Amani, M., Najmaei, S., Xu, Q., Zou, X., Zhou, W., Yu, T., Qiu, C., Birdwell, A. G., Crowne, F. J., Vajtai, R., Yakobson, B. I., Xia, Z., Dubey, M., Ajayan, P. M., & Lou, J. Strain and structure heterogeneity in MoS_2 atomic layers grown by chemical vapour deposition. *Nature Communications* **5**, 5246-1-9 (2014). http://dx.doi.org/10.1038/ncomms6246

125. Ahn, G. H., Amani, M., Rasool, H., Lien, D. H., Mastandrea, J. P., Ager Iii, J. W., Dubey, M., Chrzan, D. C., Minor, A. M., & Javey, A. Strain-engineered growth of two-dimensional materials. *Nature Communications* **8**, 608 (2017). http://dx.doi.org/10.1038/s41467-017-00516-5

126. Tonndorf, P., Schmidt, R., Bottger, P., Zhang, X., Borner, J., Liebig, A., Albrecht, M., Kloc, C., Gordan, O., Zahn, D. R., Michaelis de Vasconcellos, S., & Bratschitsch, R. Photoluminescence emission and Raman response of monolayer MoS_2, $MoSe_2$, and WSe_2. *Optics Express* **21**, 4908-4916 (2013). http://dx.doi.org/10.1364/OE.21.004908

127. Dong, L., Wang, J., Namburu, R., O'Regan, T. P., Dubey, M., & Dongare, A. M. Edge effects on band gap energy in bilayer 2H-MoS_2 under uniaxial strain. *Journal of Applied Physics* **117**, 244303 (2015). http://dx.doi.org/10.1063/1.4922811

128. Suk, J. W., Kitt, A., Magnuson, C. W., Hao, Y., Ahmed, S., An, J., Swan, A. K., Goldberg, B. B., & Ruoff, R. S. Transfer of CVD-grown monolayer graphene onto arbitrary substrates. *ACS Nano* **5**, 6916–6924 (2011). http://dx.doi.org/10.1021/nn201207c

129. Schneider, C. A., Rasband, W. S., & Eliceiri, K. W. NIH Image to ImageJ: 25 years of image analysis. *Nature Methods* **9**, 671–675 (2012). http://dx.doi.org/10.1038/nmeth.2089

130. Grüneisen, E. Theorie des festen Zustandes einatomiger Elemente. *Annalen der Physik* **344**, 257–306 (1912). http://dx.doi.org/10.1002/andp.19123441202

131. Dove, M. T. *Introduction to Lattice Dynamics* (Cambridge University Press, Cambridge, 1993). 10.1017/cbo9780511619885

132. Greaves, G. N., Greer, A. L., Lakes, R. S., & Rouxel, T. Poisson's ratio and modern materials. *Nature Materials* **10**, 823–837 (2011). http://dx.doi.org/10.1038/nmat3134

133. Chen, Y. L., Analytis, J. G., Chu, J.-H., Liu, Z. K., Mo, S.-K., Qi, X. L., Zhang, H. J., Lu, D. H., Dai, X., Fang, Z., Zhang, S. C., Fisher, I. R., Hussain, Z., & Shen, Z.-X.

Experimental realization of a three-dimensional topological insulator, Bi_2Te_3. *Science* **325**, 178–181 (2009). http://dx.doi.org/10.1126/science.1173034

134. Kim, S. M., Hsu, A., Lee, Y.-H., Dresselhaus, M., Palacios, T., Kim, K. K., & Kong, J. The effect of copper pre-cleaning on graphene synthesis. *Nanotechnology* **24**, 365602 (2013). http://dx.doi.org/10.1088/0957-4484/24/36/365602

135. Ferrari, A. C., Meyer, J. C., Scardaci, V., Casiraghi, C., Lazzeri, M., Mauri, F., Piscanec, S., Jiang, D., Novoselov, K. S., Roth, S., & Geim, A. K. Raman spectrum of graphene and graphene layers. *Physical Review Letters* **97**, 187401 (2006). http://dx.doi.org/10.1103/PhysRevLett.97.187401

136. Pospischil, A., Furchi, M. M., & Mueller, T. Solar-energy conversion and light emission in an atomic monolayer p-n diode. *Nature Nanotechnology* **9**, 257–261 (2014). http://dx.doi.org/10.1038/nnano.2014.14

137. Jo, I., Pettes, M. T., Ou, E., Wu, W., & Shi, L. Basal-plane thermal conductivity of few-layer molybdenum disulfide. *Applied Physics Letters* **104**, 201902 (2014). http://dx.doi.org/10.1063/1.4876965

138. Mavrokefalos, A., Lin, Q., Beekman, M., Seol, J. H., Lee, Y. J., Kong, H., Pettes, M. T., Johnson, D. C., & Shi, L. In-plane thermal and thermoelectric properties of misfit-layered $[(PbSe)_{0.99}]_x(WSe_2)_x$ superlattice thin films. *Applied Physics Letters* **96**, 181908 (2010). http://dx.doi.org/10.1063/1.3428577

139. Mavrokefalos, A., Nguyen, N. T., Pettes, M. T., Johnson, D. C., & Shi, L. In-plane thermal conductivity of disordered layered WSe_2 and $(W)_x(WSe_2)_y$ superlattice films. *Applied Physics Letters* **91**, 171912 (2007). http://dx.doi.org/10.1063/1.2800888

140. Chiritescu, C., Cahill, D. G., Nguyen, N., Johnson, D., Bodapati, A., Keblinski, P., & Zschack, P. Ultralow thermal conductivity in disordered, layered WSe_2 crystals. *Science* **315**, 351–353 (2007). http://dx.doi.org/10.1126/science.1136494

141. Jones, A. M., Yu, H., Ross, J. S., Klement, P., Ghimire, N. J., Yan, J., Mandrus, D. G., Yao, W., & Xu, X. Spin–layer locking effects in optical orientation of exciton spin in bilayer WSe_2. *Nature Physics* **10**, 130–134 (2014). http://dx.doi.org/10.1038/nphys2848

142. You, Y., Zhang, X.-X., Berkelbach, T. C., Hybertsen, M. S., Reichman, D. R., & Heinz, T. F. Observation of biexcitons in monolayer WSe_2. *Nature Physics* **11**, 477–481 (2015). http://dx.doi.org/10.1038/nphys3324

143. Sze, S. M. & Ng, K. K. *Physics of Semiconductor Devices*, 3 ed. (Wiley, New Jersey, 2006). 10.1002/0470068329

144. Niehues, I., Schmidt, R., Drüppel, M., Marauhn, P., Christiansen, D., Selig, M., Berghäuser, G., Wigger, D., Schneider, R., Braasch, L., Koch, R., Castellanos-Gomez, A., Kuhn, T., Knorr, A., Malic, E., Rohlfing, M., Michaelis de Vasconcellos, S., & Bratschitsch, R. Strain control of exciton–phonon coupling in atomically thin semiconductors. *Nano Letters* **18**, 1751–1757 (2018). http://dx.doi.org/10.1021/acs.nanolett.7b04868

145. Zhu, C. R., Wang, G., Liu, B. L., Marie, X., Qiao, X. F., Zhang, X., Wu, X. X., Fan, H., Tan, P. H., Amand, T., & Urbaszek, B. Strain tuning of optical emission energy and polarization in monolayer and bilayer MoS_2. *Physical Review B* **88**, 121301 (2013). http://dx.doi.org/10.1103/PhysRevB.88.121301

146. Zhou, H., Wang, C., Shaw, J. C., Cheng, R., Chen, Y., Huang, X., Liu, Y., Weiss, N. O., Lin, Z., Huang, Y., & Duan, X. Large area growth and electrical properties of p-type

WSe_2 atomic layers. *Nano Letters* **15**, 709-713 (2015). http://dx.doi.org/10.1021/nl504256y

147. Huang, J.-K., Pu, J., Hsu, C.-L., Chiu, M.-H., Juang, Z.-Y., Chang, Y.-H., Chang, W.-H., Iwasa, Y., Takenobu, T., & Li, L.-J. Large-area synthesis of highly crystalline WSe_2 monolayers and device applications. *ACS Nano* **8**, 923-930 (2014). http://dx.doi.org/10.1021/nn405719x

148. Huang, C., Wu, S., Sanchez, A. M., Peters, J. J. P., Beanland, R., Ross, J. S., Rivera, P., Yao, W., Cobden, D. H., & Xu, X. Lateral heterojunctions within monolayer $MoSe_2$–WSe_2 semiconductors. *Nature Materials* **13**, 1096-1101 (2014). http://dx.doi.org/10.1038/nmat4064

149. Zhang, X., Choudhury, T. H., Chubarov, M., Xiang, Y., Jariwala, B., Zhang, F., Alem, N., Wang, G.-C., Robinson, J. A., & Redwing, J. M. Diffusion-controlled epitaxy of large area coalesced WSe_2 monolayers on sapphire. *Nano Letters* **18**, 1049–1056 (2018). http://dx.doi.org/10.1021/acs.nanolett.7b04521

150. Loudon, R. *The Quantum Theory of Light* (Oxford University Press, New York, 2000).

151. Rodiek, B., Lopez, M., Hofer, H., Porrovecchio, G., Smid, M., Chu, X.-L., Gotzinger, S., Sandoghdar, V., Lindner, S., Becher, C., & Kuck, S. Experimental realization of an absolute single-photon source based on a single nitrogen vacancy center in a nanodiamond. *Optica* **4**, 71–76 (2017). http://dx.doi.org/10.1364/OPTICA.4.000071

152. Kumar, S., Brotóns-Gisbert, M., Al-Khuzheyri, R., Branny, A., Ballesteros-Garcia, G., Sánchez-Royo, J. F., & Gerardot, B. D. Resonant laser spectroscopy of localized excitons in monolayer WSe_2. *Optica* **3**, 882–886 (2016). http://dx.doi.org/10.1364/OPTICA.3.000882

153. Pettes, M. T., Kim, J., Wu, W., Bustillo, K. C., & Shi, L. Thermoelectric transport in surface- and antimony-doped bismuth telluride nanoplates. *APL Materials* **4**, 104810 (2016). http://dx.doi.org/10.1063/1.4955400

154. Pettes, M. T., Maassen, J., Jo, I., Lundstrom, M. S., & Shi, L. Effects of surface band bending and scattering on thermoelectric transport in suspended bismuth telluride nanoplates. *Nano Letters* **13**, 5316-5322 (2013). http://dx.doi.org/10.1021/nl402828s

155. Coletti, C., Riedl, C., Lee, D. S., Krauss, B., Patthey, L., von Klitzing, K., Smet, J. H., & Starke, U. Charge neutrality and band-gap tuning of epitaxial graphene on SiC by molecular doping. *Physical Review B* **81**, 235401 (2010). http://dx.doi.org/10.1103/PhysRevB.81.235401

156. Kim, D., Cho, S., Butch, N. P., Syers, P., Kirshenbaum, K., Adam, S., Paglione, J., & Fuhrer, M. S. Surface conduction of topological Dirac electrons in bulk insulating Bi_2Se_3. *Nature Physics* **8**, 459-463 (2012). http://dx.doi.org/10.1038/nphys2286

157. Pettes, M. T., Sadeghi, M. M., Ji, H., Jo, I., Wu, W., Ruoff, R. S., & Shi, L. Scattering of phonons by high-concentration isotopic impurities in ultrathin graphite. *Physical Review B* **91**, 035429 (2015). http://dx.doi.org/10.1103/PhysRevB.91.035429

158. Cuscó, R., Artús, L., Edgar, J. H., Liu, S., Cassabois, G., & Gil, B. Isotopic effects on phonon anharmonicity in layered van der Waals crystals: Isotopically pure hexagonal boron nitride. *Physical Review B* **97**, 155435 (2018). http://dx.doi.org/10.1103/PhysRevB.97.155435

159. Beechem, T. & Graham, S. Temperature and doping dependence of phonon lifetimes and decay pathways in GaN. *Journal of Applied Physics* **103**, 093507 (2008). http://dx.doi.org/10.1063/1.2912819

160. Murray, R. & Evans, B. The thermal expansion of 2*H*-MoS_2 and 2*H*-WSe_2 between 10 and 320 K. *Journal of Applied Crystallography* **12**, 312-315 (1979). http://dx.doi.org/10.1107/s0021889879012528

161. Cao, B. & Li, T. Interlayer electronic coupling in arbitrarily stacked MoS_2 bilayers controlled by interlayer S–S interaction. *The Journal of Physical Chemistry C* **119**, 1247-1252 (2015). http://dx.doi.org/10.1021/jp5101736

162. Varshni, Y. P. Temperature dependence of the energy gap in semiconductors. *Physica* **34**, 149-154 (1967). http://dx.doi.org/10.1016/0031-8914(67)90062-6

163. Cardona, M. & Kremer, R. K. Temperature dependence of the electronic gaps of semiconductors. *Thin Solid Films* **571**, 680-683 (2014). http://dx.doi.org/10.1016/j.tsf.2013.10.157

164. Lautenschlager, P., Allen, P. B., & Cardona, M. Temperature dependence of band gaps in Si and Ge. *Physical Review B* **31**, 2163-2171 (1985). http://dx.doi.org/10.1103/PhysRevB.31.2163